



Pedro Rafael Martins de Almeida Sampaio

Degree in Molecular and Cell Biology

Using cilia mutants to study left-right asymmetry in zebrafish

A thesis submitted in fulfillment of the requirements for the degree of the Masters in Molecular Genetics and Biomedicine

Supervisor: Susana Santos Lopes, PhD, CEDOC-FCM
Internal supervisor: Ana Madalena Ludovice, PhD, FCT/UNL

Using cilia mutants to study left-right asymmetry in zebrafish

Submitted by

Pedro Rafael Martins de Almeida Sampaio

A thesis submitted in fulfillment of the requirements for the degree of

Masters in Molecular Genetics and Biomedicine

February 2014

Using cilia mutants to study left-right asymmetry in zebrafish

Copyright Pedro Rafael Martins de Almeida Sampaio, FCT/UNL, UNL

A Faculdade de Ciências e Tecnologia e a Universidade Nova de Lisboa têm o direito, perpétuo e sem limites geográficos, de arquivar e publicar esta dissertação através de exemplares impressos reproduzidos em papel ou de forma digital, ou por qualquer outro meio conhecido ou que venha a ser inventado, e de a divulgar através de repositórios científicos e de admitir a sua cópia e distribuição com objectivos educacionais ou de investigação, não comerciais, desde que seja dado crédito ao autor e editor.

Acknowledgments

I would like to start saying that in this last year I had the privilege to work and learn from so many and good scientists, without whom this work would not have been possible. For those who were part of it, I want to express my deepest gratitude.

Moreover, I want to thank especially to:

Susana Lopes, my supervisor, for letting me to be part of her “ship”; for mentoring and guiding me during this exciting ride; for promoting and supporting my scientific growth; and most important of all for believing me. I am honestly thankful and privileged for having worked with you!

Petra and Bárbara for all the patience and great support showed to me since the beginning. You were really the cornerstones of this work, for all you taught me.

Cláudia Pereira, Petra, “Princesa do Mal”, Queiroga, Sofia, “Tsabimbi”, “Amélia” and Telmo for the friendship and all the good moments and support. I really feel lucky for having met all of you!

Adán Guerrero for teaching and discussing with me so many things that helped me a lot for the success of this work and my growth as a scientist; for showing so much support and being there when I needed. I believe you are a great scientist and I wish you all the best in the coming years. Muchas gracias, un gran abrazo!

My closest friends, for being there when I needed them.

My family, for the unconditional love and support, especially to my parents, my brother that was always at my side, and my grandparents.

Abstract

In vertebrates, internal organs are positioned asymmetrically across the left-right (L-R) body axis. Events determining L-R asymmetry occur during embryogenesis, and are regulated by the coordinated action of genetic mechanisms. Embryonic motile cilia are essential in this process by generating a directional fluid flow inside the zebrafish organ of asymmetry, called Kupffer's vesicle (KV). A correct L-R formation is highly dependent on signaling pathways downstream of such flow, however detailed characterization of how its dynamics modulates these mechanisms is still lacking.

In this project, fluid flow measurements were achieved by a non-invasive method, in four genetic backgrounds: Wild-type (WT), *deltaD*^{-/-} mutants, Dnah7 morphants (MO) and control-MO embryos. Knockdown of Dnah7, a heavy chain inner axonemal dynein, renders cilia completely immotile and depletes the KV directional fluid flow, which we characterize here for the first time. By following the development of each embryo, we show that flow dynamics in the KV is already asymmetric and provides a very good prediction of organ laterality.

Through novel experiments, we characterized a new population of motile cilia, an immotile population, a range of cilia beat frequencies and lengths, KV volumes and cilia numbers in live embryos. These data were crucial to perform fluid dynamics simulations, which suggested that the flow in embryos with 30 or more cilia reliably produces left *situs*; with fewer cilia, left *situs* is sometimes compromised through disruption of the dorsal anterior clustering of motile cilia. A rough estimate based upon the 30 cilium threshold and statistics of cilium number predicts 90% and 60% left *situs* in WT and *deltaD*^{-/-} respectively, as observed experimentally. Cilia number and clustering are therefore critical to normal *situs* via robust asymmetric flow. Thus, our results support a model in which asymmetric flow forces registered in the KV pattern organ laterality in each embryo.

Key words: Kupffer's vesicle, motile cilia, KV flow, left-right asymmetry, dnah7, *deltaD*^{-/-} mutant.

Resumo

Em vertebrados, os órgãos viscerais estão posicionados assimetricamente ao longo do eixo esquerdo-direito (E-D) do organismo. Esta assimetria ocorre durante a embriogénese sendo determinada pela acção coordenada de mecanismos genéticos.

Cílios móveis embrionários participam neste processo ao gerarem um fluxo direcional do fluido interno do órgão de assimetria do peixe-zebra, denominado Vesícula de Kupffer (VK). A correcta formação do eixo E-D depende de vias de sinalização a jusante de tal fluxo, no entanto carece uma caracterização detalhada de como essa dinâmica modula estes mecanismos.

Neste projecto, medições do fluxo do fluido foram obtidas em quatro genótipos: embriões *selvagens* (WT), mutantes *deltaD^{-/-}*, morfolino-injectados (MO) *Dnah7* e MO-controlo. *Dnah7* é uma dineína de cadeia pesada situada no lado interno dos microtúbulos do axonema e a sua ausência tornou os cílios imóveis quebrando o fluxo direcional do fluido da VK. Acompanhando o desenvolvimento de cada embrião, mostramos que a dinâmica do fluido na VK é assimétrica, fornecendo uma previsão da lateralidade dos órgãos.

Neste trabalho caracterizamos uma nova população de cílios móveis, uma população imóvel, uma variedade de frequências de batimento e comprimentos ciliares, volumes da VK e número de cílios em embriões vivos. Subsequentes simulações de dinâmicas de fluido sugerem que o fluido em embriões com 30 ou mais cílios produzem *situs solitus*; com menos cílios, a posição correcta dos órgãos pode ser comprometida através da disrupção do agrupamento de cílios móveis presente na região dorsal anterior. Estimativas aproximadas baseadas num limiar de 30 cílios predizem 90% e 60% *situs solitus* em WT e *deltaD^{-/-}*, respectivamente, como observado experimentalmente. O número e agrupamento ciliar são por isso decisivos para formar um *situs* correcto através de um robusto fluxo assimétrico. Assim, os nossos resultados suportam um modelo em que forças de fluxo assimétricas presentes na VK padronizam a lateralidade dos órgãos em embriões.

Palavras chave: Vesícula de Kupffer, cílios móveis, fluxo da KV, assimetria esquerda-direita, *dnah7*, mutante *deltaD^{-/-}*.

General index

Acknowledgments	vii
Abstract	ix
Resumo	xi
General index	xi
Figures index	xv
Tables index	xvii
1. Introduction	1
1.1. Cilia and Flagella	2
1.1.1. Cilia classification	4
1.1.2. Dynein-based ciliary motility	6
1.2. Cilia defects and ciliopathies	7
1.2.1. Primary cilia dyskinesia	8
1.3. Left-right patterning asymmetry	10
1.3.1. An asymmetric cascade of signals	10
1.3.2. The role of the node in establishing L-R asymmetry in early mouse development	11
1.3.3. The two left-right models	13
1.3.4. Left-Right asymmetry in zebrafish	15
1.3.4.1. Zebrafish Kupffer's vesicle	15
1.3.4.2. Motile cilia generated flow in Kupffer's vesicle	17
1.3.4.3. Fluid hydrodynamics	18
1.3.4.4. Directional flow	19
1.4. Project goals	21

2. Materials and Methods	23
2.1. Zebrafish mating	24
2.2. Recording of cilia beat frequencies in the Kupffer's Vesicle	24
2.2.1. Mounting zebrafish live embryos for KV imaging	24
2.2.3. Microscope setup	25
2.2.4. Recording KV cilia – image acquisition	25
2.2.5. Image processing and kymograph design	26
2.2.6. CBF spectral analysis	27
2.2.7. Kupffer's vesicle fluid flow velocity measurements	28
2.3. In silico experiments - Mathematical modeling	29
2.4. Molecular study of the motility gene <i>dnah7</i>	30
2.4.1. Morpholino antisense oligonucleotides knockdown	30
2.5. Generating transparent zebrafish	31
2.5.1. Zebrafish heart and gut laterality screening	32
2.6. Imaging KV cilia by immunostaining	32
2.7. Cilia length measurements	33
2.8. Cilia localization inside the Kupffer's vesicle	33
2.9. Kupffer's vesicle volume measurements	33
2.10. Whole-mount in situ hybridization	34
2.11. Statistical analyses	35
3. Results	37
3.1. Cilia Beat Frequency studies	38
3.1.1. CBF analysis in WT and <i>deltaD</i> ^{-/-} embryos identifies three cilia populations	38
3.2. Molecular study on <i>dnah7</i> motility gene downstream of DeltaD	42
3.2.1. <i>dnah7</i> knockdown in zebrafish rendered immotile cilia	43
3.2.2. Immunofluorescence experiments in <i>dnah7</i> -MO injected embryos	45
3.2.3. Time-course study of the expression pattern for <i>dnah7</i>	46
3.2.3.1. <i>dnah7</i> gene expresses in ciliated organs during zebrafish embryogenesis	46

3.2.3. Zebrafish heart and liver laterality screening	48
3.3. Kupffer's vesicle fluid flow velocity measurements	50
3.3.1. $\Delta D^{-/-}$ mutant embryos and <i>dnah7</i> morphants generated a range of flow patterns	50
3.4. In silico flow studies	56
3.4.1. Cilia number variations affect KV fluid flow	58
4. Discussion	63
References	71
Annex I	79
Annex II	87

Figures index

Figure 1.1 - Schematics of a 9 + 2 configuration cilia	2
Figure 1.2 - Diversity of cilia number, length and disposition	3
Figure 1.3 - <i>Chlamydomonas reinhardtii</i> flagella	3
Figure 1.4 - Intraflagellar transport machinery	4
Figure 1.5 - The architecture of primary and motile cilia	5
Figure 1.6 - Organs affected in human Ciliopathies	8
Figure 1.7 – Organ laterality defects in PCD human patients	9
Figure 1.8 – Nodal pathway activity in the determination of L–R asymmetry	11
Figure 1.9 – Scanning Electron micrographs of a mouse node	12
Figure 1.10 - Schematic representation of the two L-R models	14
Figure 1.11 – Adult zebrafish	15
Figure 1.12 – Images of zebrafish KV and cilium	16
Figure 1.13 - Pumping flow with motile cilia at low Reynolds numbers	19
Figure 2.1 - Snapshot image of a KV beating cilium in a live embryo	27
Figure 2.2 - Kymograph showing a cilium beating pattern	27
Figure 2.3 – Characterization of KV cilium motility	28
Figure 3.1 – WT cilia population with single CBFs	39
Figure 3.2 – WT cilia population with double CBFs	40
Figure 3.3 – <i>deltaD</i> ^{-/-} cilia population with single and double CBFs.	41
Figure 3.4 – KV of a live embryo with 14 hpf using fluorescent confocal microscopy	41

Figure 3.5 - Characterization of the wild-type and <i>deltaD</i> ^{-/-} KV cilia populations	42
Figure 3.6 – <i>dnah7</i> -MO cilia population with single CBFs	44
Figure 3.7 – Immunofluorescence experiment for visualizing KV cilia	45
Figure 3.8 - Cilia length measurements in WT and <i>dnah7</i> morphants	45
Figure 3.9 – WISH experiment for <i>dnah7</i> gene in WT bud and 8 th somite stage embryos	46
Figure 3.10 - WISH experiment for <i>dnah7</i> gene in WT 16 hpf	47
Figure 3.11 - WISH experiment for <i>dnah7</i> gene in WT 24 hpf	47
Figure 3.12 - WISH experiment for <i>dnah7</i> gene in WT 48 hpf hpf	48
Figura 3.13 - Screening of heart and liver orientation in WT and <i>deltaD</i> ^{-/-} embryos	49
Figure 3.14 - Screening of heart and liver orientation in <i>dnah7</i> morphant and MO-Control embryos	49
Figure 3.15 - Representative KV flow maps	51
Figure 3.16 - Gut laterality at 50 hpf	51
Figure 3.17 - Genetically generating a range of fluid flow speeds	52
Figure 3.18 - Experimental flow measurements	54
Figure 3.19 - Cilia length distribution in WT and <i>deltaD</i> ^{-/-}	56
Figure 3.20 - Cilia number distribution in WT and <i>deltaD</i> ^{-/-}	57
Figure 3.21 - Experimental measurements for KV volume of WT and <i>deltaD</i> ^{-/-} mutant embryos	58
Figure 3.22 - Generating a detailed computational mesh of Kupffer's Vesicle	59
Figure 3.23 - <i>In silico</i> experiments	60

Tables index

Table 2.1 - WISH experiment	35
Table 3.1 - Screening of organ <i>situs</i> in <i>dnah7</i> morphant embryos	55

CHAPTER 1

Introduction

1.1. Cilia and Flagella

Cilia and flagella are hair-like organelles that project from the cell surface, having been implicated in a diversity of cell functions such as cellular motility, signal transduction and embryonic development (Fliegeauf *et al.*, 2007). They are evolutionarily ancient organelles, the structure and function of which is highly conserved from unicellular organisms to higher vertebrates (Ibañez-Tallon, 2003). Typical cilia and flagella are motile, but they vary in number per cell, length and in the patterns of motility that they produce. The first light microscope observations of beating cilia were done by Anton van Leeuwenhoek on ciliated protozoa in 1675 (reviewed by Gibbons, 1981).

Their typical main structure is the axoneme, a cylinder of nine doublet microtubules surrounding a central pair of microtubules covered by the cell membrane, referred to as a “9+2” configuration (Mitchell, 2007). As shown in Figure 1.1, each doublet microtubule consists of A and B tubules: the A tubule is a complete microtubule with 13 protofilaments, while the B tubule contains 10 protofilaments. Moreover, the nine doublets assemble from a much shorter cylinder of nine triplet microtubules, a modified centriole named basal body, which is anchored to the cell surface and stabilized in the cytoplasm by other cytoskeletal elements (Vincensini *et al.*, 2011).

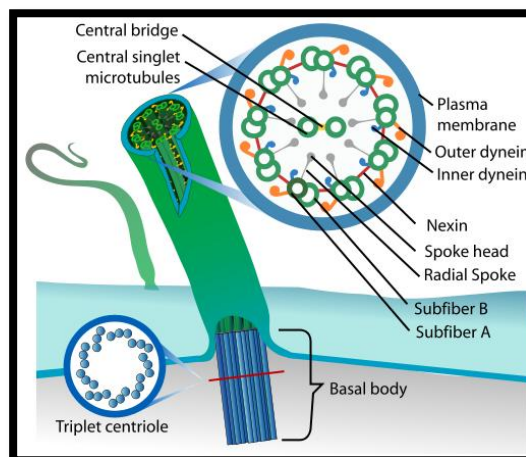


Figure 1.1 – Schematics of a 9 + 2 configuration cilia. Representation of a basal body and a cross section of a 9+2 axoneme. Adapted by Bloodgood *et al.* (2010)

Although cilia and flagella are functionally the same, they were given different designations before their structures were studied. Typically, cells possess one or two long flagella, whereas ciliated cells have many short cilia (Vincensini *et al.*, 2011). For example, the mammalian spermatozoon has a single flagellum, the unicellular green alga *Chlamydomonas* has two flagella (Figure 1.2a), and the unicellular protozoan *Paramecium* (Figure 1.2b) is covered with a few thousand cilia, which are used both to move and to bring in food particles. In mammals, epithelial cells of the respiratory passages are ciliated in order to clean debris across the tissue surface (Figure 1.2c).

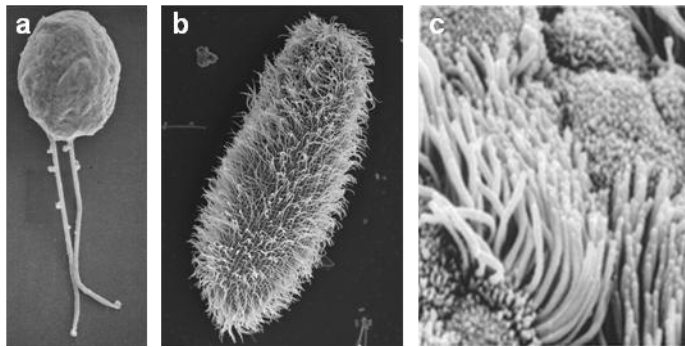


Figure 1.2 – Diversity of cilia number, length and disposition. Scanning electron micrograph of: a - *Chlamydomonas reinhardtii* cell with two motile flagella with 12 μm in length (Silflow and Lefebvre, 2001); b - *Paramecium tetraurelia* covered by motile cilia (Hayes *et al.*, 2007); c – Motile cilia in mammalian trachea (Badano *et al.*, 2006).

Historically, the flagellum axonemal structure has been studied using *Chlamydomonas* as model organism which has predominated in these analyses for over 30 years. *Chlamydomonas reinhardtii*, a unicellular, biflagellate green alga, presented unique advantages for studying eukaryotic flagella and basal bodies (Figure 1.3). These cells use flagella for swimming and for cell-cell recognition during mating, and by being situated on the surface of the cell allows them to be easily isolated for biochemical analysis (Silflow and Lefebvre, 2001).

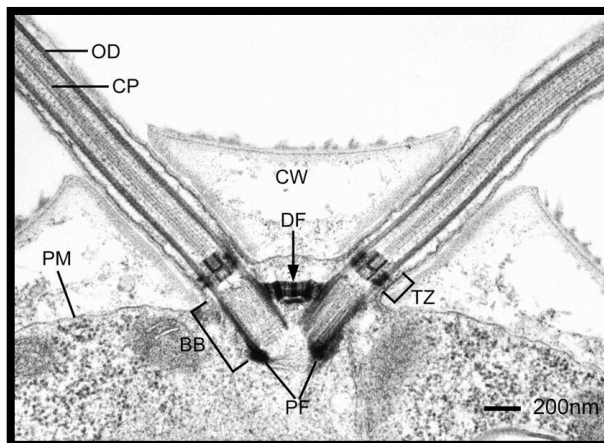


Figure 1.3 - *Chlamydomonas reinhardtii* flagella. Longitudinal section through the basal bodies and flagella of *Chlamydomonas reinhardtii*. CW, cell wall; PM, plasma membrane; OD, outer doublet microtubule; CP, central pair microtubules; BB, basal body; DF, distal striated fiber; TZ, transition zone; PF, proximal fiber connecting the two basal bodies. Electron micrograph, by Dentler (1991) adapted by (Silflow and Lefebvre, 2001).

From these studies we found that eukaryotic flagella are composed of more than 200 proteins which most of the components are also present in mammalian cilia (Ibañez-Tallon *et al.*, 2003). Moreover, this model organism along with other ciliates, such as *Paramecium* and *Tetrahymena*, were especially important to understand processes involved in ciliogenesis and motility processes (Silflow and Lefebvre, 2001; Vincensini *et al.*, 2011).

Ciliogenesis is a multistep process that is tightly coordinated with cell cycle progression and differentiation. The ciliary axoneme extends from the basal body which initially migrates to and docks onto the apical plasma membrane as cells enter growth arrest. Meanwhile, the axoneme elongation is controlled via intraflagellar transport (IFT), a bidirectional transport system that follows along the polarized microtubules of the axoneme, and which is required for assembly of cilia and flagella (Mitchel, 2007). This transporting process occurs between the doublets and the membrane, involving the rapid movement of particle components toward the tip (anterograde movement) or the base (retrograde movement) of the cilia, powered by motor proteins crucial for cilia assembly and protein trafficking in this cellular compartment (Vincensini *et al.*, 2011). In the anterograde direction, IFT is

powered by kinesins of the kinesin2 family while in the retrograde direction, power is provided by dyneins of the cytoplasmic dynein 2 family (Figure 1.4).

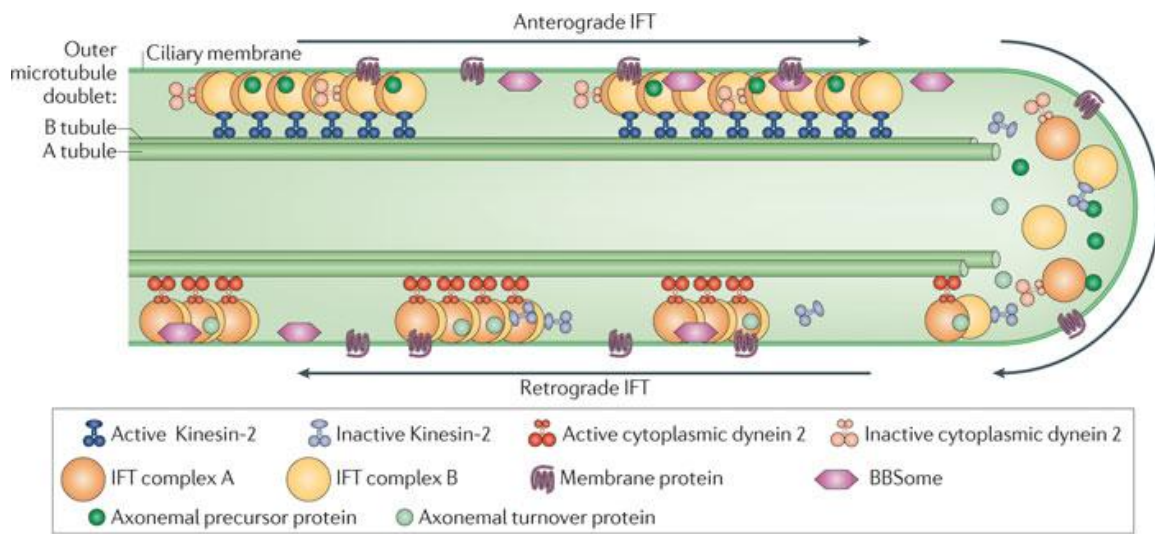


Figure 1.4 – Intraflagellar transport machinery. The canonical anterograde intraflagellar transport (IFT) motor, heterotrimeric Kinesin-2, transports IFT complexes A and B, axonemal proteins and cytoplasmic dynein 2 to the tip of the cilium. During this anterograde motion, Kinesin-2 is active and the retrograde motor, cytoplasmic dynein2, is kept inactive to allow smooth processive anterograde movement. At the tip of the cilium, anterograde IFT trains release axonemal proteins and rearrange their conformation for retrograde IFT. Cytoplasmic dynein 2 is activated and transports retrograde IFT trains to the cell body. Figure from (Ishikawa and Marshall, 2011).

Moreover, despite their overall structural similarities, the specialization of cilia for particular functions has resulted in significant variations of structure and regulation.

1.1.1. Cilia classification

Cilia and flagella are virtually equivalent in structure and function (hereafter called cilia, there being no consistent difference between organelles with these two designations) and can be divided into two categories: primary and motile cilia (Figure 1.5).

Primary cilia are single, usually non-motile, organelles that emanate from the cell surface of most cell types (Figure 1.5a-d), including stem, epithelial, endothelial, connective-tissue and muscle cells as well as neurons (Satir *et al.*, 2010; Vincensini *et al.*, 2011).

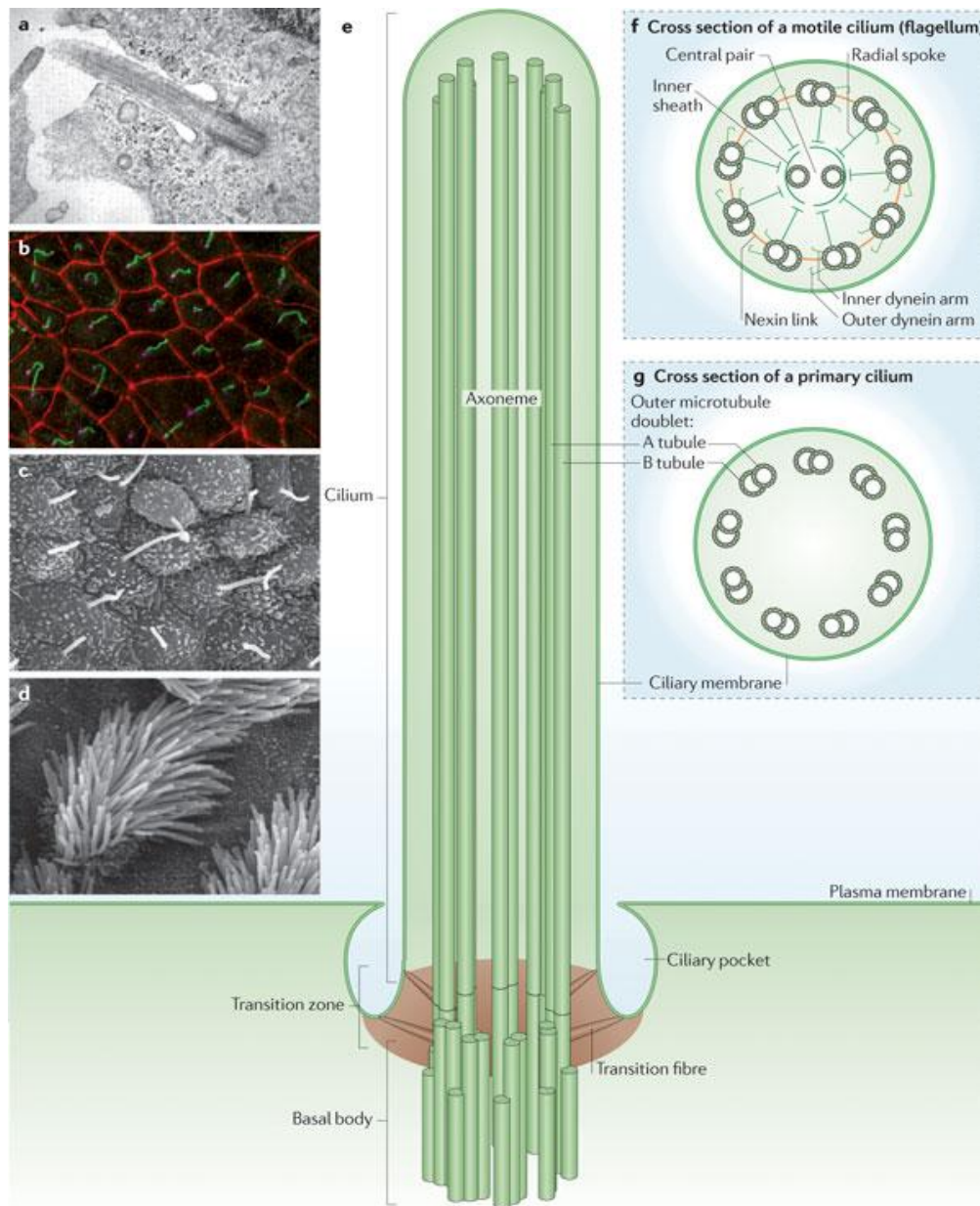


Figure 1.5 – The architecture of primary and motile cilia. a – Transmission electron micrograph of the primary cilium of retinal pigment epithelial cells; b – Immunofluorescence image of primary cilia in inner medullary collecting duct cells. The cilium (green) is produced once per cell and extends from the basal body (magenta). Cell-cell junctions are shown in red; c,d – Scanning electron micrographs of mouse nodal cilia (c) and mouse tracheal motile cilia (d); e – Schematic diagram of the primary cilium; f,g – Cross section diagrams of a typical motile cilium (f) and a non-motile primary cilium (g). Figure and legend from (Ishikawa and Marshall, 2011).

Cilia were initially thought to be vestigial, but recent findings failed this hypothesis and linked primary cilia to a major cell signaling function (reviewed by Singla and Reiter, 2006) due to presence of a variety of receptors, such as ion channels and transporter proteins, as well as some of their downstream effector molecules, in the cilium and basal body.

Signaling in the cilium coordinates crucial processes during development and in tissue homeostasis, including cell migration, differentiation and/or re-entry into the cell cycle, specification of the plane of cell division, and apoptosis. Sensory modalities to which the primary cilium responds

include mechanical stimulation (transduction of the fluid flow forces through cilium bending) and chemosensation (recognition of a specific ligand, growth factor, hormone or morphogen). This significance of primary cilia in signaling became clear with the implication of its defective function on specific organ diseases and developmental disorders, commonly referred to as ciliopathies.

In contrast to the typical axonemal organization of doublet microtubules, primary cilia have absence of the central pair of microtubules (“9+0” axoneme, Figure 1.5g) along with other interconnecting multiprotein complexes, contributing this way to its non-motility (Singla and Reiter, 2006). However, these cilia are far more widespread than the motile type. For example, in humans, only a few cell types have motile cilia, namely sperm, epithelial cells in the bronchi and oviducts, and ependymal cells that line brain vesicles. In contrast, virtually all other cells have a primary cilium.

Motile cilia are normally found at high density at the surface of the cells, beating in a synchronized manner to direct fluid movement (Vincensini *et al.*, 2011). Most of these cilia present a “9+2” axoneme structure (Figure 1.5f) and within the microtubule core there are a number of multiprotein complexes that interconnect the different components (Ibañez-Tallon, 2003). Among these are radial spokes, nexin links, central sheath and dynein arms (Figure 1.1). The dynein arms, which are divided in outer dyneins (ODA) and inner dyneins (IDA), are attached to the peripheral microtubules with certain periodicity and generate motion by ATP-dependent reactions. The other components, mainly the central apparatus and radial spokes, provide the structural interface for conducting regulatory signals to the dynein arms (Porter and Sale, 2000).

1.1.2. Dynein-based ciliary motility

To appreciate the molecular architecture of the cilium is crucial to elucidate the beating mechanism produced by this complex organelle. However, the current known structure of the cilium has not yet been fully correlated with the complex composition and localization of ciliar components needed for this process.

Mediating motility requires cilia to have an intrinsic structure axoneme, which consists in dynein arms, the molecular motors essential for the beating of these organelles. Dyneins are composed of multiple subunits thought to be preassembled in the cytoplasm before they are transported into the cilium (Fowkes and Mitchell, 1998). These called dynein arms are large protein complexes (Kobayashi and Takeda, 2011) comprising several heavy (HC of 400–500 kDa), intermediate (IC of 45–110 kDa) and light chains (LC of 8–55 kDa). Within these multiprotein assemblies, the ATPase activity that resides in the HC molecules provides the energy to produce the sliding movement between microtubules, which results in the beating of the cilium (Porter and Sale, 2000). Moreover, the capability of dynein arms to function as microtubule-based molecular motors requires the integrity of many dynein components.

Studies conducted in *Chlamydomonas* mutant strains indicate that 30–40 axonemal dyneins combine to form different dynein arms (reviewed by Kamiya, 2002). The outer dynein arms (ODA) are

positioned proximally to the cilia membrane while the inner dynein arms (IDA) are proximal to the central apparatus and have a more diverse composition.

Generation of ciliary beating involves multiple different dynein motors acting in a concerted way to specify the waveform and beat frequency (King and Kamiya, 2009).

From analyses of *Chlamydomonas* ODA and IDA mutants, ODAs appear to be more important for high frequency cilia beating, whereas IDAs are required for the proper formation of ciliary waveforms (Brokaw and Kamiya, 1987; Kamiya *et al.*, 1991). In *Chlamydomonas*, the IDA and ODA are spaced by specific length intervals of 96 nm and 24 nm, respectively, along the axis of each MT pair (Goodenough and Heuser, 1985). Furthermore, these motors must exhibit an integrated response to various signaling factors. This requirement for coordinated action necessitates a complex control mechanism with a response time on the order of 20 ms or less. Additionally, the nexin link, which was identified as the dynein regulatory complex (DRC) (Heuser *et al.*, 2009; Piperno *et al.*, 1992), connects adjacent MT doublets, and the radial spokes connect the outer MT doublets to the central pair (Fig. 2). Both of these structures are thought to regulate ciliary motility.

The motor activity of dyneins is also regulated by several other components (Supatto and Vermot, 2011; Heuser *et al.*, 2012): the radial spokes, which are projections originating from each peripheral doublet and directed towards the central pair; the projections associated with the central pair; and the dynein regulatory complex, which is constituted by the nexin links. The basis for axonemal movement is the sliding of microtubules relative to one another (Supatto and Vermot 2011). Dynein-generated forces that cause sliding between pairs of doublet microtubules produce axonemal bending because axonemal microtubules are anchored to the cell via the basal bodies (Supatto and Vermot 2011; Heuser *et al.*, 2012). Despite of all the advances, the dynamics of the dynein motor itself need to be better understood.

The loss of proteins involved in this process results in cilia dysmotility. Studies of human ciliopathies have contributed to our understanding of the cilia beating process.

1.2. Cilia defects and ciliopathies

Ciliated cells can be found in various tissues throughout the human body. These include the eye, the trachea, the kidney, the reproductive tract, the intestines, the heart, and many others. In each of these tissues, the cilia perform a significant role in allowing proper function of the tissues.

Not surprisingly, there is an increasing appreciation for the vital role played by the cilium organelle in diverse developmental processes and homeostasis in vertebrates. Consistently, cilia dysgenesis and dysfunction have been linked to a growing list of human pleiotropic disorders, collectively referred to as ciliopathies. These ciliary diseases cause multisystem pathology, resulting in very low quality of life and early death for many patients. Some major ciliopathies include Primary Ciliary Dyskinesia (PCD), Hydrocephalus, Polycystic Kidney Disease (PKD), Bardet-Biedl Syndrome (BBS), and even cancer (Hildebrandt *et al.*, 2011).

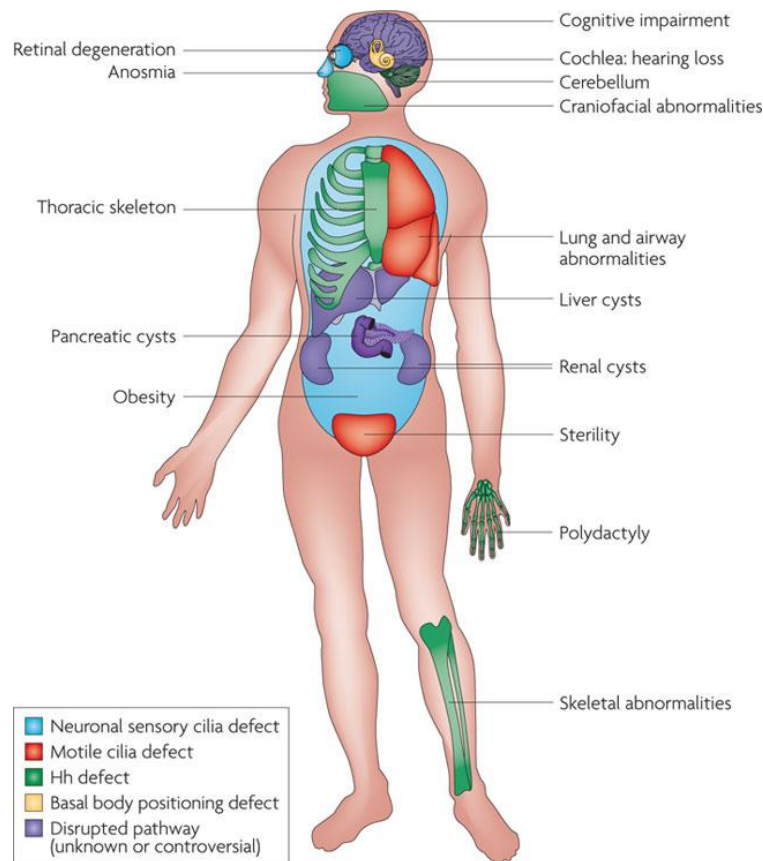


Figure 1.6 - Organs affected in human Ciliopathies. Numerous pleiotropic human disorders have been attributed to defects in cilia formation. Some aspects of these syndromes have been attributed to defective hedgehog (Hh) signalling. Other attributes of human disorders result from defective specialized cilia. Infertility observed in patients with ciliopathies is the result of defective sperm flagella and motile oviduct cilia. Figure adapted from (Goetz and Anderson, 2010).

The role of motile cilia in a number of physiological processes has been long accepted and thus the consequences of motile cilia dysfunction have four major manifestations in mammals: early embryonic death due to failure of embryonic turning; respiratory dysfunction; reproductive sterility; and hydrocephalus (Badano *et al.*, 2006) (Figure 1.6). Ciliary dysfunctions involving motile cilia also result in body laterality defects (McGrath, 2003), like *situs inversus* (Afzelius, 1976). However, not all ciliopathies are related to motile cilia, some are based in defects occurred in primary cilia, like PKD (Polycystic Kidney Disease), BBS (Bardet–Biedl Syndrome), Joubert Syndrome, Oral-Facial-Digital Syndrome, Alström Syndrome or Meckel Gruber Syndrome (Fliegauf *et al.*, 2007; Vincensini *et al.*, 2011). In this study we will focus on motile cilia and on motile cilia ciliopathies.

1.2.1. Primary cilia dyskinesia

Among ciliopathies, a motility defect involving the cilia, referred to as primary ciliary dyskinesia (PCD) is characterized by recurrent respiratory tract infections, sinusitis, bronchiectasis and male

infertility. Approximately 50% of patients with PCD also have *situs inversus*, a condition in which the major visceral organs are reversed from their normal positions (Ibanez-Tallon *et al.*, 2003), thereby defining the Kartagener Syndrome.

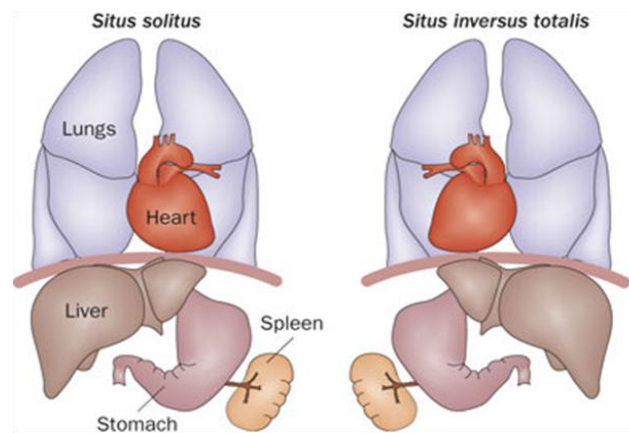


Figure 1.7 – Organ laterality defects in PCD human patients. Normal left-right asymmetry (*situs solitus*) and *situs inversus*. Figure from (Patel and Honoré, 2010).

PCD is a rare genetic condition, usually autosomal recessive, affecting approximately 1 in 15,000 people (Bush *et al.*, 2007; Afzelius, 2004;).

One of the typical causes of motility defects is due to a range of ultrastructural ciliary axoneme defects, more than 70% involving loss of the outer dynein arms (Papon *et al.*, 2010). Inner dynein arms defects also have been involved in this disease where isolated absence of the IDA is reported to cause between 10 and 29% of PCD cases (Chilvers *et al.*, 2003; Carda *et al.*, 2005).

Ciliary motility seems to be linked to the type of ciliary defects: most of the cilia become immotile when both dynein arms and outer dynein arms are affected while the ciliary beating pattern seems atypical with reduced amplitude in case of inner dynein arm defects (Chilvers *et al.*, 2003). Recently, Shoemark *et al.* (2013) also showed that depletion of inner dynein arms can also render completely immotile cilia.

The diagnosis of PCD is based on the identification of functional and structural abnormalities of cilia by TEM or/and by abnormal ciliary function (Bush *et al.*, 2007; Armengot *et al.*, 2012). In most patients with PCD, all the cilia share the same ultrastructural defect, as expected for a congenital disease.

However, depending on the patients, cilia have been shown to carry various axonemal abnormalities. In 10–20% of patients with PCD and *situs inversus*, no ultrastructural defects can be found through conventional electron microscopy, although cilia are immotile (Afzelius, 2004). For these reasons, the diagnostic validity of the ultrastructural study is limited (Bush *et al.*, 2007), and has been complemented by high-speed videomicroscopy (Armengot *et al.*, 2012).

Ordinarily cilia beat in a coordinated fashion at 11-15 Hz clearing secretions from the respiratory tract (Chilvers *et al.*, 2003), and any mean frequency less than 10 Hz is considered

abnormal. At present, guidelines and algorithms have been developed to standardize diagnostic procedures (Bush *et al.*, 2007) in order to improve the PCD diagnostics.

The ciliary genome is highly conserved throughout the phylogenetic spectrum from simple unicellular eukaryotes to mammals, which supported the identification of the causative genes in PCD. Studies carried out in the green algae *Chlamydomonas reinhardtii* established the link between cilia and several genetic diseases (Vincensini *et al.*, 2011). By the end of the 20th century, DNAI1, the human ortholog of the *Chlamydomonas reinhardtii* gene IC78, was identified as the first gene involved in PCD (Pennarun *et al.*, 1999), thus emerging a novel field of research to interpret the pathophysiology of this complex disorder. Also, despite the respiratory insufficiency of these patients could be correlated with ultrastructural defects in their airway motile cilia (Afzelius, 1976), the rising question of how ciliary abnormalities are responsible for the incorrect positioning of visceral organs opened a subject of intense research interest.

1.3. Left-right patterning asymmetry

The external body plan of vertebrates is bilaterally symmetric, but several internal organs, including the heart, digestive organs and regions of the brain, display highly conserved left-right (L-R) orientations that are crucial for their functions.

Strikingly, however, these gross anatomical asymmetries arise in early embryos that are bilaterally symmetrical along the mediolateral axis. A couple decades ago, nothing was known about the molecular or genetic underpinnings of left-right asymmetric morphogenesis, and no genes with left-right asymmetric expression had been identified. Since then several discoveries have led to an emerging picture of how left-right asymmetry is initiated, stabilized, propagated, and translated into asymmetric organogenesis during development of vertebrate embryos.

1.3.1. An asymmetric cascade of signals

In the mid-1990s, studies from several groups showed that asymmetric expression of genes during early embryogenesis forecasted the development of morphological asymmetry of the vertebrate body (Collignon *et al.*, 1996; Levin *et al.*, 1995; Meno *et al.*, 1996). In the mouse embryo, one of those genes, *Nodal*, is primarily expressed throughout the node, a transient embryonic cavity that forms at the end of the developing notochord, which then becomes limited to the left side of the node (Collignon *et al.*, 1996) (Figure 1.8). On the contrary, its antagonist, the secreted molecule Cerberus-like 2 (*Cerl2*), is expressed with the opposite predisposition. The left-sided expression of *Nodal*, which encodes a member of the transforming growth factor beta (TGF β) family of secreted signaling proteins, then extends to the tissue adjacent to the node, the lateral plate mesoderm (LPM), where *Nodal* induces its own expression, as well as that of *Lefty1/2* and *Pitx2*. Like *Nodal*, *Lefty1/2* encodes

members of the TGF β family that competitively bind to a class of Nodal receptors. Biochemically, Lefty2 exists as a monomer, in contrast to Nodal, which functions as a dimer. This property allows Lefty2 to diffuse faster and farther than Nodal, thereby limiting the Nodal activity to the left side. On the other hand, Pitx2, a paired-like homeodomain transcription factor, acts as the effector of Nodal signaling.

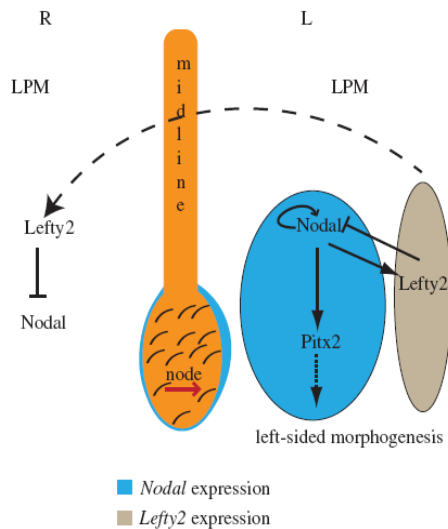


Figure 1.8 – Nodal pathway activity in the determination of L–R asymmetry. A simplified schematic depicting asymmetric Nodal expression in the node, and the essential elements of asymmetric Nodal signaling in the left LPM. Figure from (Babu and Roy, 2013).

Thereby, Pitx2 has been proposed as a controller of the subsequent asymmetric morphogenetic events by regulating the gene expression mechanism essential for left-sided morphogenesis (Hamada *et al.*, 2002).

It is known that members of the nodal and lefty cell-signaling families and pitx2 also display similar asymmetric expression patterns in the lateral plate mesoderm in chick, frog and zebrafish embryos, but how does the asymmetric pattern of Nodal pathway genes get established in the first place?

1.3.2. The role of the node in establishing L-R asymmetry in early mouse development

The fact that the earliest asymmetrically expressed genes are at the node increased the interest for this structure as a region where the initial left-right decision might be made.

Several studies conducted in mouse indicated that the node plays an important role in the establishment of L-R asymmetry (Nonaka *et al.*, 1998; Okada *et al.*, 2005), being the reason why this organ is also called the L-R organizer. The mouse node (Figure 1.9) is found at the rostral end of the primitive streak. It consists dorsally of epiblast and ventrally of the most caudal aspect of the notochordal plate (Brennan *et al.*, 2002). The node generates midline structures such as the

notochord and floor plate that act as a midline barrier required for preserving the correct laterality (reviewed in Brennan *et al.*, 2002). Remarkably, the cells on the ventral surface of the mouse embryo node each have a motile monocilium projecting from their apical surface that have a clockwise rotator beating pattern.

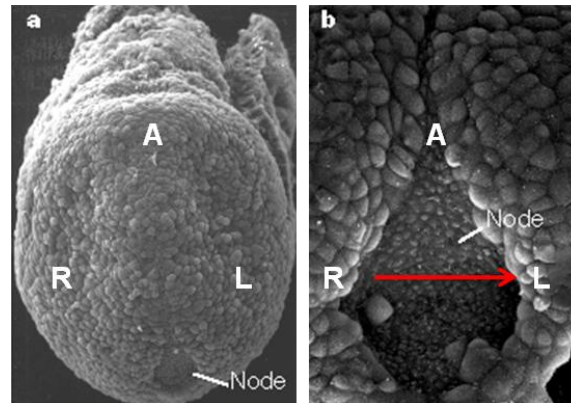


Figure 1.9 – Scanning Electron micrographs of a mouse node. a – The node is at the apex of the egg cylinder, and the head process, which give rise to the notochord, extends anteriorly. b – Close-up showing the cup-like shape of the node. The cilia motility generates a leftward fluid flow (red arrow). The anterior (A) is oriented to the top. Figure adapted from (Vogan and Tabin, 1999).

Furthermore, a model has been suggested in which monocilia projecting from cells in the late gastrula node produce an asymmetric flow of extracellular fluid, known as ‘Nodal flow’ (Figure 1.9b), which results in the determination of asymmetric gene expression (Nonaka *et al.*, 1998). This ‘nodal flow’ model was first sustained from the analysis of mutant mice that were deficient in genes encoding kinesin proteins. Kinesins, which are enzymes that move along microtubules and contribute in the trafficking of a range of cargoes within the cell, are also required for the assembly of cilia in a process called intraflagellar transport. So in this case, the mice mutants for the kinesin genes *Kif3a* or *Kif3b* were unable to assemble cilia, and, remarkably, approximately 50 per cent of the mutant embryos showed *situs inversus*, similar to patients afflicted with Kartagener Syndrome (Nonaka *et al.*, 1998; Takeda *et al.*, 1999). Certainly, the expression of *Lefty2* in the LPM was disrupted, suggesting that the initial molecular events in the determination of L–R development were affected. Moreover, some groups reported that the node in normal embryos have motile monocilia that beat in a clockwise rotary pattern (when viewed from the ventral side) which drive the ‘nodal flow’, whereas cilia and directional fluid flow were completely absent in the *Kif* mutant embryos (Nonaka *et al.*, 1998; Takeda *et al.*, 1999). These notable observations suggested that cilia-driven nodal flow is an essential epigenetic signal that initiates L–R asymmetry. Posterior work (Supp *et al.*, 1997) supported this view through the analysis of the *inversus viscerum (iv)* mutant mice. The *iv* locus encodes a member of the dynein family—left–right dynein (Lrd), a protein that is required for ciliary motility (Okada *et al.*, 1999; Supp *et al.*, 1999). Cilia were present normally in the *iv* mutant mice, however the deficiency of Lrd turned them immotile. In result, these mice failed to establish a leftward flow which then translated to a randomization of L–R asymmetry.

The strongest arguments for a role for nodal flow in the establishment of L-R asymmetries come from cultured mouse embryos in which externally applied rightward fluid flow is capable of reversing L-R patterning in wild-type (WT) embryos and externally applied leftward flow is able to rescue L-R patterning in mutants that would normally have inverted L-R orientation (Nonaka *et al.*, 2002). Also, submitting *iv* mutant embryos to external flow restored their normal *situs*, which otherwise would have developed randomized asymmetry. But how do a directional nodal flow functions in establishing L-R asymmetry?

1.3.3. The two left-right models

Since the discovery of nodal flow, two hypotheses have evolved to explain the mechanism by which L-R is transferred to the LPM.

The first of these was named the 'morphogen hypothesis'. It proposes that directed motion of the nodal cilia leads to a unidirectional transport of a secreted morphogen to the left side of the node (Nonaka *et al.*, 1998; Okada *et al.*, 1999). This simple model suggests that ciliary beating guarantees that one side of the node preferentially receives greater concentration of a morphogen than the other side (figure 1.10a). Thus, the asymmetry in the distribution of the morphogen then triggers signaling events that strengthen the asymmetry in the developing embryo. However, this hypothesis raises several questions, primarily among them being the identity of the morphogen itself. Later evidences came in this direction from the work of Tanaka *et al.* (2005). This group observed flowing objects inside the node cavity. These particles, which they termed nodal vesicular parcels (NVPs), were seen to be released into the flow and to fragment upon contact with the ciliated surface, thereby releasing their contents on the left side of the node. But which is the nature of this putative morphogen? Tanaka *et al.* (2005) also found that Sonic Hedgehog (Shh) and Retinoic acid (RA) are associated with the NVPs, and are released into the nodal flow in a fibroblast growth factor (FGF)-signaling-dependent manner. Based on these findings, Cartwright and colleagues (Cartwright *et al.*, 2006) modeled the movement of NVPs across the mouse node and verified that the flow could definitely cause them to accumulate on the left side of the node, which would be needed for symmetry breaking. However, based on the biophysical properties of node such as high viscosity of the fluid, they disagreed that the morphogens could be delivered to the surrounding cells by their mechanical rupture either by the action of cilia or the flow. Alternatively, they hypothesize that if there is rupture it must be induced by a biochemical mechanism not yet discovered (Cartwright *et al.*, 2006).

Regardless of these fascinating findings, the NVP model of the 'morphogen hypothesis' has not been further supported. Most importantly, genetic analysis of Sonic Hedgehog and the Retinoic acid pathways do not supply convincing support of their roles as nodal flow morphogens (Vermot *et al.*, 2005; Zhang *et al.*, 2001).

The second model is called the 'two-cilia hypothesis' and suggests that the beating of the motile cilia generates a leftward fluid flow, which can be sensed by immotile cilia (figure 1.10b). Therefore, this hypothesis adds an additional level of complexity to ciliary function in the node by

dividing the 'nodal flow' process into two steps: generating the flow, and responding to the flow by two distinct kinds of cilia.

The work that suggested cilia could be implicated in the generation and also the sensation of nodal flow came from the known function of the polycystic kidney disease 1 (*Pkd1*) and polycystic kidney disease 2 (*Pkd2*) genes in the kidney tubule cells - the proteins encoded by these genes form a functional mechanosensory complex that detects urine flow and gives rise to a Ca^{2+} signal response (Nauli *et al.*, 2003).

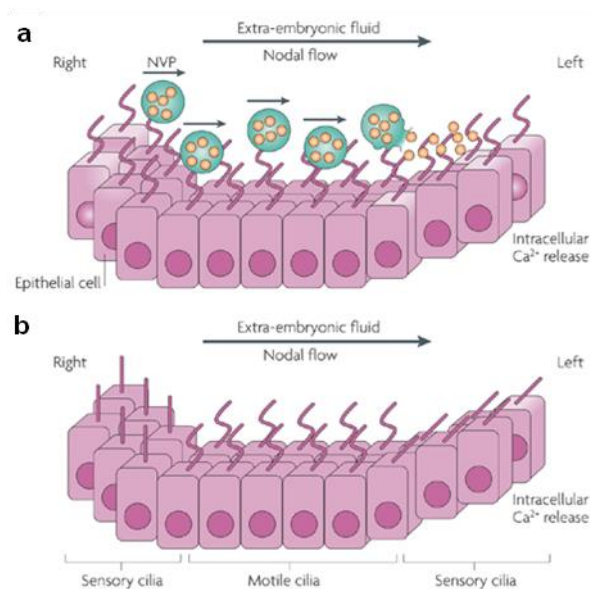


Figure 1.10 – Schematic representation of the two L-R models. a - 'morphogen model' – NVPs appear to be released from dynamic microvilli, transported to the left side by the nodal flow, and fragmented with the aid of cilia at the left periphery of the node. b - 'Two cilia model' - non-motile cilia are capable of sensing the mechanical stress of the leftward flow generated by motile cilia. Adapted from (Fliegeauf *et al.*, 2007).

Although *Pkd1* is not required for L-R determination and is not expressed in the node (Tanaka *et al.*, 2005), *Pkd2* mutant mice exhibited many features that illustrate abnormal L–R development, thus involving Ca^{2+} signaling in the establishment of L–R asymmetry (Pennekkamp *et al.*, 2002).

Recently it was discovered that Pkd111 is the functional partner of Pkd2 in the L-R organizer being conserved in medaka and mouse (Field *et al.*, 2011). Additional support of this possibility appeared from the examination of Pkd111-Pkd2 localization on nodal cilia. While Lrd, the dynein protein required for ciliary motility, localized to the motile cilia on the central cells of the node pit, Pkd2 was present on the motile cilia as well as the immotile Lrd-negative cilia on the perinodal cells that surround the node (McGrath, 2003).

Furthermore, in the Kupffer's vesicle (KV) of medaka, which is the fish homologue of the mouse node, where all cilia are visibly motile, it was also proposed that cilia have a double role in producing the characteristic fluid flow and interpreting it through Pkd111-Pkd2 sensor-channel complexes expressed in all cilia (Kamura *et al.*, 2011). In zebrafish it is still not known if pkd111 plays a role in L-R determination, while Pkd2 role is definitely conserved.

Nonetheless, since the molecular sensors of nodal flow are still unknown, both chemosensory and mechanosensory hypotheses are plausible in the L-R organizer.

1.3.4. Left-Right asymmetry in zebrafish

Zebrafish (*Danio rerio*) is a small teleost fish (Figure 1.11) and has emerged as one of the leading models for studying development. As a vertebrate organism, this fish presents many organs and cell types similar to that of mammals (reviewed in Lieschke and Currie, 2007).



Figure 1.11 – Adult zebrafish – wild-type female zebrafish. Scale bar = 4mm. Figure from (Parichy *et al.*, 2009).

The zebrafish embryos are transparent (Figure 1.12) and also develop rapidly (Kimmel *et al.*, 1995), thus, allowing real-time imaging of developing stages in embryos and larvae. In addition zebrafish proved to be more advantageous over previous model organisms in many ways. For example early developmental processes are less accessible in the mouse because they occur *in utero*.

Moreover, an individual female can produce hundreds of eggs in each clutch, enabling huge numbers of progeny to be generated, facilitating the detection of rare mutations.

Through the 1980s, the development of zebrafish genetic techniques, such as ‘cloning’, mutagenesis, transgenesis and mapping approaches, underpinned the use of zebrafish to apply invertebrate-style forward genetics to questions of vertebrate development (reviewed in Lieschke and Currie, 2007).

Over the past decade, the zebrafish has proven to be very useful regarding genetic manipulation of laterality. Studies using zebrafish have also provided insights into how the Kupffer’s vesicle, the fish homologue of the mouse node, relays L-R asymmetry information to the lateral plate mesoderm (Long *et al.*, 2003; Wang and Yost, 2008).

1.3.4.1. Zebrafish Kupffer’s vesicle

Kupffer’s vesicle (KV) is the equivalent to the mouse node ciliated organ of asymmetry in the zebrafish embryo that initiates L-R development of the brain, heart and gut (Essner, 2005). First described in 1868 by *Kupffer*, KV is a conserved structure among teleost fishes. In zebrafish, KV is

formed from the dorsal surface epithelial cells, known as dorsal forerunner cells (DFCs), a group of approximately two-dozen cells that migrate at the edge of the embryonic shield at the beginning of gastrulation. DFCs move to the vegetal pole in close contact with the overlying enveloping layer margin and become transformed into an epithelial vesicle (KV). During subsequent somite stages, KV formation is completed with the generation of motile monocilia on the apical membranes of KV cells facing the lumen (Figure 1.12). It constitutes a small and distinctive epithelial closed vesicle containing fluid, located mid-ventrally posterior to the yolk cell, and is transiently present during most of the segmentation period (Amack *et al.*, 2007; Kimmel *et al.*, 1995; Kramer-Zucker, 2005).

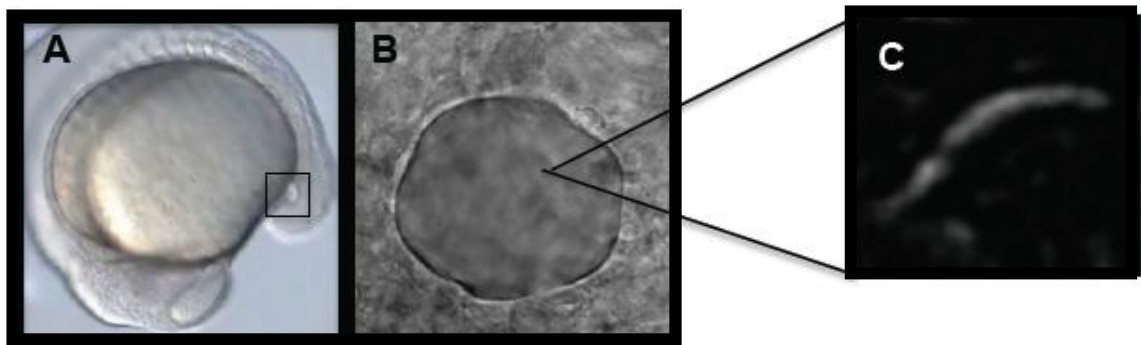


Figure 1.12 – Images of zebrafish KV and cilium. A - Localization of the KV (squared region) in the body of the zebrafish embryo at 14 hpf. B - Snapshot image of a Kupffer's vesicle of a live embryo filmed from the dorsal side. C - Snapshot image of a KV beating cilium in a live embryo.

The monociliated cells lining the epithelium of the KV have a 9+2 arrangement (Kramer-Zucker *et al.*, 2005; Kreiling *et al.*, 2007) and generate a counterclockwise fluid flow. This flow promotes intracellular Ca^{2+} elevation in cells localized on the left side of KV (Francescato *et al.*, 2010; Sarmah *et al.*, 2007) and is involved in establishing and maintaining the L-R asymmetry of the body axis (Essner, 2005; Kramer-Zucker, 2005). Even so, the presence of sensory cilia is still a subject of discussion in the zebrafish (Borovina *et al.*, 2010; Okabe *et al.*, 2008).

At present, it is assumed that KV is analogous to the mouse node in terms of L-R patterning (Essner, 2005). While the ciliated surface of the mouse node is reasonably flat, KV is a hollow sphere containing cilia, projecting both from dorsal roof and ventral floor (Kreiling *et al.* 2007; Amack *et al.*, 2007). Kramer-Zucker *et al.* (2005) reported that cilia rotate counterclockwise when observed from the apical side in the KV, which is contrary to what is observed in the mouse node.

Recent studies in zebrafish have also shed some light on how this KV flow is responsible for the symmetry-breaking. Counterclockwise fluid flow promotes intracellular Ca^{2+} elevation in cells localized on the left side of KV. This induces phosphorylation of Ca^{2+} /CaM-dependent protein kinase II (CaMK-II), to activate both Ca^{2+} release from the endoplasmic reticulum (ER) and extracellular Ca^{2+} influx (Francescato *et al.*, 2010). This positive feedback loop of Ca^{2+} signals may promote processing and/or secretion of Spaw only in the left side of KV. Charon, a member of the Cerberus family, is also contributes to generating Spaw asymmetry around KV (Hashimoto *et al.*, 2004). *Charon* is expressed

bilaterally in KV cells at the 6-somite stage, but its expression changes to a right-sided asymmetric pattern at the 8 to 10 somite stages in a fluid flow-dependent manner (Lopes *et al.*, 2010). Since Charon binds to Spaw and antagonizes Spaw functions (Hashimoto *et al.*, 2004), the rightward gradient of Charon around KV tends to inhibit Spaw strongly in the right side. Due to the opposing gradients of activator (Spaw) and inhibitor (Charon), Spaw cannot stimulate expression of *spaw* on the right side of the LPM. On the other hand, Spaw induces its own expression on the left-side LPM by positive feedback regulation which indicates that opposed gradients between Spaw and Charon around KV may contribute to initiating *spaw* expression in the left-side LPM.

Okabe *et al.* (2008) hypothesized that the fluid flow in zebrafish KV is analogous to the flow in the mouse node and medaka fish in terms of L-R patterning, although the ciliated cell arrangement appear to vary in structure. According to Kamura *et al.* (2011), all medaka KV cilia are motile, whereas in the mouse node McGrath *et al.* (2003) showed the presence of two populations of cilia, one motile and other immotile. In zebrafish, it is still not clear if all cilia are motile.

Although a unidirectional fluid flow is evident in the mouse node, the zebrafish KV has a more intricate internal arrangement of cilia contributing to the generation of a more complex flow that needs to be investigated.

1.3.4.2. Motile cilia generated flow in Kupffer's vesicle

Ciliary beating is characterized by a series of bends, originating at the base of the structure and propagated toward the tip. High-speed microscopy allows the waveform of the beat to be seen and it is currently used as an important tool for diagnosis of ciliopathies such as PCD by studying the cilia beat frequency (CBF).

An important factor dictating cilia-mediated hydrodynamics is the type of beat they generate. Beating can be planar or three-dimensional and it can be described by its amplitude, wavelength, and frequency. The bends push against the surrounding fluid, propelling the cell forward or moving the fluid across a fixed epithelium.

The beat pattern appears to be related with the inner organization of cilia but many unsolved questions remain regarding the correlation of structure and cilia beat in different developing organs.

The nexin link, which was first identified as the dynein regulatory complex (DRC), connects adjacent MT doublets, and the radial spokes connect the outer MT doublets to the central pair. In humans and zebrafish, mutants for the radial spoke heads showed to affect cilia motion (Castleman *et al.* 2009) and that DRC is critical for proper cilia motility in zebrafish (Colantonio *et al.* 2009). These two structures are considered to regulate ciliary motility. In addition, motility requires axoneme-associated dynein arms to generate the sliding of microtubules and thus motion (reviewed in Vincensini *et al.*, 2011).

Vertebrates' cilia with 9+6 structure, which typically beat in a planar whip-like pattern, can significantly bend during its motion with effective and recovery strokes, while 9+0 motile cilia have an approximately circular motion (Bellomo *et al.*, 1996; Nonaka *et al.* 1998; Nonaka *et al.* 2005). This clue

led to the assumption that the absence of the CP apparatus confers the rotary pattern of beating to the node cilia. However, some studies suggest that this interpretation is unlikely to be correct. Teleost fishes such as the zebrafish and medaka also make use of ciliary motility to establish L–R asymmetry (Essner *et al.*, 2005; Kramer-Zucker *et al.*, 2005). In these species, motile cilia exist in Kupffer's vesicle (KV). Although medaka KV cilia are 9+0 and beat in a rotary manner (Okada *et al.*, 2005), the zebrafish has CP-containing KV cilia (9+2 structure), and yet they too demonstrate rotational motion (Kramer-Zucker *et al.*, 2005).

Similarly, contrary to the conventional view, it has been recently reported that the mouse node cilia, which have a circular motion, also contains cilia with CP (Caspary *et al.*, 2007). Thus, the presence or absence of the CP appears not to decide the beating pattern of the cilium.

Moreover, genetic confirmation does favor the hypothesis that the CP is dispensable for nodal cilia motility. In mice and humans, mutation of genes that are necessary for the assembly or function of the CP do not have an affect on laterality, while the planar motility of different 9+2 cilia (such as those in the airways) is strongly affected (Lechtreck *et al.*, 2008; Olbrich *et al.*, 2012). Together, these results demonstrate the mechanisms that confer rotary beat pattern to the nodal cilia remain an unresolved question.

Another challenging problem is how rotational movement of the cilia could be linked to directional flow.

1.3.4.3. Fluid hydrodynamics

To understand the role of beating in producing fluid flow it is important to first have a look on how does fluid behave at microscales in a confined compartment such as the KV.

Fluid dynamics are ruled by laws that are complex at this microscale and the resulting fluid flow exhibits properties that are not obvious when used to human scale (Supatto and Vermot, 2011).

In fluid mechanics, the *Reynolds* number (Re) is a dimensionless number that defines the nature of a fluid flow and the relative contribution of inertia and viscous dissipation. The cilia-driven flow involved in zebrafish development shows characteristic scales, $L < 100\mu\text{m}$ and $U < 100 \mu\text{m s}^{-1}$ (L = length; U = typical velocity) (Supatto and Vermot, 2011). Using the kinetic viscosity of water ($\nu \approx 106 \mu\text{m}^2 \text{s}^{-1}$), the resulting Re is $< 10^{-2}$. The flow produced by beating cilia is described by a low Re ($\text{Re} \ll 1$) environment, and it is governed by *Stokes* equations - being referred as 'Stokes flow' (Smith *et al.*, 2012).

From a modeling point of view, the low value of the Re enables the simplification of the *Navier–Stokes* flow equation, the general model governing fluid dynamics (Supatto and Vermot 2011). If $\text{Re} \ll 1$, the inertial forces can be neglected compared to the viscous forces and the unresolved *Navier–Stokes* flow equation can be approximated by the linear Stokes flow equation (Figure 1.17). This equation points out the beginning of any modeling of cilia-driven flows (Cartwright *et al.*, 2006; Smith *et al.*, 2008; Smith *et al.*, 2010; Smith *et al.*, 2012). Thus, the flow generated by a group of cilia can be approximated as the sum of the flow induced by each single cilium. In addition, the linearity

and the time reversibility of ‘Stokes flow’ equation presents fundamental properties of the flow that can be generated by motile cilia (Supatto and Vermot, 2011).

1.3.4.4. Directional flow

Most cilia and flagella generate flow by an unidirectional power stroke, which is planar or almost planar, and in the direction of the flow (planar beating), while nodal cilia rotate in 3D.

Based on ‘Stokes flow’ equation, the first obstacle to the generation of a directional flow is the difficulty to achieve a net flow (Supatto and Vermot, 2011). The absence of inertia results in a velocity that is proportional to the force applied to the fluid (Supatto and Vermot, 2011; Smith *et al.*, 2012). This means that a specific mechanism is required to produce a directional fluid flow from the rotating cilia because the simple circling movement of the nodal cilia would only produce a vortex instead of biased flow (Buceta *et al.*, 2005). According to previous studies (Cartwright *et al.*, 2009; Smith *et al.*, 2012), in order to produce a directional flow at low Re, a beating cilium needs an asymmetry either in space or shape.

Most likely due to the cilia ultrastructure, length, and/or orientation, three types of spatially asymmetric cilia beating patterns have been proposed theoretically and observed experimentally in different organs of developing embryos: the ‘corkscrew-like motion’ (Kramer-Zucker, 2005), the ‘asymmetric bending’ (Schweicbert *et al.*, 2007), and the ‘tilted conical’ motion (Okada *et al.*, 2005), represented in Figure 1.13. From these three the ‘tilted conical’ motion was observed experimentally in mouse, rabbit, and fish L-R organizer. This specific type of cilia beating pattern is characterized by having a directional flow generated by cilia that exhibits a symmetrical circular motion without asymmetric shape as in the two previous cases.

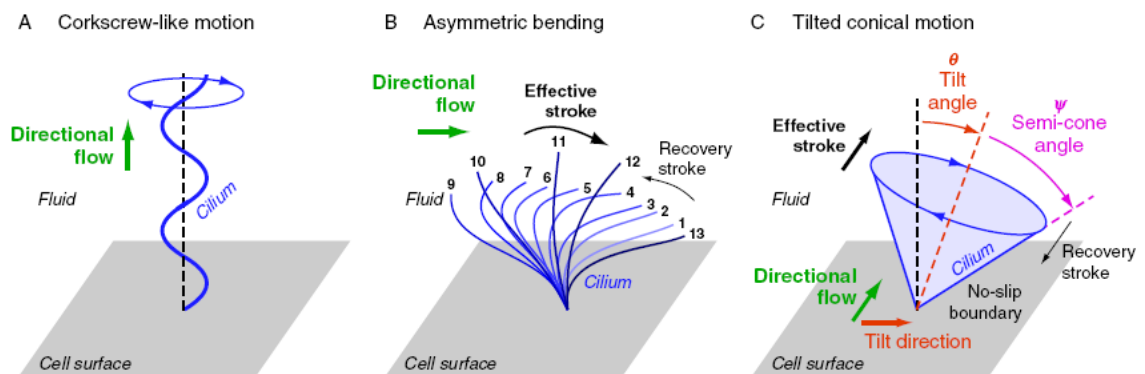


Figure 1.13 - Pumping flow with motile cilia at low Reynolds numbers. Three types of spatially asymmetric beating patterns observed experimentally: (A) helical motion or corkscrew-like motion which pumps fluids along the cilium, (B) asymmetric motion which is related to an asymmetric bending of the cilium during its movement, (C) cylindrical rotation with a tilted cilium. In (B) and (C), the effective stroke corresponds to the cilium momentum where fluid is moved efficiently in the direction of motion, whereas poor transport occurs during the cilia recovery phase (Supatto & Vermot, 2011).

In this case, theoretical fluid dynamics simulations of nodal cilia rotation could foretell that a linear directional flow will result if the rotational axes of the cilia are tilted (Cartwright *et al.*, 2009).

Here, the cilium interaction with the cell surface plays a critical role (Cartwright *et al.*, 2006; Smith *et al.*, 2008; Smith *et al.*, 2010; Smith *et al.*, 2012;): such a tilt will make sure that the effective stroke (towards the left side) will be much more efficient than the recovery stroke (towards the right side), because the latter will need to move fluid much closer to the cell surface, where viscosity is higher (no-slip boundary condition). Thus, the direction of the net flow generated depends on the cilium tilt and on the cell surface, and must be perpendicular to the direction of the cilium tilt and parallel to the surface.

Experimental authenticity of this prediction initially came from a analysis of the dynamics of ciliary beat. Using high-speed videomicroscopy, two different groups found that the rotational axes of the mouse nodal cilia are indeed tilted towards the posterior (Nonaka *et al.*, 2005; Okada *et al.*, 2005) promoting a directional flow toward the left direction with cilia rotating clockwise. It was also observed that the surface of the nodal cells was conspicuously convex, and that the position of basal body, the structure to which cilia are anchored at the cell surface, switched to the posterior side from an initial central location. Even more remarkably, Nonaka *et al.* (2005) demonstrated that motorized 'artificial cilia' could indeed drive a net leftward flow of viscous liquid silicone when their rotational axes were posteriorly tilted.

On the other hand in zebrafish it is noted that the beating pattern of KV cilia is different (counterclockwise motion) from the mouse nodal cilia, which presumably is because of different ultrastructures. This implies the counterclockwise fluid flow circulating around the dorsal-ventral axis within the KV cannot be due to a posterior tilt, but due to a dorsal tilt (Supatto and Vermot, 2011). In fact this has been already observed *in vivo* in previous studies. Kreiling *et al.* (2007) showed that cilia are concentrated in the dorsal-anterior region of the vesicle and that those cilia tilt is towards the already-established posterior and dorsal axes. This, thus, allows the viscous interaction of fluid with the cell surface to produce the continuous counterclockwise flow (Smith *et al.*, 2012; Supatto and Vermot, 2011).

In recent years, several models and simulations have been developed based on mouse node experimental data. In these theoretical studies, the cilium is modeled either as an microscopic sphere rotating in its place (Cartwright *et al.*, 2006), a small sphere moving on a fixed trajectory in the surrounding area of a planar surface (Vilfan *et al.*, 2012) or a slender body (Smith *et al.*, 2008). Whatever the complexity of the model used, they are a great advantage to understand how biological processes occur, by explaining new observations, raising specific predictions, and suggesting the next set of experiments.

Despite the fact that several features are common to mice and fish, each species remains different and might have developed diverse ways to break the embryonic symmetry using the same basic ciliary machinery (Supatto and Vermot 2011). Thus, it is crucial to improve the characterization of the L-R organizers, especially the differences between the different animal organisms, in order to establish more accurate L-R theoretical models.

1.4. Project goals

The main goal of this Master project was the characterization of the fluid flow dynamics in the Kupffer's vesicle (KV) of zebrafish embryos. It was our objective to understand how fluid flow dynamics could modulate the mechanisms responsible for the establishment of the left-right asymmetry.

To answer this question we decided to tackle the problem by using two different approaches: experimental characterization of the KV fluid flow in zebrafish embryos, and development of mathematical simulations for the KV flow in collaboration with David Smith group from Birmingham.

A tissue-specific screen previously done in *deltaD*^{-/-} mutants in our lab underpinned the beginning of my Master project. These mutants were previously reported by Lopes *et al.*, (2010) to present left-right defects and also KV fluid flow abnormalities. With this screen we found several differentially expressed genes in *deltaD*^{-/-} mutants, compared to wild-type embryos. Having identified some motile cilia-related genes, a validation study of gene expression was realized to 3 of these genes by a previous lab colleague. The validated genes were *dnah7*, *rsph3* and *foxj1a*. With this Master project we wanted to test if *deltaD*^{-/-} mutants had cilia defects and whether that could partially explain the defects in L-R patterning reported (Lopes *et al.* 2010). So considering what could be the best candidate responsible for the KV fluid flow problems seen in the mutants we decided to focus our analysis in the *dnah7* gene. Zhang *et al.* (2002) identified Dnah7 as an inner dynein arm component of human cilia important for its motility, and reported cilia from a PCD patient with mutations in Dnah7. Therefore we aimed to dissect the contribution of dynein Dnah7 deregulation to cilia defects and consequently in the KV fluid flow, by making use of the anti-sense technology of morpholinos in zebrafish embryos.

The first part of the project consisted in characterizing the fluid flow dynamics. Considering that we proposed to evaluate different parameters that inherently contribute to the fluid flow generation: cilia beat frequencies, by using high-speed videomicroscopy; and cilia lengths, through immunofluorescence assays. These measurements were conducted in three different genetic backgrounds: Wild-type (WT) and *deltaD*^{-/-} mutant embryos and *dnah7* morphants. After we studied the cilia-generated fluid flow inside the zebrafish KV by tracking native particles and calculating their velocity in a non-invasive assay. We intended to analyze different situations where the KV fluid flow was disrupted so we used the 3 different genetic backgrounds that allowed us to get a range of motile cilia inside the KV.

To have an insight of *dnah7* mRNA distribution throughout embryogenesis, we also evaluated the *dnah7* gene expression pattern throughout several stages of embryo development using whole-mount *in situ* hybridization (WISH).

The second part of this project consisted in characterizing several parameters needed to input into the mathematical model that was being developed: KV volumes and cilia numbers in live embryos, with the help of two lab colleagues, Barbara Tavares and Petra Pintado.

It was our ultimate goal, to test causality between KV fluid flow dynamics with organ laterality, which we assessed by following the development of each embryo analyzed.

CHAPTER 2

Materials and Methods

2.1. Zebrafish mating

General maintenance, collection and staging of zebrafish were carried out at the IGC zebrafish facility (Oeiras, Portugal) as described by Westerfield, (2000).

Zebrafish fertilization and embryo isolation outlined the basic steps to get embryos for use under the zebrafish line needed for each experiment. Wild type (AB strain) and *deltaD*^{-/-} mutant embryos were staged according to Kimmel et al. (Kimmel *et al.*, 1995). The development stages are given in hour post-fertilization (hpf) and day post-fertilization (dpf) according to morphological criteria. For somite-stage embryos, the number of somites was used as a proxy of developmental time.

Adult male and female zebrafish selected from the main-tank system were put together in a top compartment of a mating-tank and stayed in the dark overnight (O/N). To ensure that male fish would not mate with the females during this period, fish of the opposite sex were separated by a divider. At the onset of the light cycle, zebrafish would normally initiate breeding behavior that results in the laying and fertilization of eggs (Westerfield, 2000). So in the beginning of the fish light cycle the dividers were removed allowing the mating process. The females laid eggs, which were externally fertilized by the males, and fell to the lower compartment of the tank through a sieve, preventing the egg cannibalism by the parents. Afterwards the adult fish were moved back to their home tank and the collected eggs were sorted into a Petri dish with embryo medium (5 mM NaCl, 0,2 mM KCL, 0,3 mM CaCl₂, 0,3 mM MgSO₄, ddH₂O – pH 7,2). These eggs stayed in temperature-controlled (28°C) incubators until the embryos reached the desired stage. May be say here that in order to perform imaging at 8-10 somite-stages in the next morning the incubation temperature was optimized to 25°C.

2.2. Recording of cilia beat frequencies in the Kupffer's Vesicle

The use of light microscopy coupled with high-speed imaging in cilia beat frequency studies yields useful data that allows to identify altered ciliary beat patterns that may be related to specific ultrastructural defects. To characterize cilia motility in the L-R organizer of WT and zebrafish mutants, we analyzed the CBF of several individual cilium by filming live embryos with high-speed videomicroscopy.

2.2.1. Mounting zebrafish live embryos for KV imaging

KV imaging needed a special and careful mounting set up as the young embryos are easily damaged. Since we used an inverted compound microscope, the zebrafish embryos had to be mounted with the dorsal roof of the KV facing the objective lens – defined as “dorsal view”. For this purpose we made customized 2% agarose 18 well moulds to be placed in glass-bottom Petri dishes

(FluoroDish™, WPI Inc, China). This design allowed to mount and maintain live embryos still with the KV dorsal roof facing the bottom of the mould.

At room temperature, live embryos between 6-7th somite-stages were gently dechorionated with sharpened forceps and placed in the agarose mould filled with embryo medium to keep the embryos moist. With the help of a microloader pipette tip, embryos were placed correctly inside the mold wells with the dorsal roof of the KV facing down.

2.2.3. Microscope setup

Mounted embryos at 8-10th somite-stages were set under the 100x/1.30NA oil immersion objective lens on a Nikon Eclipse Ti-U inverted brightfield light microscope at room temperature. After finding and focusing the KV, images were recorded with a high speed FASTCAM MC2 camera (Photron Europe, Limited) and controlled with PFV (Photron FASTCAM Viewer) software.

2.2.4. Recording KV cilia – image acquisition

Kupffer's vesicle was scanned through the different focal planes along the dorsal-ventral axis in order to observe as many cilia as possible. Since this spherical organ has cilia projecting from all the cells lining the fluid filled space (Okabe *et al.*, 2008), these can be visible from multiple different orientations. Once a region of interest inside the KV was chosen, focused cilia were recorded and its anterior-posterior and left-right position was annotated, allowing to map each cilium inside the KV.

The recorded videos were produced by the collection of consecutive images known as frames, taken at a properly selected rate expressed in frames per second (fps), for a finite time period. Accurate measurements of cilia beat frequencies were dependent on the frame rate at which images were acquired. The *Nyquist-Shannon* sampling theorem implies that to measure the frequency F_0 of cilia, image acquisition should be performed at a rate more than twice as fast (Jaffe *et al.*, 2010), which is a necessary condition to avoid aliasing (motion artifacts). Therefore acquisitions at even faster rate are highly recommended (typically, $F > 3-4 * F_0$). This higher acquisition rate compensates for the fact that cilia motion may not be exactly periodic (sinusoidal/harmonic) as for the finite duration of the movie sampling, overall facilitating the frequency measurement. Previous groups have reported that cilia beat frequencies in the KV range from 5 to 45 Hz (reviewed in Freund *et al.*, 2012), so according to Jaffe *et al.*, (2012) a frame rate above 180 fps is advised. Since our imaging camera recorded up to 2000 fps at its full image resolution (512 x 512 pixels) we decided to choose a 500 fps frame rate which corresponds approximately to eleven times faster than the highest fundamental frequency reported and it is currently used to diagnose PCD patients (Shoemark *et al.*, 2013). This allowed us to efficiently analyze and characterize the components of the ciliary movement as we were able to produce high quality images.

Each movie was produced by a total number of 1000 frames which corresponds to a 2 second movie at a 500 fps frame rate. To validate that 2 second movie was a significant time window to correctly characterize the cilia beating pattern during the 8-10th somite stages we decided to do a live time course imaging with an embryo during these developing stages. A focal plane of the KV was chosen from one zebrafish embryo at 8th somite stage and the cilia focused on this focal plane were recorded every 10 minutes during 1 hour at room temperature (approximate time to reach 10 somites) with the same experimental setup described before. The six movies collected during the time course showed that during the 8-10th somite stages cilia had a consistent cilia beat pattern (see Figure S1 in Annex II).

In summary, for this project the KV cilia were recorded during 2 seconds at a 500 fps rate. This experimental procedure allowed us to measure 5 to 45 Hz CBF, which is the frequency range previously reported, providing novel information on zebrafish KV cilia motility.

2.2.5. Image processing and kymograph design

Ciliary movement was recorded for each pixel within the image resolution, resulting in a set of temporal waveforms with as many members as there were pixels. Each waveform depicted the pixel intensity as a function of time, displaying the periodicities of the ciliary movement (Olm *et al.* 2011) in a graph called kymograph (Figure 2.2).

CBF analysis had to follow a previous movie image filtering procedure using ImageJ program (<http://imagej.nih.gov/ij/>) to extract the resulting kymographs, before passing by the Fourier analysis in R software (R Development Core Team, 2010). The ImageJ protocol consisted in removing the background noise of the movie frames that otherwise would interfere with the CBF analysis and then produce a kymograph depicting each cilia beating pattern. The main steps of the protocol were as follows: a) static objects were removed by creating an average intensity projection of the 1000 frames that is subtracted to each frame of the original movie – as a result, the motile objects (such as cilia) are enhanced, getting lighter and the static objects getting darker (Figure 2.1); b) movie image stacks were represented as orthogonal views, also called kymographs, showing the spatial position over time (x,t and y,t); after choosing the cilium of interest, a point is selected where the tip of the cilium passes during its trajectory, which produces a pattern of the cilia movement; c) a straight line was drawn over the time domain of the entire (x,t or y,t) kymograph and a plot profile is generated (Figure 2.2), which gives the graphical representation of pixel intensity over time; d) a list of values correspondent to the plot profile was recorded, which was exported to R software to perform Fourier analysis with the Fast Fourier Transform (FFT) algorithm.



Figure 2.1 - Snapshot image of a KV beating cilium in a live embryo – cilia image after background subtraction and image improved contrast for posterior kymograph analysis.

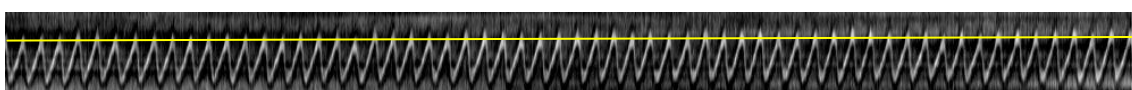


Figure 2.2 - Kymograph showing a cilium beating pattern – orthogonal view of a cilium beating at a single fundamental frequency, during a time of 2 seconds (1000 frames).

2.2.6. CBF spectral analysis

Ciliary movement was recorded for each pixel within the drawn line in the kymograph, resulting in a set of temporal waveforms which reflected the cilium beat pattern. The aim of the spectral analysis was to estimate, based on this set of waveforms, the proportion of each CBF value in relation to the overall movement of the cilia within the drawn line, accomplished through Fourier analysis.

As described previously, a list of plot values was obtained from the resultant waveform of each cilium kymograph, and was imported to R program. In collaboration with Dr. Adán Guerrero (Instituto Gulbenkian da Ciência) we developed a script for R program, which applies the FFT algorithm to KV cilia data (“FFT script function” in Annex).

The FFT script function resolves a time waveform (signal) into its sinusoidal components, meaning that this function takes the time-domain data, which is represented by the list of values obtained previously, and returns the Fourier spectrum of the data. This spectrum interprets the ciliary movement by describing how the power of the signal is distributed with frequency.

Thus, we could characterize each KV cilium motility by the number of the existent frequencies, depicted as power peaks in the Fourier spectrum (Figure 2.3).

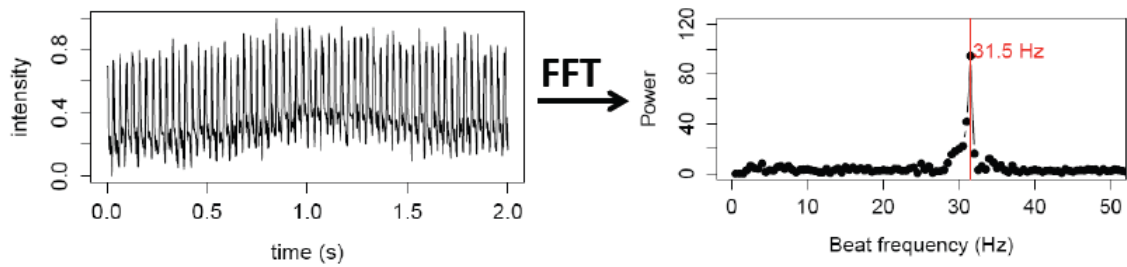


Figure 2.3 – Characterization of KV cilium motility - Time series over 2 seconds for the same beating cilium, and the resulting power spectrum after analysis using Fast Fourier Transform (FFT) for the same cilium showing that it has only one fundamental frequency of 31.5 Hz.

Significant cilia beat frequencies were selected from their Fourier spectra based on local maxima criteria using a frequency window of 4Hz. Only local maxima that were beyond 2Hz and above a 13 power limit were considered in order to remove the influence of any signal noise. These parameters made the algorithm very robust, allowing a confident spectral analysis.

2.2.7. Kupffer’s vesicle fluid flow velocity measurements

For all the genetic backgrounds we measured the KV fluid flow by a non-invasive method described as in Lopes *et al.* (2010). This method consists in tracking naturally occurring particles that move with the fluid flow.

Differently to the protocol described for cilia imaging here we used a frame rate of 60 fps in a 2000 frames time window (~33 seconds). Particle movement was recorded after selecting several focal planes of the entire KV where one or more particles were observed.

The main difference in this methodology to that used in Lopes *et al.* (2010) occurred in the posterior movie analysis. In ImageJ program all the videos analyzed were initially rotated in a way that the anterior region of each KV was oriented upwards. Afterwards, we used the ImageJ plugin MTrackJ to follow each individual particle (<http://www.imagescience.org/meijering/software/mtrackj/>) in a 0.2 second interval allowing to measure instant velocity of the particle movement.

Particles were tracked manually and the ImageJ plugin returned a list of coordinates for each track point (x and y) and a list of distances between two consecutive point tracks. These data were imported to an Excel datasheet and particle velocity was calculated.

Using R program we then analyzed the collected information by different ways. According with the central point of the each KV analyzed we generated rose diagrams to illustrate the relative distribution of all tracked particles inside the KVs. For assessing visually the speed of the fluid flow, representations of the KV flow were produced for each embryo, which we called ‘flow maps’. By projecting in a single image the entire particle trajectory during the movie duration and attributing to

each second a different color ('Macro' function in Annex), being red the color used to identify the first second of the movie.

The quantification of such flow speed was achieved by created boxplots that represented the different flow speed contributions in each region of the KV, and heat maps that visually showed local flow speed ('Boxplot script function' in Annex).

This procedure was then used to analyze the entire data correspondent to WT, *deltaD*^{-/-} and *dnah7* morphants embryos and provide an overall view of the fluid flow dynamics for each genetic background.

It is important to refer that our experimental observations and mathematical calculations were performed in the midplane of the KV. The microscope setup allowed us to track particles in a depth of field below 1µm. Elementary mathematical analysis shows that if the z-component V_z is small, it makes a contribution to the velocity magnitude which is very well approximated by $-(1/2)*(V_z^2/\sqrt{V_x^2+V_y^2})$. Essentially a small component V_z changes the velocity magnitude by a very small amount, which allows us to say that our speed measurements are correct and present a negligible error.

Moreover, each filmed embryo was transferred to a 12 well test plate (TPP Techno Plastic Products AG, Switzerland) in embryo medium and incubated at 28°C for later individual heart and gut scoring.

2.3. In silico experiments - Mathematical modeling

In order to better understand the flow fields involved we mathematically modeled KV fluid flow. In collaboration with Drs. Andrew Smith, Thomas Montenegro-Johnson and David Smith, we computed the most realist mathematical model of the KV using experimental data previously collected for KV volume, CBF, cilia number and cilia length.

To interpret the effect of cilium number and distribution on the flow generated within KV, we used a modified version of the computational model of Smith and Johnson *et al.* (Smith *et al.*, 2012) described in detail in the Annex II section. These modifications allowed for arbitrary placement of cilia, multiple beat frequencies and variable lengths. Cilia were modeled as whirling rods, with diameter 0.3 µm, programmed to perform a conical rotational motion with dorsal roof and ventral floor cilia tilted posteriorly and 'equatorial' cilia tilted dorsally.

The average dimensions of KV were ascertained from confocal microscopy imaging of WT and *deltaD*^{-/-} mutants performed previously in the lab; for each simulation, KV was modeled as a scalene ellipsoid with axes 59 µm (L-R), 52 µm (A-P) and 49 µm (D-V) for WT and 57 µm (L-R), 56 µm (A-P) and 43 µm (D-V) for *deltaD*^{-/-}. Following Kreiling *et al.* (Kreiling *et al.*, 2007), KV was divided into

4 regions: the dorsal-anterior (D-A), dorsal-central (D-C), dorsal-posterior (D-P) and ventral (V) sectors. Cilia were assigned random positions in each sector, so that approximately 38%, 25%, 17% and 20% of cilia were located in the D-A, D-C, D-P, and V sectors respectively, matching both our own data and that of Kreiling et al. (Kreiling *et al.*, 2007).

Each simulation was carried out by sampling cilia lengths and frequencies from statistical distributions parameterized by our experimental data (see Figures 3.1, 3.2, 3.3, 3.19, 3.20 and 3.21 in Results Chapter), using the probability distributions. Wobbling cilia with two frequency peaks were incorporated as described in the Annex II. For WT, approximately 14.4% of the cilia were randomly designated wobbling, and 22% immotile (approximated by the nearest whole number), with 11.3% wobbling and 15% immotile for *deltaD*^{-/-}.

The computational meshes for each embryo were generated in the same manner as in Smith and Johnson *et al.* (Smith *et al.*, 2012) with the addition of these randomly sampled parameters. The flow generated within each model embryo was then calculated using the boundary element regularized Stokeslet method in which our collaborators have specialized (in Annex II).

For *deltaD*^{-/-}, 5 independent simulations with different random parameters were performed for embryos with 15, 22, 29 and 36 cilia. For WT, 5 simulations were performed for embryos with 25, 37, 45 and 60 cilia. These values were chosen to span the range of cilia numbers found experimentally (see Figure 3.20 in Results Chapter). Analysis of simulations focused on the Coronal plane time-averaged velocity field. Computations were coded in Intel Fortran 90 with the NAG Fortran library Restarted GMRES (Numerical Algorithms Group, Oxford, UK); mesh generation and plotting were carried out using Matlab (Mathworks Inc., Natick, MA, USA). This part of the work was done by our collaborators.

2.4. Molecular study of the motility gene *dnah7*

In order to understand the molecular players responsible for the motility defects present in *deltaD*^{-/-} mutants (Lopes et al. 2010), our lab performed a tissue specific screen using microarrays revealing that some motility genes (*dnah7*, *rsph3* and *foxj1a*) were deregulated. Among these, *dnah7* which codifies for a heavy chain axonemal dynein located at the inner dynein arms of ciliary axonemes, was selected for motility studies. Gene expression for this *dnah7* in the KV was previously performed and confirmed in our laboratory.

2.4.1. Morpholino antisense oligonucleotides knockdown

A widely used anti-sense knockdown tool in the zebrafish community is the morpholino oligonucleotide technology (MOs). This technique is normally employed as oligomers of 25 morpholino bases that are targeted via complementary base pairing to the mRNA of interest. In this way, MOs can

knock down gene expression, modify RNA splicing or inhibit miRNA activity and maturation (Bill *et al.*, 2009).

For *in vivo* functional characterization of *dnah7* activity, a translation blocking MO (sequence: AGGGTCATCTTCACGGTGCATAATA) specific to this gene (Ensembl: ENSDARG00000060165) was microinjected to zebrafish transgenic embryos AB *tg(sox17:GFP)^{s870}* (Chung and Stainer, 2008) and *deltaD^{-/-}* mutants *tg(sox17:GFP)^{s870}* for later gut laterality screening. As recommended by Eisen and Smith (Eisen and Smith, 2008) we used a five-mismatch morpholino (sequence: AGGCTGATCTTGACGCTGGATAATA) as a negative control. Morpholinos were specifically designed and supplied by Gene Tools LLC (Philomath, OR; <http://www.gene-tools.com/>).

Zebrafish mating occurred as described in the section 2.1 and the microinjection procedure followed a protocol previously described (Rosen *et al.*, 2009). Initially, the capillary needles were back-loaded with the MO solution using a Microloader tip (Eppendorf, Hamburg, Germany), and inserted with a silicon gasket into a three-axis micromanipulator (Narshige, Greenvale, NY). A PV820 Pneumatic PicoPump pressure injector (World Precision Instruments, Inc., Sarasota, FL) was used to reproducibly inject equal amount of the solution into the embryos. To calibrate and calculate the volume of solution injected, a S1 stage micrometer (10mm/0.1mm Graticule Ltd., Tonbridge, Kent, UK) was used and the injected time of the micro-injector was adjusted so that 1.4 nL of solution was delivered with each pulse. For our experiments, zebrafish eggs were collected immediately after being laid and injected at one-cell-stage.

Morpholinos stocks were reconstituted at 1 mM concentration in Milli-Q (MQ) water. The first step in using the MOs was to determine the optimum delivery dose. To resolve the MO tolerance by the embryos, determine the correct amount of MO to deliver and optimize the phenotype to toxicity ratio, WT zebrafish eggs were initially injected at four different doses: 12 ng, 6 ng, 3 ng and 2.6 ng, per injected volume; then embryo development was followed.

2.5. Generating transparent zebrafish

Zebrafish pigmentation is initiated during embryogenesis, after 23 hpf, and begins in the retinal pigmented epithelium and in the head melanophores. The pigment cells develop rapidly, and within hours they constitute a prominent feature of the embryo that can interfere with some observations. In order to improve signal detection by whole mount *in situ* hybridization, confocal microscopy, or expression of GFP, embryos were treated with 1-phenyl 2-thiourea (PTU, Sigma) at approximately 24 hpf (0.1 mM in embryo medium) according with a previously described protocol (Karlsson *et al.*, 2001). PTU inhibits melanogenesis by blocking all tyrosinase-dependent steps in the melanin pathway which allows embryos to remain transparent as long as the PTU treatment is continued.

2.5.1. Zebrafish heart and gut laterality screening

To explore the biological significance of fluid flow, we kept the embryos alive after imaging the movement of KV native particles in four genetic backgrounds: WT, *deltaD*^{-/-} mutants, embryos injected with *dnah7* morpholino (MO) and embryos injected with the respective five-mismatch control-MO. After 30 hours post fertilization (hpf) we evaluated heart jogging using a stereoscopic Zoom Microscope (SMZ745, Nikon Corporation, Japan) to observe the embryos from the ventral side. The heart is readily visible at 30 hpf beating under the left eye. At 72 hpf, we assessed gut laterality by observing live larvae from the transgenic lines AB *tg(sox17:GFP)*^{s870}; and *deltaD*^{-/-} *tg(sox17:GFP)*^{s870} that have GFP in the developing gut. For gut visualization larvae were observed from the dorsal side using a SteREO Discovery V8 stereomicroscope (Carl Zeiss Microimaging GmbH, Jena, Germany) using a GFP filter.

Images were taken with a SteREO Discovery V8 equipped with a CCD camera AxioCam HRc (Carl Zeiss Microimaging GmbH, Jena, Germany) using LM Image Manager (Leica Microsystems) or AxioVision 4.5 software (Carl Zeiss).

2.6. Imaging KV cilia by immunostaining

Immunofluorescence (IF) localization of cellular molecules exploits the ability of antibodies to bind specific antigens (usually proteins) with high affinity. The technique may be used to localize antigens to subcellular compartments. In our experiments, this technique was performed for the purpose of visualizing KV cilia using a monoclonal antibody specific for an acetylated form of α -tubulin that recognizes the antigen along the cilia structure.

The IF procedure was followed according to previous methods (Jaffe *et al.*, 2010). Initially, embryos at 8-10th somite stages previously injected with *dnah7* MO were fixed in 4% paraformaldehyde (PFA) O/N at 4°C. Next, embryos were dechorionated in phosphate buffered saline (PBS) solution followed by permeabilization in PBSX (250 μ l Triton X-100 10% in 50ml of PBS) for 2 times 5 minutes each. For the acetylated α -tubulin antibody, extra fixation was performed with acetone for 7 minutes at -20°C. Samples were then blocked with PBDX (0.5g bovine serum albumin/0.5ml dimethyl sulfoxide/0.25 ml Triton X-100 10% in 50 ml of PBS) with 15 μ l goat serum per ml for 1 hour at room temperature. After washing in PBDX, embryos were incubated with 1:400 acetylated α -tubulin monoclonal antibody (Sigma) O/N at 4°C. Next day, primary antibody was removed as much as possible through several PBDX washings and embryos were then incubated with 1:500 secondary antibody Alexa Fluo 488 (Invitrogen) with 15 μ l goat serum per ml O/N at 4°C. After washing excess of secondary antibody in PBS, embryos were re-fixed for 5 minutes in PFA 4% and washed again in PBS. Finally, before imaging the KV, each embryo was dissected with sharp forceps and flat-mounted between two-cover slips, dorsal side up.

KV cilia images were taken in a Zeiss LSM-710 confocal microscope with a 40x/1.20 NA water immersion objective. Through acquisition of dorsal projections of confocal z-stacks (0.25 μm step size) we did the reconstruction of the whole KV allowing the visualization of all the cilia inside.

2.7. Cilia length measurements

Ciliary length was measured in 2D from two different sources: high-speed live imaging and immunofluorescence cilia images, with NIH Image J software. Considering that cilia inside the KV are visible from multiple different angles, only those recorded in an angle parallel to the focal plane were measurable.

3D measurements were extracted by filming the whole KV in 3D using live embryos injected with *arl13b-GFP* mRNA, done by a colleague Barbara Tavares in the lab. Immotile cilia were scored by filming the entire volume of the KV of live embryos injected with *arl13b-GFP* mRNA by confocal microscopy. Motile cilia were identified as bright GFP⁺ objects with 'cone-like' shapes, created by their circular rotation (which is much faster than the normal acquisition rates achieved by confocal imaging), whereas immotile cilia appeared as sharp GFP⁺ line segments.

2.8. Cilia localization inside the Kupffer's vesicle

All cilia filmed for cilia beat frequency (CBF) studies were localized inside the Kupffer's vesicle, according to the left-right (L-R) and anterior-posterior (A-P) regions.

Since immotile cilia (without CBF) were less visible by brightfield high-speed videomicroscopy another set of data was used for this analysis. Cilia previously recorded in the lab by Barbara Tavares through live imaging fluorescence confocal allowed was to detect all the immotile cilia inside the KV.

In this way we were able to localize cilia and correlate the localization with a specific CBF pattern after CBF spectral analyses.

2.9. Kupffer's vesicle volume measurements

KV volume was calculated using the dimensions measured for WT and *deltaD*^{-/-} mutants, assuming that the geometric three-dimensional shape of a KV resembles to an ellipsoid. So, by filming live embryos that were transgenic for *sox17:GFP*, thus having the KV cells expressing GFP, we measured the ventral/dorsal (a), anterior/posterior (b) and left/right (c) axes of each KV. After, we

calculated the volume of the KVs both for WT and *deltaD*^{-/-} mutants by the given formula for an ellipsoid = $\frac{4}{3}\pi abc$.

2.10. Whole-mount in situ hybridization

The *in situ* hybridization (ISH) allows sites of expression of specific genes to be detected in morphologically preserved cells or embryos, using labeled segments of RNA that bind to complementary sequences. This technique is used to obtain valuable temporal and spatial information about a specific gene expression within the tissue (Thisse and Thisse, 2008) however variable probe specificity and tissue penetration makes it unsuited for quantification.

We performed whole-mount in situ hybridization (WISH) experiments to study the localization of *dnah7* gene expression in zebrafish WT embryos through different development stages. The RNA-probes used have been developed and tested previously in the lab.

The WISH procedure was performed as in (Thisse and Thisse, 2008) on O/N 4% PFA fixed embryos followed by 3 hours 100% Methanol (MeOH) at -20°C fixed zebrafish embryos at distinct developmental stages (see embryo stage used in Table 2.1). The *dnah7* anti-sense and *ntl* RNA probes were already available in the lab. Embryos were first brought through 75%, 50% and 25% MeOH-PBS for 5 min each at RT and then twice for 5 min in PBT (PBS/Tween20 0.1%) for rehydration. Embryos were dechorionated prior to proteinase treatment. This treatment consisted in the embryo's digestion with Proteinase K (5mg/ml in PBT) at RT for different periods of time according to their developmental time (recommended time for embryos in early somitogenesis is 1 minute). Immediately after, embryos were fixed in 4% PFA for 20 min, followed by a series of washes in PBT.

The pre-hybridization and hybridization steps were conducted at 65°C for both ribo-probes in HYB-mix solution (Formamide (Roche), 20x SSC, Tween20 10%, 1M Citric acid to pH6 and heparine (0.63mg/ml)). The probes were added to the embryos and incubated O/N (see RNA-probes dilutions in Table 2.1).

In the second day, the probes were recovered and embryos were brought through 100%, 75%, 50% and 25% HYB-mix/2x SSC for 15 min each at 65°C and then once for 15 min in 2x SSC at 65°C. Next, embryos were washed twice in 0.2 SSC for 30 min and then through 75%, 50% and 25% 0.2 SSC/PBT for 10 min each at RT, finishing with a RT wash in PBT for 10 min. Embryos were blocked for at least 2 hours at RT with BSA, goat serum (GS) and PBT (50mL PBT with 100mg BSA and 1ml GS). *In situ* hybridization signals were detected with sheep anti-digoxigenin-AP Fab fragments (Roche Mannheim, Germany), and incubated at a 1:5000 dilution in blocking solution, O/N at 4°C.

In the next day antibody solution was removed and embryos were washed in PBT in a 6-times series of 15 min. After embryos were equilibrated in staining buffer (1M TRIS pH9.5, 1M MgCl, 5M

NaCl and Tween20 10%) 3 times for 5 min each at room temperature. The color staining was carried out with NBT/BCIP (Roche Mannheim, Germany), alkaline phosphatase substrates, until the probes reached the desired level of purple staining in relation to background noise. In order to stop the staining reactions we used 4% PFA for 20 min at RT, followed by several washes in PBS prior to mounting embryos in 100% glycerol for photography.

WISH results were photographed with an AxioCam MRc 5 camera using an upright microscope (Axiovert 40 CFL) and images were treated with AxioVision 4.5 software (Carl Zeiss).

Table 2.1 - WISH experiment. List of mRNA probes, dilution factors and embryo-stages used.

mRNA probes	Dilution factor	Embryo-stage used
<i>dnah7</i>	5:200	bud stage (10 hpf), 8-10 somites stage (~12 hpf), 16 hpf, 24 hpf and 48 hpf
<i>ntl</i>	0.5:100	16 hpf

2.11. Statistical analyses

All statistical tests were performed using R software (R Development Core Team, 2010) – codes described in Annex – at a significance level at 95%.

KV fluid flow velocity measurements are presented for a number of particle tracks (WT = 847; *deltaD*^{-/-} = 10193; *dnah7* knockdown = 3470; *dnah7* mismatch control-MO = 1700) that were generated from different embryos (WT = 7; *deltaD*^{-/-} mutant = 26; *dnah7* knockdown = 8; *dnah7* mismatch control-MO = 5). Rayleigh tests of circular distribution of the relative particle positioning with respect to the centre of the KV were performed for assessing the significance of finding particles moving preferentially in the anterior/posterior and left /right regions. Potential differences in KV fluid flow speed between WT and each genetic mutant, and differences between each KV halves (anterior-posterior and left-right regions) within each genetic background were assessed using Wilcoxon test.

CBF data are presented for a number of individual cilia (WT = 80 cilia; *deltaD*^{-/-} = 77; *dnah7* knockdown = 26) that were selected randomly from different embryos (WT = 16; *deltaD*^{-/-} = 26; *dnah7* knockdown = 15). Statistical significance of CBF deviations within each genetic background population

was assessed through a Wilcoxon test. CBF differences between the WT population and each of the genetic mutants separately was achieved with a Wilcoxon test.

For cilia without any type of beating frequency (immotile cilia), data previously analyzed in the lab by Barbara Tavares through fluorescent confocal live imaging was used, for a number of individual cilia (WT = 300; ΔdeltaD = 240) selected from a random set of embryos (WT = 7; ΔdeltaD = 8). Potential biased spatial distribution in the left-right regions of the KV, for each CBF type was assessed by binomial test. Deviations from previously reported (Kreiling *et al.*, 2007) cilia distribution in anterior, central and posterior regions, were achieved by Fisher test.

A different set of data was used for assessing cilia 2D length differences between each genetic background. Cilia were measured from immunofluorescence 2D confocal images from WT (639 cilia; 27 embryos), ΔdeltaD (280 cilia; 17 embryos) and *dnah7* knockdown (172 cilia; 3 embryos) embryos. Cilia length differences between the WT population and each of the genetic mutants separately was assessed with a Student's t-test.

2D length measurements are presented for a number of cilia (WT = 73 cilia, 11 embryos; ΔdeltaD = 119 cilia, 15 embryos), which were previously recorded for CBF studies by high-speed videomicroscopy. Any potential correlation between CBF type and cilia length was determined by a Student's test.

Data used for volume calculations are obtained for a number of embryos (WT = 8; ΔdeltaD = 8). Volume differences between the two genetic backgrounds were assessed using a Student's test.

CHAPTER 3

Results

The results obtained by filming the Kupffer's vesicle (KV) of live embryos with high-speed videomicroscopy are reported here, including cilia beat frequency (CBF) studies, cilia length measurements and KV fluid-flow velocity measurements. These studies were conducted both in wild-type (WT), *deltaD*^{-/-} mutant and *dnah7* morphant embryos, which allowed us to obtain a range of motile cilia number in the KV. One important feature of this study was the fact that embryos after being filmed could be kept alive for later scoring of the heart and liver position.

Moreover, for better interpretation and support of the experimental results we matched them to mathematical simulations which mimicked the KV fluid flow in WT and *deltaD*^{-/-} mutant situations.

In addition, to complement the biophysical work with molecular studies we studied *dnah7* gene expression for different stages along the zebrafish embryo development by a time course whole-mount *in situ* hybridization (WISH) for WT embryos.

3.1. Cilia Beat Frequency studies

To identify the underlying frequencies of each individual cilium we performed a Fast Fourier Transform (FFT) spectral analysis on cilia data acquired by bright field high-speed videomicroscopy (as in movie S1 in Annex II).

3.1.1. CBF analysis in WT and *deltaD*^{-/-} embryos identifies three cilia populations

We show that, like the mouse node, the zebrafish KV is a ciliated structure. However the KV is a closed vesicle and has cilia all around with a cluster of monociliated cells preferentially localized in the anterior pole of the organ (Kreiling *et al.*, 2007).

Our results demonstrated that in the WT zebrafish Left-Right (L-R) organizer there are two major populations of motile cilia characterized by different CBFs (Wilcoxon test $p < 0.05$). One population beats at a single frequency (Figure 3.1) and a second novel population is characterized by additional lower frequency components (Figure 3.2). These novel cilia were readily identifiable by kymograph analysis and due to their irregular motility pattern (Figure 3.2c) we named them 'wobbling cilia'. In WT embryos, cilia that displayed one single CBF constitute 60% of the KV cilia population and show a unimodal distribution peaking at 33Hz (Figure 3.1a). Along a period of time of 1 hour (see Figure S1 annex II) this population of cilia displayed a constant CBF.

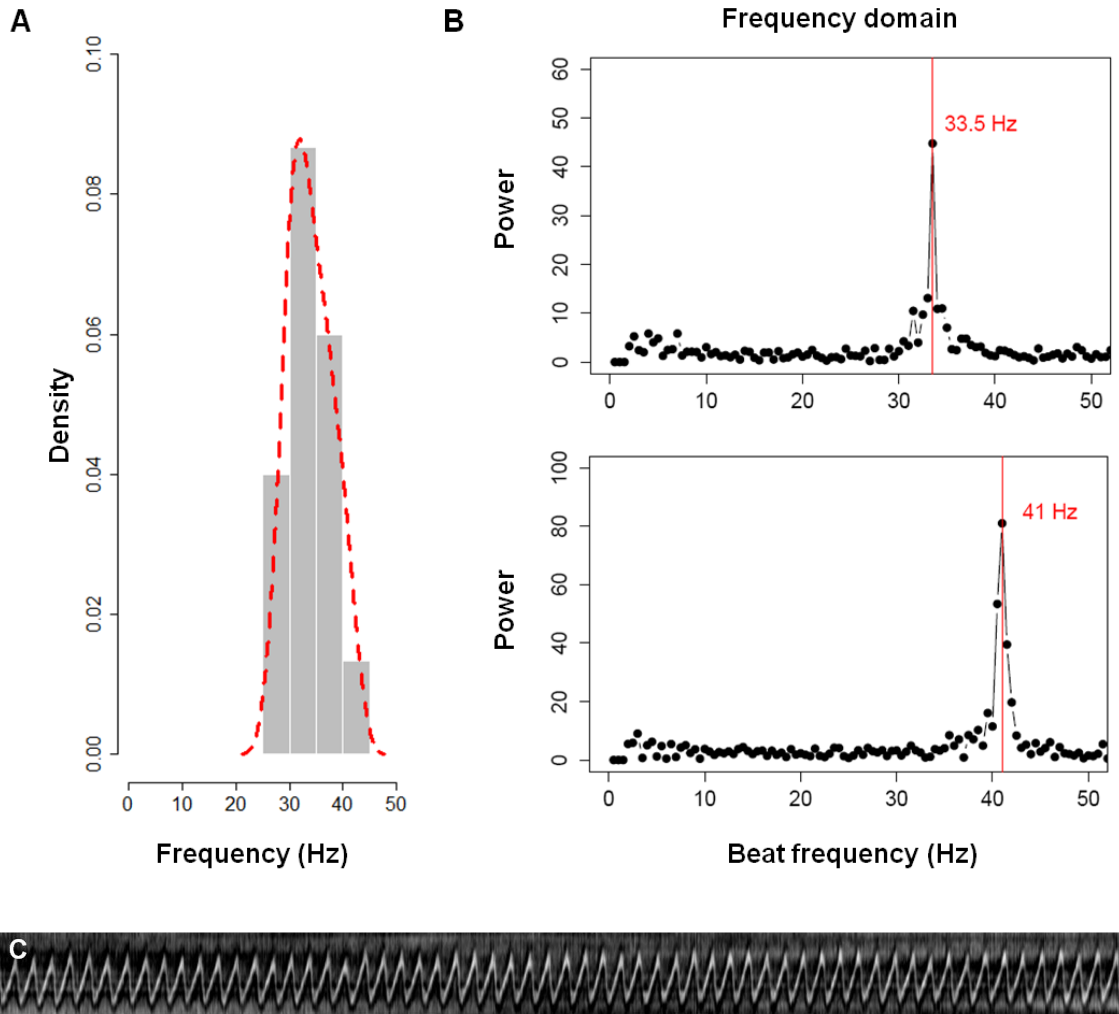


Figure 3.1 – WT cilia population with single CBFs. A - CBF frequency distribution of the cilia population that displays single CBFs; B - Representative results from two cilia with single CBF after FFT spectral analyses; C - Kymograph of a cilium presenting one fundamental frequency. CBF (cilium beat frequency).

The second population of motile cilia characterized by the wobbling motility, ranged from 3 to 45Hz, whereas the lowest frequency varied between 3 and 18Hz and highest frequency from 17 to 45Hz. Overall, these cilia accounted for 14% of the total population (Figure 3.5).

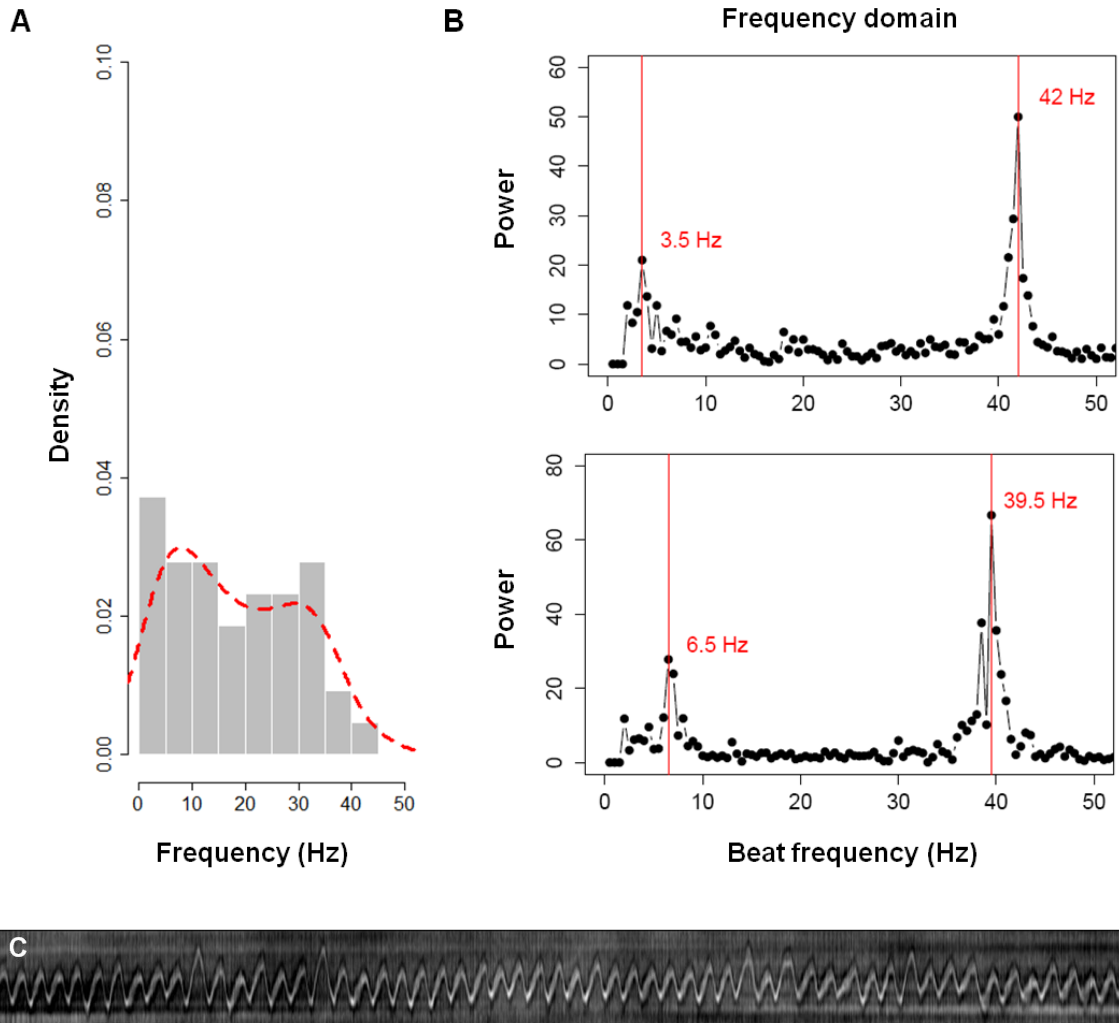


Figure 3.2 – WT cilia population with double CBFs. A- CBF frequency distribution of the cilia population that displays double CBFs; B - Representative results from two cilia with double CBF's after FFT spectral analyses; C - Kymograph of a cilium with two major frequencies which we called a wobbling cilium. CBF (cilia beat frequency).

We performed a similar CBF analysis with *deltaD*^{-/-} mutants, which showed that the two motile cilia populations were maintained in similar percentages in *deltaD*^{-/-} mutants (Wilcoxon test $p > 0.05$; Figure 3.3). These results revealed that even in the *deltaD*^{-/-} mutants, that tend to have shorter cilia lengths (see Figure 3.19), the percentage of wobbling cilia was maintained in the KV.

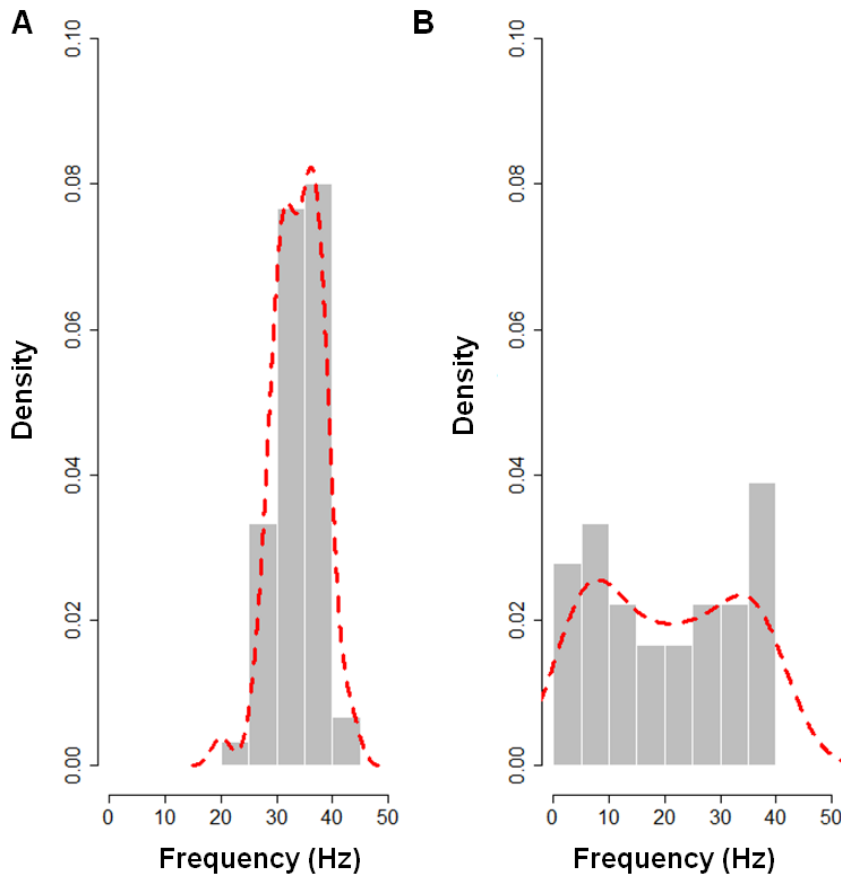


Figure 3.3 – *deltaD*^{-/-} cilia population with single and double CBFs. A- CBF frequency distribution of the cilia population that displays single CBFs; B - CBF frequency distribution of the cilia population that displays double CBF's.

Additionally, a population of immotile cilia was found in both WT and *deltaD*^{-/-} mutants (see movie S2), while a very low percentage of cilia (WT = 4%; *deltaD*^{-/-} = 3%) had a very irregular movement which did not translate in any measurable frequency when performing FFT analysis.

Since bright field high-speed imaging did not allow us to detect all the immotile cilia present in the KV we used confocal microscopy to film the entire volume of the KV of live embryos injected with *arl13b-GFP* mRNA (Figure 3.4 and movie S3 in Annex II).

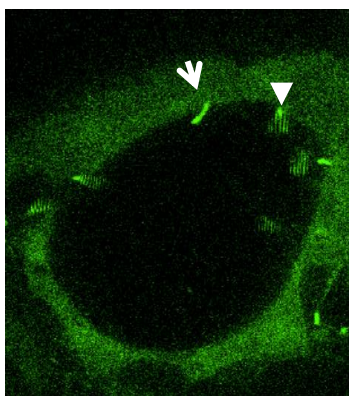


Figure 3.4 – KV of a live embryo with 14 hpf using fluorescent confocal microscopy – KV cells are labeled with the transgene *sox17:GFP*, cilia are also labeled with *arl13b-GFP* so that immotile cilia are bright and sharp (arrow) whereas motile cilia appear as cones with a blurred GFP label caused by the ciliary movement (arrow head).

In WT embryos we found 22% of cilia were immotile and their localization was random ($n = 7$ embryos; 300 cilia; Fisher test, $p > 0.05$), whereas in $\delta\text{eltaD}^{-/}$ mutants we found that only 15% of immotile cilia ($n = 8$ embryos; 240 cilia) were present (Figure 3.5). Both immotile and motile cilia were also visible by independent experiments using bright field high-speed imaging, which demonstrated that cilia immotility was not being caused by overexpression artefacts. This result establishes for the first time that, unlike medaka (Kamura *et al.*, 2011), zebrafish has both immotile and motile cilia in the KV.

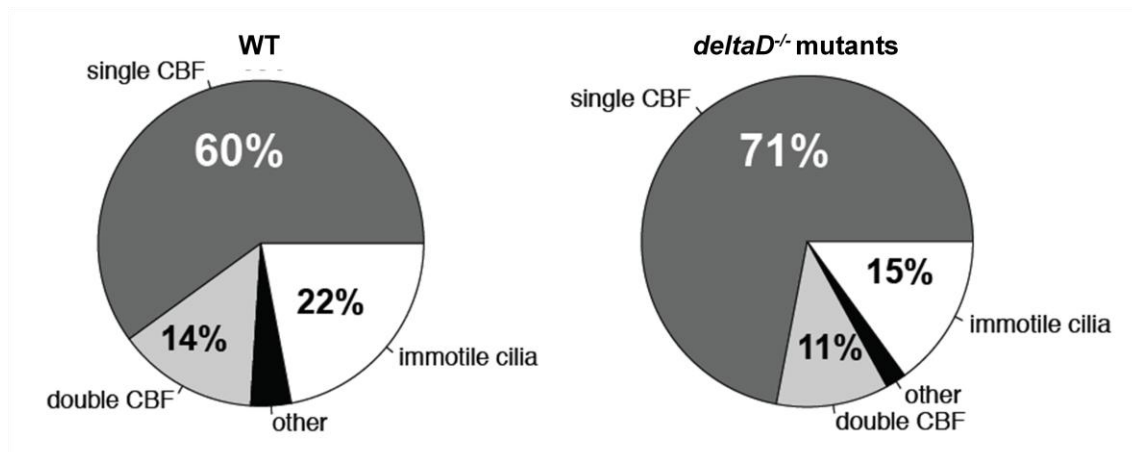


Figure 3.5 - Characterization of the wild-type and $\delta\text{eltaD}^{-/}$ KV cilia populations. Quantification of the different types of KV cilia according to motility and to CBF in (K) wt embryos; $n_e = 16$, $n_c = 80$ and in (L) $\delta\text{eltaD}^{-/}$ mutants; $n_e = 26$, $n_c = 77$. Kupffer's vesicle (KV); n_e (number of embryos); n_c (number of cilia).

Moreover, we observed that single and double-frequency cilia appeared to be distributed randomly, without any evidence of asymmetry, in WT and $\delta\text{eltaD}^{-/}$ mutants (Fisher test $p > 0.05$). Data were presented for a number of 60 cilia with a single beat frequency and 20 wobbling cilia in 16 wt embryos whereas in 26 $\delta\text{eltaD}^{-/}$ embryos we presented data for 60 and 17 cilia with single CBF and wobbling motion, respectively.

By measuring the length of a number of cilia for WT (Single CBF = 60, Wobbling = 13, Immotile = 10; 11 embryos) and $\delta\text{eltaD}^{-/}$ mutants (Single CBF = 103, Wobbling = 10, Immotile = 6; 15 embryos) which were previously recorded for CBF studies we saw that there was no correlation between the type of ciliary motility and cilia length (t-test $p > 0.05$).

3.2. Molecular study on *dnah7* motility gene downstream of DeltaD

In order to better understand the molecular players responsible for the cilia defects and laterality defects previously described in $\delta\text{eltaD}^{-/}$ mutants (Lopes *et al.* 2010), our lab decided to perform a tissue-specific screen using microarrays, revealing the transcriptome of the KV precursor

cells. The results showed the existence of more than 762 genes differentially expressed between WT and *deltaD*⁻ mutants. From those 762 differentially expressed genes, three were known to be related to cilia motility, namely *dnah7*, *foxj1a* and *rsph3*. According to the screen all the three genes were up-regulated in the *deltaD*⁻ KV precursor cells compared to WT (*dnah7*: p = 0.003; *foxj1a*: p > 0.05; *rsph3*: p = 0.029).

Among these genes, *dnah7* shown to be the most promissory to address the laterality problems verified in *deltaD*⁻ mutants. *Dnah7* is a heavy chain axonemal dynein and is located at the inner dynein arms of ciliary axonemes. It was found to be missing in respiratory cilia of one patient with Primary Ciliary Dyskinesia who had a deficiency of inner dynein arms and displayed abnormal cilia motility (Zhang *et al.*, 2002).

Taking into consideration that 50% of PCD patients present *situs inversus*, we decided to further study this cilia motility-related gene. *Dnah7* was never characterized before in any animal model and therefore we report here a description of its knockdown phenotype and the gene expression pattern through various development stages of zebrafish embryos by using whole-mount *in situ* hybridization (WISH) experiments.

3.2.1. *dnah7* knockdown in zebrafish rendered immotile cilia

We next explored the knockdown of a heavy chain axonemal dynein *Dnah7* by injecting a specific translation blocking morpholino (*dnah7*-MO) and the respective mismatch control morpholino (Control-MO) in WT embryos.

High dosage (12ng and 6ng) of *dnah7*-MO showed to be completely lethal for WT embryos, and although lower doses (3ng and 2.6ng) demonstrated a considerable effect in WT embryos resulting in phenotypic severity and high mortality rates (\approx 80% and 70%, respectively), this MO dosage range yielded >90% penetrance (injected embryos showed a specific phenotype). The same dosage of Control-MO (3ng) showed the same phenotypic behavior of non-injected embryos with a low mortality rate (\approx 15%) validating the specificity of the *dnah7*-MO.

Our results showed that *dnah7* knockdown embryos rendered immotile cilia very effectively all over the KV (Movie S4 in Annex II) while *dnah7* mismatch MO-control did not affect cilia motility (Movie S5 in Annex II). The *dnah7*-MO injected embryos allowed us to scan for how many motile cilia remained in each embryo confirming it by kymograph analysis (Figure 3.6c,d). Only an average of 2 cilia per embryo maintained its motility. However, in contrast to WT cilia (t-test p < 0.05), these presented a higher variability of CBF's (Figure 3.6a,b). Data were presented for a number of 26 cilia in 15 *dnah7* morphant embryos.

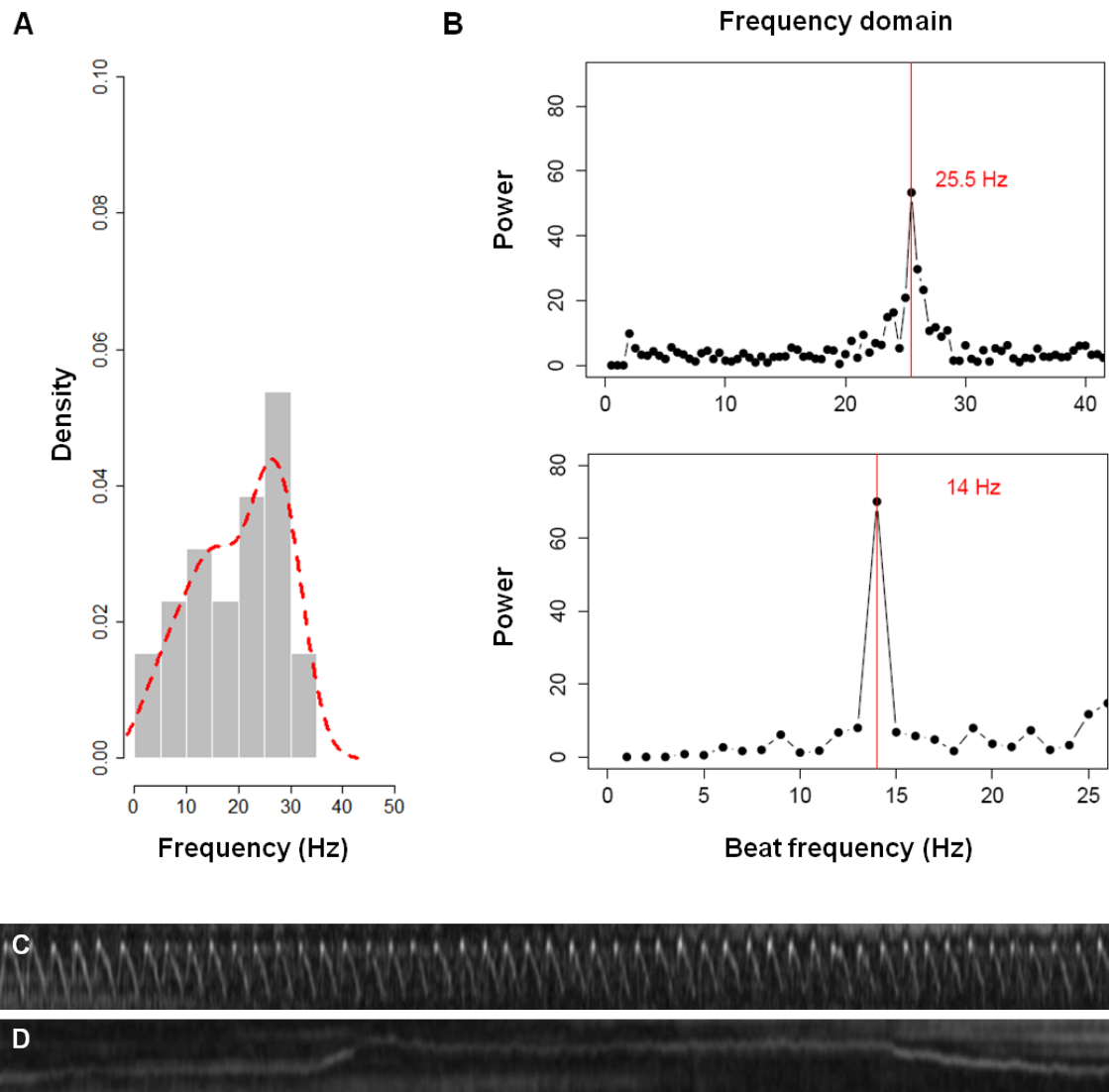


Figure 3.6 – *dnah7*-MO cilia population with single CBFs. A - CBF frequency distribution of the cilia population that displays single CBFs. B - Representative results from two cilia with single CBF's after FFT spectral analyses; C - Kymograph of one motile cilium from a *dnah7* knockdown embryo showing a consistent beat frequency over 2 seconds filmed with 500 fps.. D – Kymograph of a cilium from a *dnah7* knockdown embryo that shows no active motility over 2 seconds at 500 fps. CBF (cilia beat frequency).

In addition, was clearly visible that injected embryos had a slower heart beating rate that uninjected WT embryos.

Altogether, our data for WT and *deltaD*^{-/-} embryos revealed two different populations of motile cilia based on the criteria of CBF number by spectral analysis using FFT, and one population of immotile cilia. On the other hand, *dnah7* knockdown showed that this protein has an important role for cilia motility and turned out to be a very good tool for further reducing KV fluid flow.

3.2.2. Immunofluorescence experiments in *dnah7*-MO injected embryos

It was crucial to check if the phenotype detected in the KV motile cilia of the *dnah7* morphant was affecting motility alone or other parameters such as cilia number and length. As described previously in Materials and Methods, after imaging MO-injected embryos these were fixed for immunostaining at 8 somite stage by labeling an acetylated form of α -tubulin which is present the cilia structure (Figure 3.7).

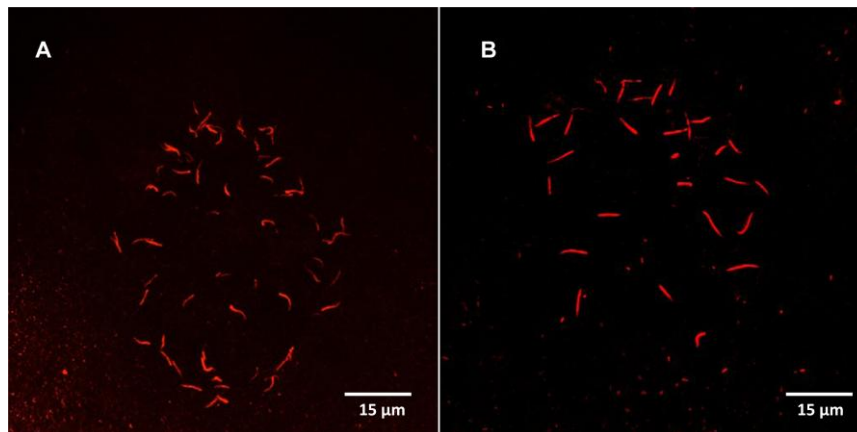


Figure 3.7 – Immunofluorescence experiment for visualizing KV cilia. Immunodetection with anti-acetylated α -tubulin (1:400) to visualize the presence of KV cilia in a *dnah7*-MO injected (A) and in WT embryos (B).

Our results showed that *dnah7*-MO injected embryos disrupted cilia motility without affecting their number relative to control embryos. Also, KV cilia length in *dnah7* morphants does not seem to have changed significantly compared with WT embryos (Figure 3.8) (t-test $p > 0.05$). Data were presented for a number of 200 cilia in 5 WT embryos and 172 cilia in 3 MO-injected embryos.

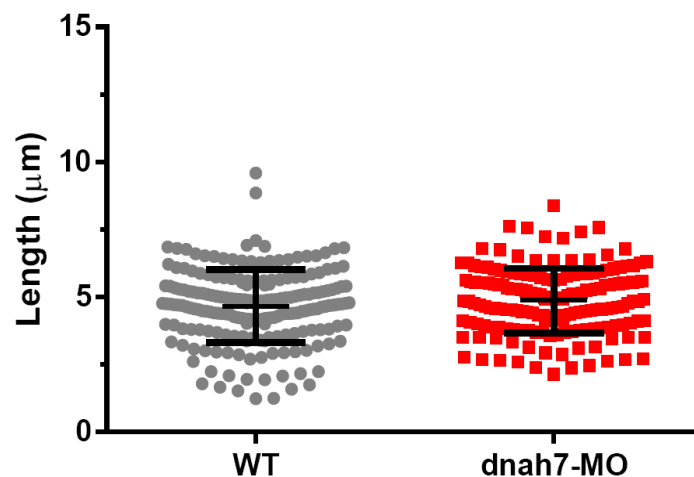


Figure 3.8 - Cilia length measurements in WT and *dnah7* morphants. Dot plot of length per cilia in WT embryos (n=5) and *dnah7* morphants (n=3).

3.2.3. Time-course study of the expression pattern for *dnah7*

The characterization of cilia beat frequency in *dnah7* morphants pointed out a role of the inner dynein *dnah7* in cilia motility. Moreover, inner dynein defects have been recently associated with ciliopathies (Shoemark *et al.*, 2013; Zhang *et al.*, 2002) which prompted us to further study the *dnah7* cilia motility-related gene by doing a whole-mount *in situ* hybridization (WISH) experiment to validate if this gene was expressed in ciliated organs of WT zebrafish embryos at various stages of development.

3.2.3.1. *dnah7* gene expresses in ciliated organs during zebrafish embryogenesis

To have an insight of *dnah7* mRNA distribution throughout embryogenesis and to evaluate if it is expressed in ciliated organs, namely in the Kupffer's vesicle, we performed a time course study of this gene expression in zebrafish embryos by *in situ* hybridization. In this experiment we used *ntl* (no-tail) a gene homologous to *brachyuri* in mouse, as positive control of the WISH experiments (Figure S2 in Annex II).

At bud-stage, *dnah7* gene expression was restricted to the dorsal forerunner cells (KV precursor cells) and to the KV at 8 somite-stage WT embryos (Figure 3.9) as expected.

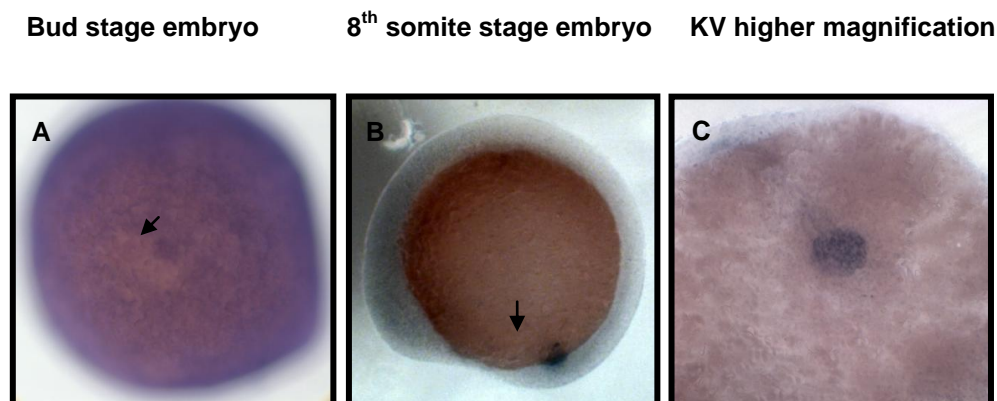


Figure 3.9 – WISH experiment for *dnah7* gene in WT bud and 8th somite stage embryos. WT embryos revealed *dnah7* expression in KV precursor cells at bud stage (A, arrow) and in the KV at 8th somite stage stage (B – arrow; C).

Around 12-16hpf *dnah7* was detected in a set of structures, namely in the pronephros, and brain ventricles (Figure 3.10) both known to be lined by cells with motile cilia (Kramer-Zucker *et al.*, 2005).

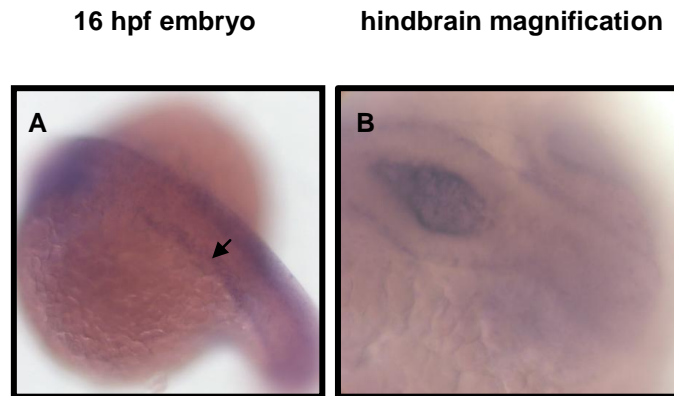


Figure 3.10 - WISH experiment for *dnah7* gene in WT 16 hpf. Pronephric duct (A, arrow) and hindbrain, a roughly triangular shaped structure (B).

In the following stages *dnah7* gene expression was also verified in the above organs and in other developing ciliated organs: posterior tail dorsal region and proximal pronephric tubules (24 hpf), brain ventricles, (24hpf and 48hpf), otic vesicles (24 and 48 hpf), olfactory pits and in the heart (48hpf) (Figure 3.11 and 3.12).

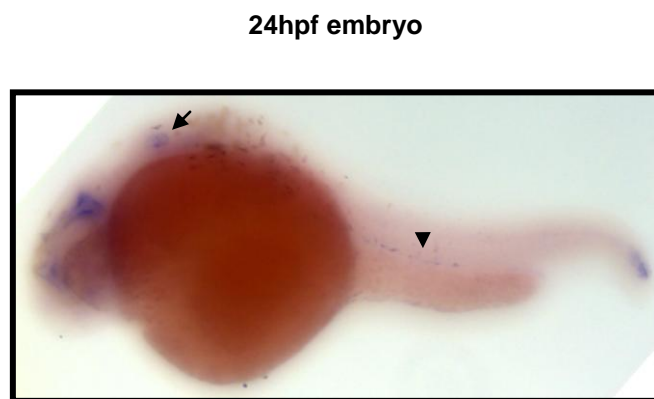


Figure 3.11 - WISH experiment for *dnah7* gene in WT 24 hpf. Brain ventricles, otic vesicles (arrow), proximal pronephric tubules (arrowhead) and posterior tail dorsal region.

48hpf embryo

Ventral view

Lateral view

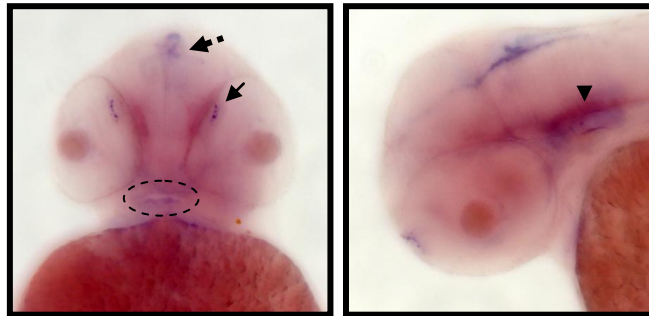


Figure 3.12 - WISH experiment for *dnah7* gene in WT 48 hpf hpf. Ependymal cells in the brain ventricle (dashed arrow), olfactory pits (arrow), otic vesicle (arrowhead) and heart (dashed circle).

These findings suggest that *dnah7* gene expression is confined to ciliated organs of the zebrafish embryo.

3.2.3. Zebrafish heart and liver laterality screening

Previous studies in mouse, zebrafish and medaka have linked immotile cilia with L-R defects (Essner *et al.*, 2005; Supp *et al.*, 1999) so, we wanted to evaluate the impact that the lack of cilia motility seen in *dnah7* morphants had on heart and liver positioning, which are the main organs to be affected in these cases. WT, *deltaD*^{-/-} mutants, *dnah7* morphants and MO-*dnah7* control embryos were scored for heart asymmetry *in vivo* and made use of the gut transgenic line *sox17*:GFP in live embryos for scoring liver and pancreas position (see Materials and Methods Chapter). According with the specific outcome of these internal organs position along the left-right body axis embryos were classified as: *situs solitus* (normal arrangement, having heart and liver on the left side), *heterotaxia* (normal heart position with central or right liver position), *situs inversus* (both heart and liver on the right position) or *situs ambiguus* (both heart and liver with centralized position).

Our results showed that 10% of the WT embryos (number of embryos = 112) have L-R defects (Figure 3.13), in which 60% of these only referred to the liver position. In the other hand *deltaD*^{-/-} (number of embryos = 26) we only detected liver and pancreas laterality defects (heterotaxia), which are concordant with the previous literature (Lopes *et al.*, 2010).

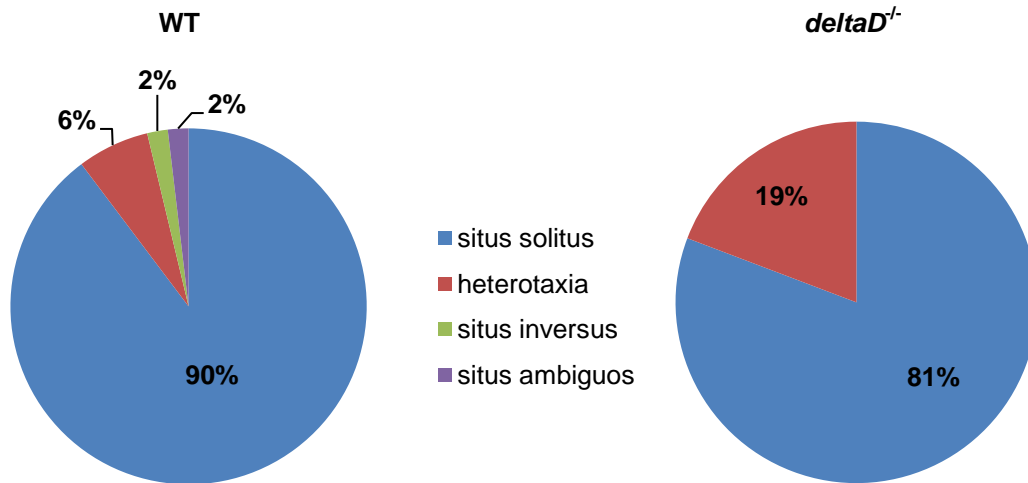


Figura 3.13 - Screening of heart and liver orientation in WT and *deltaD*^{-/-} embryos. WT (ne = 112) and *deltaD*^{-/-} (ne = 26). ne (number of embryos).

For *dnah7* morphant embryos (number of embryos = 80) we have identified several L-R defects which confirms the major role that cilia motility has in organ lateralization (Figure 3.14). We also noticed that normally *dnah7*-MO injected embryos died before reaching 4 dpf. *Dnah7*-MO mismatch controls (number of embryos = 53) showed minor L-R defects.

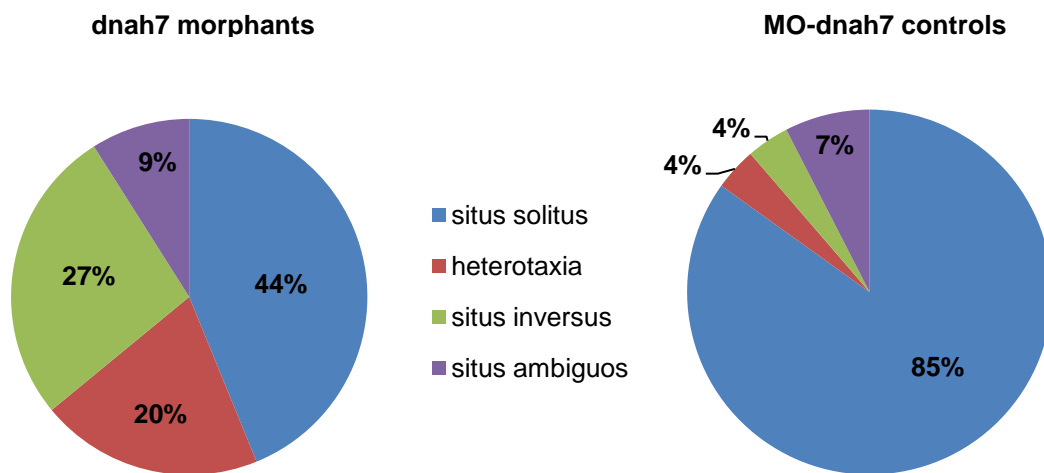


Figure 3.14 - Screening of heart and liver orientation in *dnah7* morphant and MO-Control embryos. *dnah7* morphants (ne = 80) MO-Control embryos (ne = 53). ne (number of embryos)

Motile cilia are known to play an essential role in the L-R patterning by generating a directional fluid flow inside the L-R organizers, and it has been shown that when nodal flow malfunctions or is artificially reversed, L-R asymmetric localization of internal organs is affected (Nonaka *et al.*, 2002; Flieugauf *et al.*, 2007). Thus, these results indicated to us that defects for cilia motility identified here in *dnah7* morphants might be the source of organ laterality abnormalities by disturbing KV fluid flow. Therefore, the next objective was to evaluate the fluid flow produced by these morphants and correlate them with heart and liver-pancreas lateral positioning.

3.3. Kupffer's vesicle fluid flow velocity measurements

The following step was to address *situs* abnormalities seen in *deltaD*^{-/-} mutants and *dnah7* morphants by evaluating if the directional fluid flow inside the KV had any correlation with these *situs* defects.

Since CBF, together with cilia number and length impacts fluid flow velocity we decided to investigate the relevance of these parameters by using *deltaD*^{-/-} mutants that exhibited a range of cilia number and lengths but lack major KV morphology defects (Lopes *et al.*, 2010) and by using the novel *dnah7* knockdown tool which enabled us to genetically manipulate the number of motile versus immotile cilia experimentally.

3.3.1. *deltaD*^{-/-} mutant embryos and *dnah7* morphants generated a range of flow patterns

We produced flow trajectory maps for each embryo genetic background (Figure 3.15). These maps provided visual information about the pattern and the relative velocity of the fluid flow in the KV.

Our results showed that the zebrafish KV is a site of dynamic cilia-driven fluid flow where we observed that flow occurs in a circular, counterclockwise direction (see Movie S6 in Annex II) in WT, *deltaD*^{-/-} mutants and *dnah7* MO-controls. However *deltaD*^{-/-} mutants presented a range of flow patterns, some of which had lower velocities than WT (Figure 3.15 - A, B, C). For *dnah7* morphants we could see that the directional fluid flow was completely disrupted (Figure 3.15 - D and Movie S4 in Annex II) because embryos presented a very low speed characterized by a presumably random movement of particles, called Brownian motion. Fluid flow in *dnah7* control-MO injected embryos seemed not to be affected (see Movie S5 in Annex II)

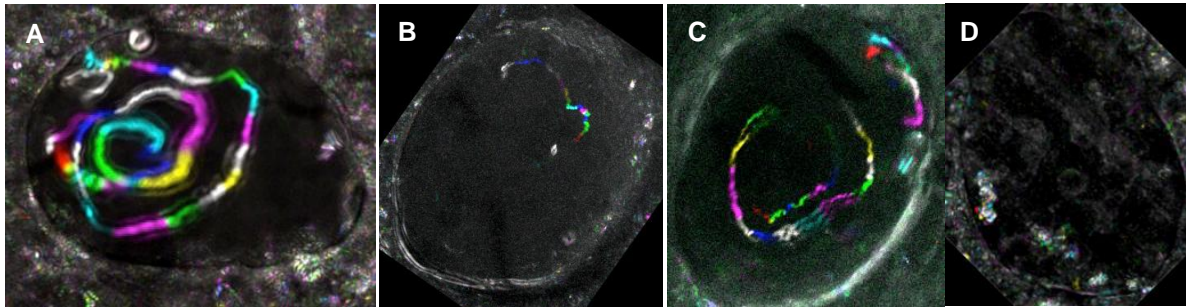


Figure 3.15 - Representative KV flow maps. Produced trajectory flow maps for a WT embryo (A), for two different *deltaD*^{-/-} mutant embryos (B and C), and for a MO-*dnah7* injected embryo (D). Each track color corresponds to 1 second (red track corresponds to the first second). Left is to the left and anterior to the top throughout.

To confirm these results we measured the flow velocity by manually tracking native particles that did not get trapped by cilia to avoid measuring the vortical fluid flow described by (Supatto *et al.*, 2008). Importantly, this work differs from previous studies (Supatto *et al.*, 2008), in the fact that our method was completely non-invasive, which safeguarded the epithelium and natural osmotic pressure inside the KV. We have successfully imaged 7 WT embryos, 26 *deltaD*^{-/-} embryos, 9 *dnah7* morphants and 5 *dnah7* MO-controls.

Furthermore, in order to explore the biological significance of fluid flow, we kept the embryos alive after imaging the movement of KV native particles in four genetic manipulations: WT, *deltaD*^{-/-} mutants, embryos injected with *dnah7* morpholino (MO) and embryos injected with the respective five-mismatch control-MO.

After 30 hours post fertilization (hpf) we evaluated heart jogging and after 50 hpf, we assessed gut laterality by observing live larvae from the transgenic lines *tg(sox17:GFP)^{s870};deltaD^{-/-}* and *tg(sox17:GFP)^{s870}* that express GFP in the developing gut, allowing for visualization of the liver, pancreas and intestinal bulb position (Figure 3.16).

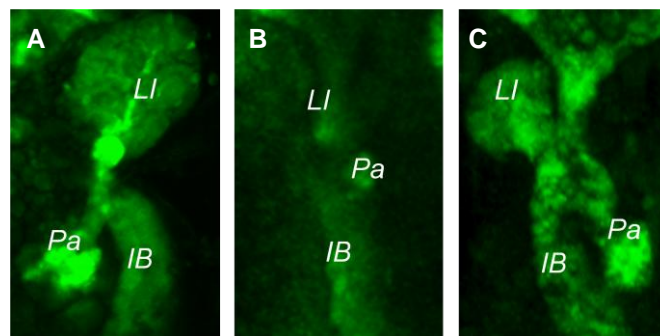


Figure 3.16 - Gut laterality at 50 hpf. Z projection showing the liver, pancreas and intestinal bulb of a (A) WT embryo *tg(sox17:GFP)^{s870}*, (B) *deltaD*^{-/-} mutant in the same genetic background and developmental stage showing a gut without lateralization and (C) another *deltaD*^{-/-} mutant showing reversed organ position. Li liver; Pa pancreas; IB intestinal bulb.

The results showed that we were successful in generating a range of flow speeds (Figure 3.17). WT larvae, *deltaD*^{-/-} mutants with *situs solitus* and *dnah7* control-MO presented faster fluid flow speeds (Figure 3.17, Wilcoxon test, $p < 0.05$);). All these larvae displayed a left position of the heart and liver (*situs solitus*). Next, *deltaD*^{-/-} mutant larvae displaying hearts on the left but showing central and right livers (heterotaxic embryos) presented a clearly slower flow speed than WT embryos (Figure 3.17, Wilcoxon test, $p < 0.05$). At this stage we realized that *deltaD*^{-/-} embryos with the weakest flow speed developed livers in central positions. Furthermore, embryos knockdown for *dnah7* presented even lower speed flows, most of the times characterized by simple Brownian motion (Figure 3.17 and Movie S4 in Annex II). These embryos presented either no motile cilia or few motile cilia resulting in larvae with very different *situs* outcomes.

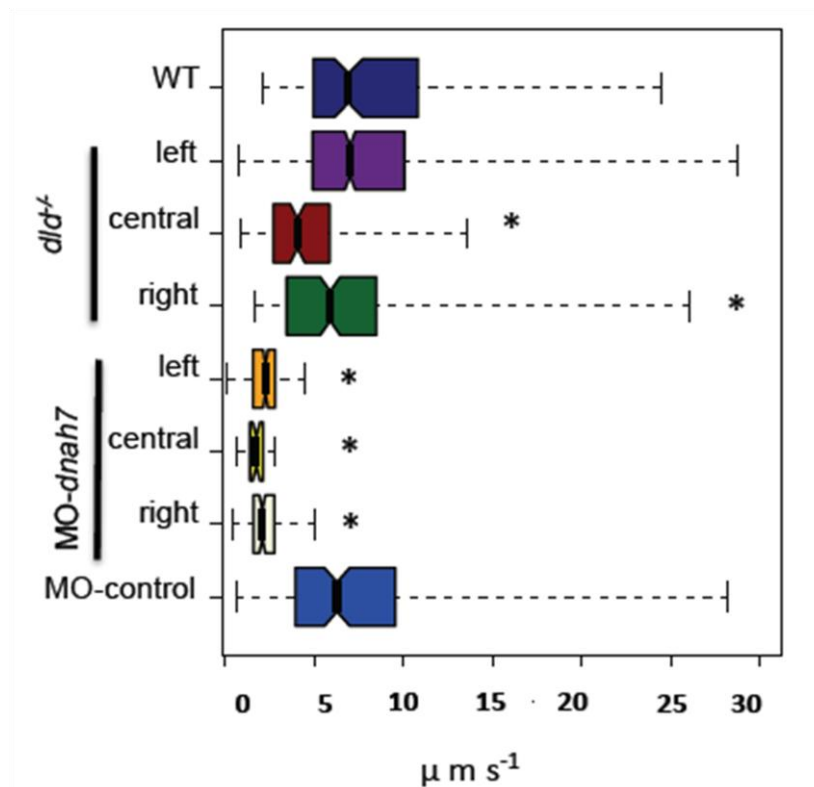


Figure 3.17 - Genetically generating a range of fluid flow speeds. Box plot of flow speed in WT, *deltaD*^{-/-} embryos and MO-*dnah7* injected embryos ($p < 0.05$, Wilcoxon test). Left, central and right conditions refer to liver situs. The total number of tracks (n_t) and embryos (n_e) followed with native particles for each condition was as follows: WT $n_t = 847$, $n_e = 7$; for *deltaD*^{-/-} mutants with left liver $n_t = 7877$, $n_e = 21$; for *deltaD*^{-/-} mutant with centralized livers $n_t = 1458$, $n_e = 2$; for *deltaD*^{-/-} mutants with right liver $n_t = 858$, $n_e = 3$; for *dnah7* knockdown embryos with left liver $n_t = 1105$, $n_e = 3$; for *dnah7* knockdown embryos with central liver $n_t = 505$, $n_e = 1$; for *dnah7* knockdown embryos with right liver $n_t = 1860$, $n_e = 4$ and for *dnah7* mismatch control-MO $n_t = 1700$, $n_e = 5$.

In search for factors that could explain how relatively similar fluid flow speed gives rise to both left and right organ laterality, we re-examined the flow trajectories and their speed with more detail. First, we analyzed the tracking of all the native particles in each KV and realized that the most peripheral trajectories in each KV, those closer to the ciliary tips, were not evenly radially distributed from the KV centre (Figure 3.18 A, D, G, J). According to our results the trajectories preferentially

localized to the anterior-left region in case of *situs solitus*, however in the case of heterotaxic embryos these trajectories showed a different behavior. In *deltaD*^{-/-} embryos in which the liver positioned to the right the trajectories preferentially localized to the right, whereas in embryos with centralized liver the trajectories occurred preferentially in the left-posterior region. To further investigate the reason of these events, we next examined if these trajectories had slower or faster flow speeds. For this purpose we measured the instantaneous flow speed in each half of the KV (Figure 3.18 B, E, H, K, N) and made heat maps of flow speed to achieve more local detail within each KV half (Figure 3.18 C, F, I, L). The results showed that the average flow speed was significantly faster on the anterior half of the KV in all situations ($p < 0.05$) except for the central liver cases (Figure 3.18 H, I). In the *situs solitus* cases (Figure 3.18 B, E) the next highest speeds were registered on the left halves of the KV, which is also visualized by the corresponding heat maps (Figure 3.18 B, E). Regarding the mutant *deltaD*^{-/-} embryos with central livers, fluid flow was weak and homogenous all over the KV (Wilcoxon test $p > 0.05$). In contrast, for heterotaxic embryos with right livers, the flow was still stronger anteriorly but between left and right sides there was no significant difference (Wilcoxon test $p > 0.05$). However, the heat maps show a stronger local increase on the right side of speed values (Figure 3.18 L).

These higher resolution results for localized flow made us suspect that the local flow felt at the KV periphery, where cilia are located, was likely stimulating neighboring cilia and starting the next signaling events that lead to the asymmetric gene expression and concomitant L-R patterning. In other words, our data could be pointing to a mechanosensory role played by the cilia that were being stimulated by the local flow.

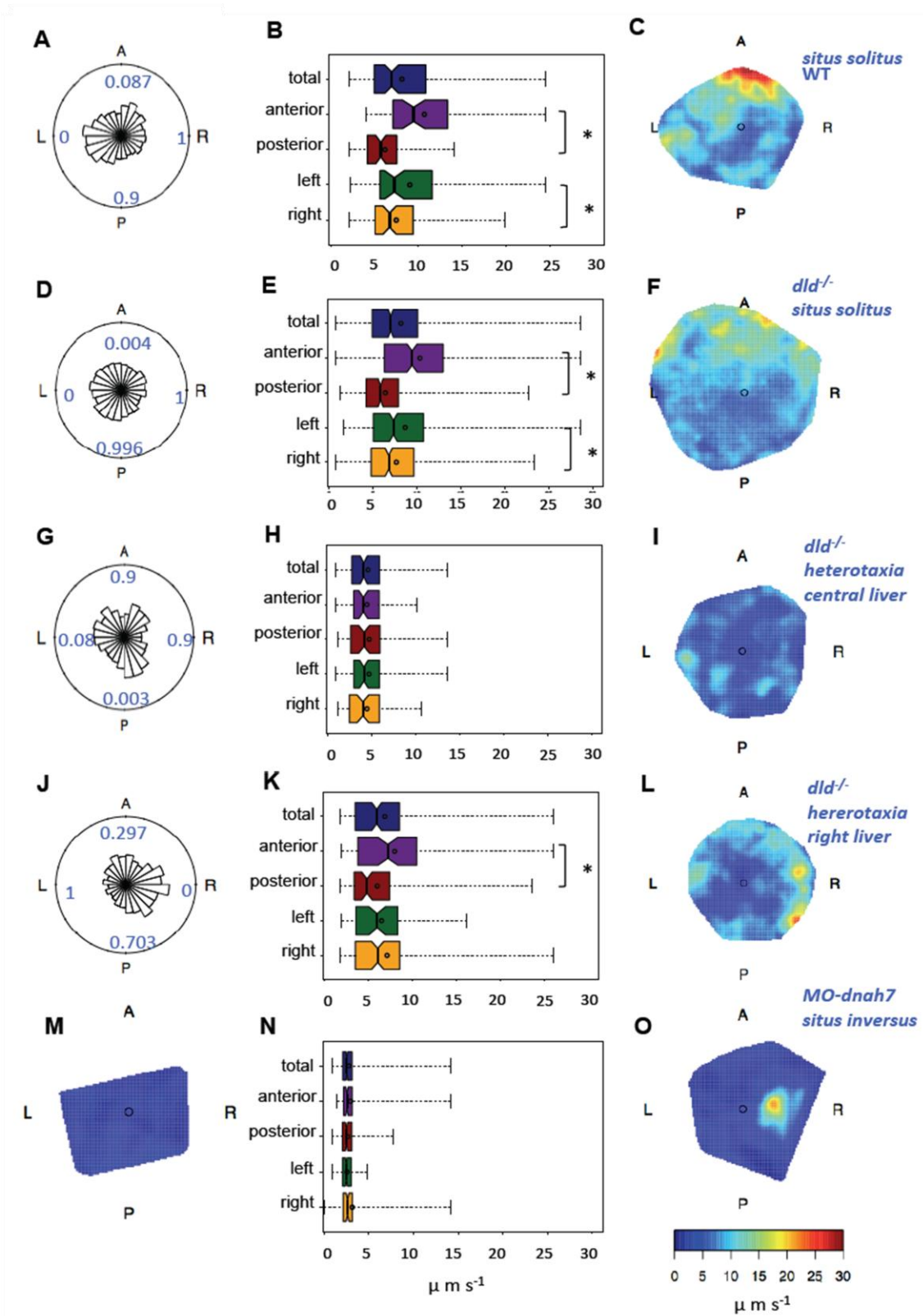
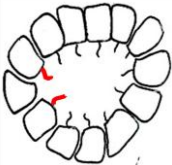
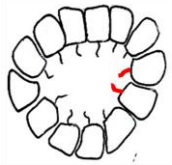


Figure 3.18 - Experimental flow measurements . (A, D, G, and J) Probability of finding and tracking native particles within the KV represented as rose diagrams. Data obtained from pooled embryos with 14 hpf of each experimental condition: WT (A, $n_t = 675$, $n_e = 7$), *deltaD*^{-/-} mutants with left liver (D, $n_t = 4742$, $n_e = 21$), *deltaD*^{-/-} mutant with central livers (G, $n_t = 895$, $n_e = 2$) and *deltaD*^{-/-} mutants with right liver (J, $n_t = 723$, $n_e = 3$). Rayleigh tests were performed considering a null hypothesis of a bias distribution towards a given KV quadrant, p – values are indicated as blue numbers. Note that only particles moving at a

distance of $r > 0.5$ from the centre of the KVs were considered (r is the normalized distance from the centre ($r = 0$) to the wall ($r = 1$) of the KV). (B, E, H, K and N) Box plots for instantaneous flow speed measured at different locations of the KVs for pooled embryos in each experimental condition, WT (B, $n_t = 847$, $n_e = 7$), *deltaD*⁻¹ mutants with left liver (E, $n_t = 7877$, $n_e = 21$), *deltaD*⁻¹ mutant with central livers (H, $n_t = 1458$, $n_e = 2$), *deltaD*⁻¹ mutants with right liver (K, $n_t = 858$, $n_e = 3$) and *dnah7* morphants with *situs inversus* (N, $n_t = 1297$, $n_e = 2$). (C, F, I, L, M and O) Heat maps of flow speed showing detailed regions within each KV based on the dataset used to generate the box plots of panes B, E, H, K and N. (M) heat map for a *dnah7* morphant without any cilia. The pseudo-colour scale represents flow speed in $\mu\text{m s}^{-1}$. A (anterior); P (posterior); R (right); L (left). n_e (number of embryos) and n_t (number of tracks followed).

To test the mechanosensory hypothesis further we used the *dnah7* knockdown embryos where we could precisely select the cases with only very few motile cilia located clearly on the left or on the right side of the KV. In these embryos, the presence of 1-3 motile cilia results in a very localized fluid flow close to the cilia and therefore could allow us to relate this position to subsequent organ *situs* (Figure 3.18 M, O). The results showed that embryos without any motile cilia had no significant flow and preceded *situs* randomization, presenting 50% *situs solitus*, 30% *heterotaxia* and 20% *situs inversus* ($n=10$ embryos; see heat map in Figure 3.18 M). We then focused on six embryos that had only one or two motile cilia clearly placed on the left or right side of the KV. We found that five out of six embryos had the liver and heart concordant and on the same side as the motile cilia we had screened for (Table 3.1). In three of these embryos with cilia positioned on the right side, the presence of native particles allowed us to measure flow and identify a localized hotspot on the right side of the KV, which preceded *situs inversus* (Figure 3.18 N, O). These experiments support the hypothesis that in the presence of immotile cilia a clear local flow stimulus generated by motile cilia can influence organ *situs*.

Table 3.1 - Screening of organ *situs* in *dnah7* morphant embryos. Fate of the organs *situs* in three different situations: absence of motile cilia, left-sided motile cilia and right-sided motile cilia. Schematic representation indicates the location of motile cilia (red). Data obtained from 16 *dnah7*-MO injected embryos.

	<i>Situs solitus</i>	<i>Heterotaxia</i>	<i>Situs inversus</i>
No motile cilia	5:10	3:10	2:10
	2:2	0:2	0:2
	1:4	0:4	3:4

Thus, our results support a model in which asymmetric flow forces may dictate organ laterality in each embryo. We observed that asymmetric and repetitive swirls of flow occur for several hours.

Our prediction is that the viscous stresses closer to the ciliated walls of the KV will repeatedly stimulate the sensory cilia and likely trigger a mechanosensory response in these cells.

3.4. *In silico* flow studies

In our experiments we followed as many native particles as possible, however it was not always possible to have a perfect coverage of mid plane flow fields. So, in order to better characterize these flow fields and to relate more clearly the effect of observed parameters to flow behavior we conducted *in silico* 'experiments', by mathematically modeling KV fluid flow. For this purpose we collaborated with the lab of David Smith in Birmingham University and worked together for updating their last published model (Smith *et al.*, 2012), which already incorporated many important experimental KV data. Variables such as cilia density in different regions of KV and a mixture of cilia dorsally and posteriorly tilted were integrated into a 3D, time-dependent computational simulation resolved at the level of individual cilia length and beat pattern (Smith *et al.*, 2012).

The improved model for the new flow field simulations additionally included the distribution of cilia length, measured in 3D after performing immunofluorescence with anti-acetylated α -tubulin for 27 wt embryos, (639 cilia in total) and for 17 *deltaD*^{-/-} mutants, (280 cilia in total; Figure 3.19). Cilia length distribution was repeated across multiple statistical samples to take into account the heterogeneity observed experimentally. Results showed that *deltaD*^{-/-} mutants tend to have shorter cilia than in WT embryos (t-test $p < 0.05$). These measurements were done by a colleague Petra Pintado in the lab.

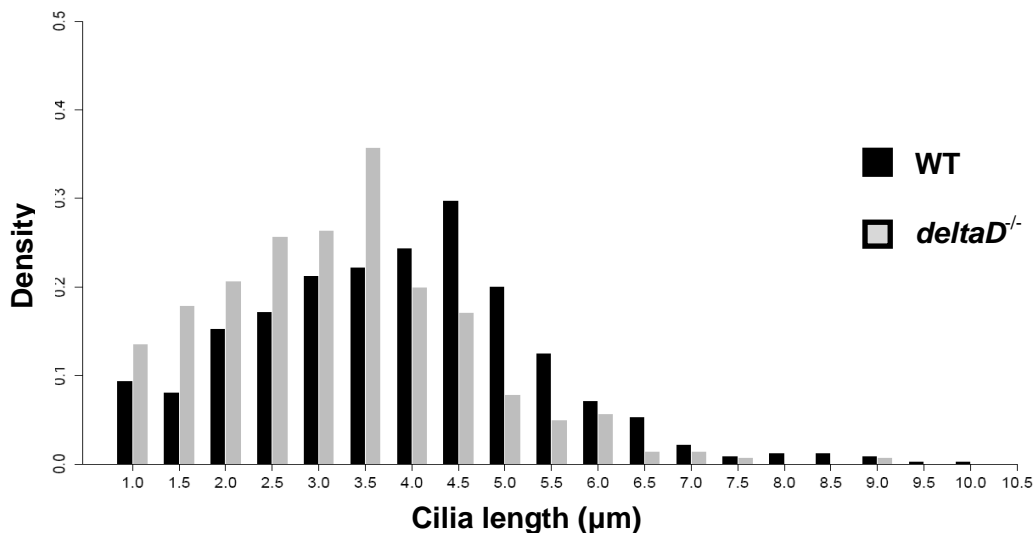


Figure 3.19 - Cilia length distribution in WT and *deltaD*^{-/-}. Experimental 3D measurements for modeling in WT (ne=27, nc=639) and *deltaD*^{-/-} mutant embryos (ne=17, nc=280).

With the same data collection we were able to quantify the number of cilia present in the embryos KVs (Figure 3.20). Our results showed that *deltaD*^{-/-} mutants have significantly less cilia when compared with WT embryos (t-test p < 0.05).

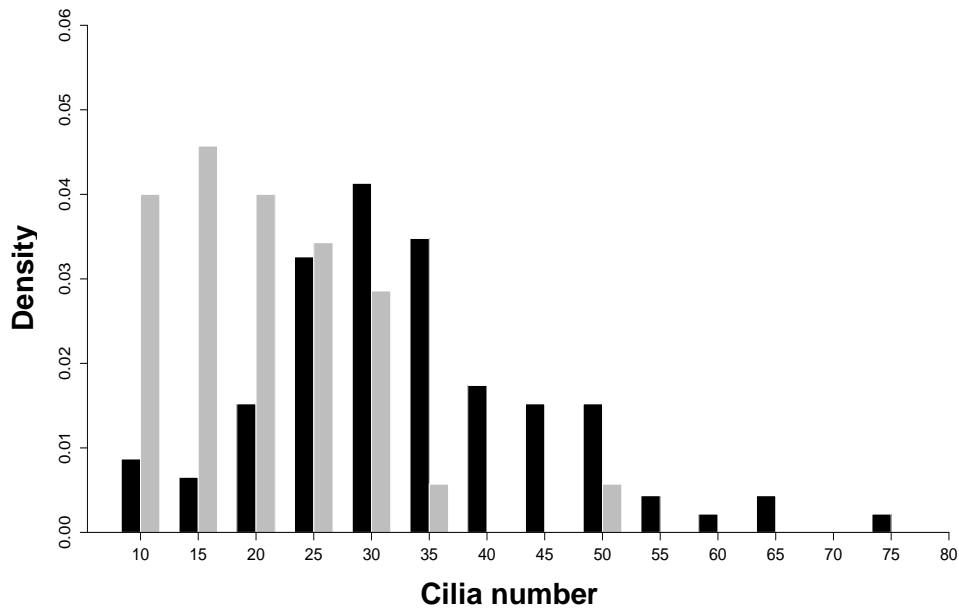


Figure 3.20 - Cilia number distribution in WT and *deltaD*^{-/-}. Experimental quantification in WT (ne=27) and *deltaD*^{-/-} mutant embryos (ne=17).

In addition, another colleague in the lab, Bárbara Tavares filmed live embryos, transgenic for *sox17:GFP*, thus having the KV cells expressing GFP, in order to measure the real volume of several KVs both for WT and *deltaD*^{-/-} mutants and use it in the simulations (n=8 KVs each condition, Figure 3.21).

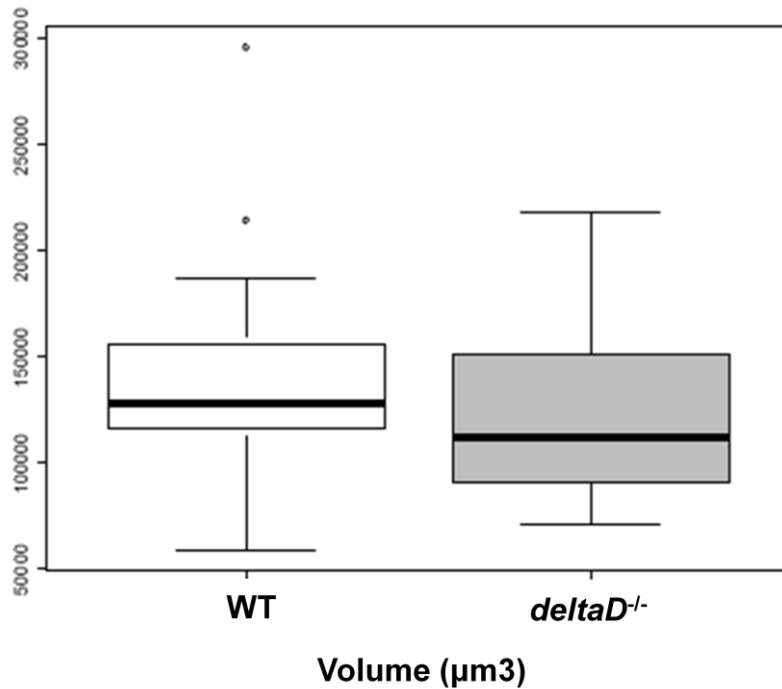


Figure 3.21 - Experimental measurements for KV volume of WT and *deltaD^{-/-}* mutant embryos. Box plots for KV volume measurements WT (n=18) and *deltaD^{-/-}* mutant embryos (n=20).

To produce better simulations we realized that the number of motile and immotile cilia and their localization were extremely important parameters that could be extracted from the analysis referred above by injecting *arl13b-GFP* to label ciliary axonemes. So, Bárbara Tavares performed those experiments and delivered the number of motile and immotile cilia for each condition. In addition, the immotile cilia were checked by CBF analysis performed by me.

Our team goal was to input into the model all the relevant experimental data including the distribution of cilia beat frequencies for each of the genotypes, a feature which had not previously been included in models of organizing structures.

3.4.1. Cilia number variations affect KV fluid flow

In order to introduce the new CBF parameters (reported here previously) into the simulations we had to first create a model for cilia that beat with two or more frequencies, the wobbling cilia model (see Annex II). These wobbling cilia, together with single frequency and immotile cilia identified above were then used to seed the KV meshing in a differentiated dorsal-ventral density (see Annex II). The results of this type of modeling allowed for clear visualization of the flow forces within the KV in any plan we desire (Figure 3.22).

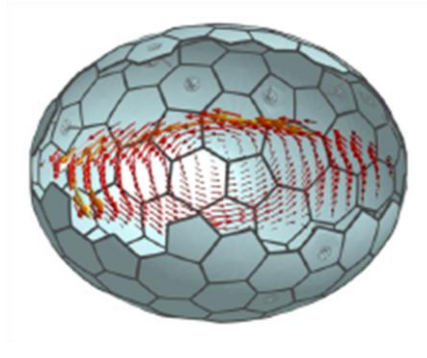


Figure 3.22 - Generating a detailed computational mesh of Kupffer's Vesicle - The time-averaged fluid flow generated in the Coronal plane of a model *deltaD^{-/-}* embryo with 36 cilia, looking towards the anterior dorsal corner, where the number density of cilia is highest. The computational mesh is also shown, with the posterior dorsal sector removed for better visualization.

The resulting simulations for eight different KV cilia numbers (based on the range of cilia numbers observed in the experimental studies, see Figure 3.20) allowed us to quantify the number of cilia sufficient to reproduce in simulations the experimental behaviors observed in Figure 3.18. Comparing the simulated flow (Figure S3 and S4 in Annex II) with the real flow (Figure 3.18) in the anterior and posterior halves we observed that 24 out of 25 experiments had anterior flow much faster than posterior (binomial test, $p < 0.001$), showing that the anterior cluster of motile cilia was retained in the mutants except for the very low flow embryos presenting a central liver (Figure 3.18 H). It is clear that anterior flow becomes stronger in the *deltaD^{-/-}* mutants as more cilia are added to the simulation (Figure S4 in Annex II). This fact shows that central liver in *deltaD^{-/-}* mutants, must be an event triggered by either very few cilia equally placed in the KV four quadrants or simply by very short cilia producing almost no flow, such as the predicted flow simulation 22_4 (Figure 3.23 J, K, L) that corresponds to the experimental flow heat map on Figure 3.18 I. Based on this reasoning we matched the averaged flow speed data calculated for every KV half in WT (Figure 3.18 B) and in *deltaD^{-/-}* mutants (Figure 3.18 E,H,K) to simulations that exemplified the observed flow behaviours (Figure 3.23 B, H, K, N) to determine what features of cilia number and placement may be underlying the observed flow. Accordingly, simulation 60_1 (Figure 3.23 A-C) was matched to WT with *situs solitus* (Figure 3.18 A-C); simulation 29_3 (Figure 3.23 G-I) to *deltaD^{-/-}* mutants with *situs solitus* (Figure 3.18 D-F); simulation 22_4 (Figure 3.23 J-L) was matched to *deltaD^{-/-}* mutants with central liver *situs* (Figure 3.18 J-L) and simulation 22_2 (Figure 3.23 M-O) was matched to *deltaD^{-/-}* mutants with right liver *situs* (Figure 3.18 J-L).

By examining the placement of motile cilia in these simulations (Figure 3.23 A, G, J, M) we see anterior clustering for left liver *situs*, homogeneous cilia placement in central *situs* and slight right-sided clustering for right *situs*. These results show that the probability of producing the observed behaviours is correlated positively with cilia clustering. However, even in WT situations, if the number of cilia is below 30 (see Figure S3 in Annex II) we could predict for example by simulation 25_1 (Figure 3.23D-F) that an abnormal flow may arise if we disrupt the dorsal anterior cluster of motile cilia, likely generating larvae with *situs inversus* or heterotaxia.

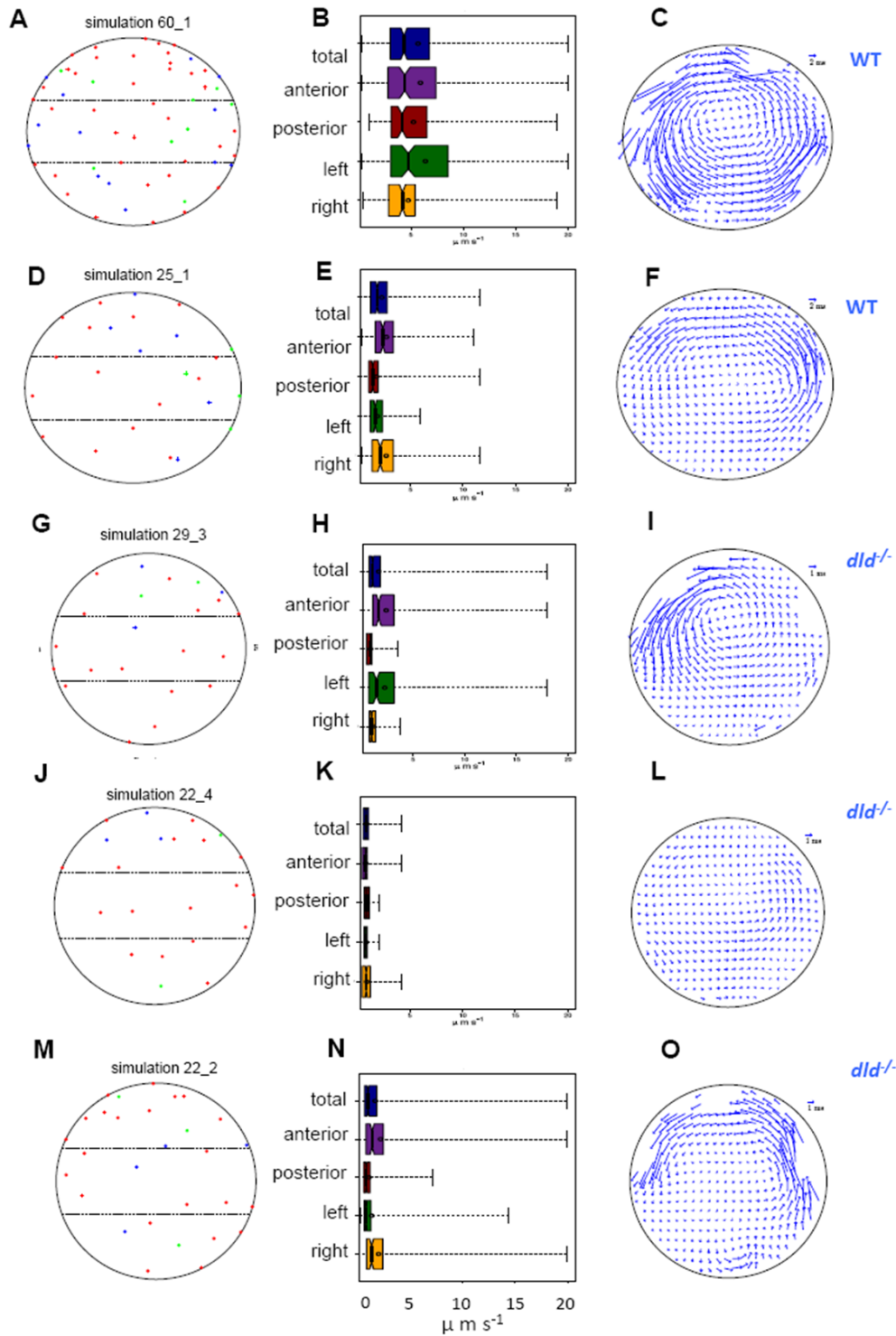


Figure 3.23 - *In silico* experiments. From individual cilium kinematics to cluster distribution and flow fields. These five simulations, among a total of forty (see Figure S2-3), were the ones that better matched the experimental data of Figure 3.18. (A, D, G, J, M) Seeding of different types of cilia in the KV mesh, filled dots represent cilia on the dorsal side and crosses label cilia on the ventral side of the KV, red represents motile cilia with single CBFs, green represents motile cilia with wobbling behaviors and blue represents immotile cilia. (B, E, H, K, N) Simulated flow speed in the different halves of the KV is plotted exactly in the same way as in Figure 3.18. (C, F, I, L, O) Flow forces produced by the simulated cilia are represented by vectors. Scale is $1 \mu\text{m s}^{-1}$.

Based on these findings our collaborators proposed a simplified statistical model relating cilia number to *situs*. For *deltaD*^{-/-} mutants, 8 out of 10 simulations with cilia number 29 or higher produced flow profiles exemplifying *situs solitus* (Figure S4 in Annex II). Taking an approximate threshold of 30 cilia, above which *situs solitus* is produced 100% of the time, and below which *situs solitus* is produced 50% of the time, we can use experimental data on the statistical distribution of cilium numbers in mutant and WT (Figure 3.20) to produce a rough estimate of the proportions of *situs solitus* embryos. For *deltaD*^{-/-}, approximately 80% of embryos have fewer than 30 cilia; the percentage of *situs solitus* via our model is then $80 \times 50\% + 20 \times 100\% = 60\%$. For WT, approximately 20% of embryos have fewer than 30 cilia; our model predicts $20 \times 50\% + 80 \times 100\% = 90\%$. These percentages closely match the embryo fates observed experimentally by Lopes *et al.* (2010). While this model is idealized and approximate, the close match to experimental observations suggest that in WT, cilia are produced in sufficient numbers to ensure the flow dominates random effects in the majority of cilia; we remark that our suggested threshold of 30 cilia corresponds to the modal value observed in WT embryos (Figure 3.19).

CHAPTER 4

Discussion

In this study we continued the characterization of the ciliary populations present in the Kupffer's vesicle (KV) following the work of a previous Master student in the lab, Rita Rua, who showed the existence of two motile cilia populations in the KV based on a Cilia Beat Frequency (CBF) spectral analysis using high-speed videomicroscopy. However, the video microscopy camera used in previous studies in our lab had a low resolution and the success rate in filming cilia per KV was very low. This led us to use a better resolution, faster acquisition camera (Photron MC2) which increased enormously the number of cilia filmed in each embryo, allowing us to map almost all cilia in the whole KV, something that we were not able to do before.

The improved analysis for cilia motility showed discrepancies from the previous cilia motility characterization done in the lab, which forced us to collect new embryos, re-film and re-analyze all cilia found in the KV. The new analysis confirmed the existence of the two motile cilia populations but the contribution of the wobbling cilia to the total population is much less than we previously thought. Importantly, the composition of the motile cilia population is actually very similar in WT and *deltaD*^{-/-} embryos.

By applying Fast Fourier Transform (FFT) we were able to unequivocally show that one population beats at a single frequency while a smaller population of motile cilia exhibit multiple beat frequency spectra peaks. Having identified this novel population of motile cilia we questioned if the secondary (lowest) frequency below the fundamental frequency could result from sub-harmonic components of the beating. After analyzing all the new movies with the better camera we found no evidence for the secondary frequencies following a 1/n ratio compared to the correspondent fundamental frequency. This fact allowed us to exclude that the secondary frequency could be a sub-harmonic of the fundamental frequency leading us to the most suited conclusion that these cilia are beating at two different frequencies simultaneously, which we named wobbling motion.

The discovery of cilia showing different motility patterns raised the question of whether these biophysically different populations are also molecularly and structurally different. In zebrafish it is commonly accepted that the KV has 9+2 motile cilia (Kreiling *et al.*, 2007; Kramer-Zucker, 2005; Supatto and Vermot, 2011; Sarmah *et al.* 2007) however, others have reported 9+0 and 9+2 types of cilia ultrastructure in the KV (Ferrante *et al.* 2009). So, there is some evidence that different cilia types exist in the zebrafish vertebrate L-R organizer as described for the mouse node (Caspary *et al.*, 2007).

It is our future goal to assign molecular markers to these different motility behaviors. One important aspect in zebrafish is the fact that while most of the epithelial tissues with motile cilia were reported to have a 9+2 structure (Kreiling *et al.*, 2007; Kramer-Zucker, 2005; Supatto and Vermot 2011; Sarmah *et al.*, 2007), not all of these cilia display a typical waveform motion. Supatto and Vermot (2011) recently revisited the types of spatially asymmetric beating patterns for motile cilia observed experimentally in zebrafish and described a 'corkscrew-like' motion in the kidney and a 'tilted conical' motion in the KV. We would like to add to these motility patterns the wobbling motion pattern we reported in our study as a subgroup of the tilted conical motion.

Although we do not know what makes a cilium to wobble it is likely to be related to its ultrastructure. Thus, the origin of this smaller population of motile cilia is object of our future research. Nevertheless, its impact in the flow dynamics was accounted for the mathematical modeling of the KV and may become important as cilia number increases.

Other studies (Kramer-Zucker, 2005; Okabe *et al.*, 2008; Supatto and Vermot, 2011; Jaffe *et al.*, 2010; Supatto *et al.*, 2008) have shown zebrafish KV CBF results obtained by averaging a few random cilia (usually from 3-4 embryos). In contrast, our CBF data was generated by analyzing as much as 80 cilia in a total of 16 embryos for WT and 26 embryos for $\Delta\Delta$ embryos. Our reported CBF values showed to be within the range described in these previous studies, but our spectral analysis brought innovation to the study of the vertebrate organizer allowing us to identify two different types of motile cilia based on CBF distinct patterns.

While characterizing WT and $\Delta\Delta$ cilia populations we noticed that, generally, the number of cilia found in the mutants was less than in the WT embryos. This, in addition to the shorter cilia found in $\Delta\Delta$, that was previously reported (Lopes *et al.*, 2010), let us wonder how would the KV fluid flow behave under these conditions.

From fluid flow measurements we observed that $\Delta\Delta$ mutants could have a range of fluid flow velocities for different embryos (Figure 3.18 E, H, K), which could be explained by the combination of a relatively broad distribution of cilia length and number found for the mutants. Considering this and knowing that $\Delta\Delta$ mutant embryos were previously reported to have heterotaxia defects we thought it was worth to explore how the variation of flow behaviors seen along the different mutants could correlate with organ *situs*.

So, by using $\Delta\Delta$ homozygous mutants and *dnah7* morphants we evaluated the contributions of different motile cilia numbers to KV fluid flow patterns. Subsequently, we correlated these flow patterns with respective organ *situs*. For this purpose we manipulated the cilia number and length, using $\Delta\Delta$ mutants and abolished cilia motility using *dnah7* morphants. As predicted, we observed a dispersion of fluid flow velocities as the main parameter affected. Most importantly, our results showed a link between specific local flow dynamics and internal organ laterality, which raised the long-standing question of whether the action of nodal flow is to generate mechanical stress or to transport an unknown determinant morphogen. Our observation that a weak flow, generated by as few as two motile cilia, is sufficient to break L-R symmetry favors the mechanical force model. In terms of hydrodynamics on the microscopic scale, the slower flow observed in some $\Delta\Delta$ embryos (Figure 3.18 H, I) is still capable of transporting particles along the KV. However, the flow generated by two motile cilia is extremely local (Figure 3.18 N, O), and under conditions with a low Reynolds number, when viscosity dominates and inertia is negligible (Smith *et al.*, 2012), the flow would be attenuated over distance from the motile cilia. This means that would take a relative long time for a particle to travel from one side of the node to the other side. Alternatively, a local mechanical force generated by such flow may be sufficient to stimulate the surrounding cells and therefore break the L-R asymmetry.

To sense local flow implies that some sort of sensory mechanism must be in place in the KV. We know that *pkd2*, a gene encoding a Ca²⁺ channel involved in mechanosensory responses in the kidney (Nauli *et al.*, 2003), is expressed in the zebrafish KV cells and that *cup/pkd2*^{-/-} null mutants have left-right defects (Bisgrove *et al.*, 2005; Schottenfeld *et al.*, 2007). These observations, together with the report that Pkd111-Pkd2 complexes are present in all motile cilia of medaka fish (Kamura *et al.*, 2011), suggest that all KV cilia, irrespective of their motile capabilities, may be competent to respond to hydrodynamic forces. On the other hand, our results show for the first time that there is a significant number of immotile cilia in the zebrafish KV which may disclose a sensory role, as described for the crown cell cilia of the mouse node. Nevertheless, this mechanosensory hypothesis would require a mechanism that expands the signal received by the few stimulated KV cells to the cells in the lateral plate mesoderm. Our results suggest that zebrafish KV has a highly sensitive system that is able to detect an extremely weak signal generated by a localized flow. Whereas in mouse studies the methods used are highly invasive and allow only to score LPM markers to infer about the final position of the organs, our work in zebrafish had the great advantage that we could correlate local fluid flow using non-invasive methods with organ position after the embryos were filmed. Ultimately, this allowed us to create a testable model that can predict organ *situs* by evaluating KV flow dynamics.

The existence of mutants where heterotaxia occurs without notochord defects, such as in *deltaD*^{-/-} mutants (Lopes *et al.*, 2010), lead us to envisage the existence of a specific and complex mechanism that decouples heart from liver *situs*. Considering this issue we think it would be very important and informative to study an intermediate step of development between flow patterns and organ position to be able to understand the full course of development events that lead to heart and liver patterning in a heterotaxic embryo.

Nodal and Nodal-related factors play fundamental roles in a number of developmental processes, including mesoderm and endoderm formation, patterning of the anterior neural plate, and determination of bilateral asymmetry in vertebrates. The *Nodal*-related gene southspaw (*spaw*) is the earliest molecule to be asymmetrically detected in the left lateral plate mesoderm (LPM) and is known to induce the expression of the transcription factor *pitx2* (Hamada *et al.*, 2002; Long *et al.*, 2003), a paired-like homeobox gene, that has been reported to be required early in the Nodal signaling pathway for specification of the endodermal and mesodermal germ layers. The Nodal antagonist, Charon, on the other hand, is expressed asymmetrically on the right side of the KV from the 8th to 12th somite stage in a fluid flow-dependent manner (Lopes *et al.*, 2010). In mouse, it has been shown that the asymmetric signals that are induced by flow are first apparent in the peripheral crown cells. Yoshida *et al.* (2012) demonstrated that *Nodal* antagonist, *Cerl2* (*Charon*), is a target of flow-induced Pkd2-mediated signals, suggesting that nodal leftward flow is capable of activating Pkd2 channels within crown cell cilia, which in turn inhibits expression of *Cerl2*.

Hashimoto *et al.* (2004) studying medaka fish also supported this idea when suggesting that an asymmetric Charon function inhibits the expression of *spaw* on the right LPM. **spaw** /nodal is required for establishment of laterality and disturbance in its expression pattern is correlated with

defects in organ placement in zebrafish and other organisms (Long *et al.*, 2003). However the relationship between *spaw* abnormal expression and organ situs is not known in the same embryos.

The way *spaw* expression is thought to occur has been addressed previously and it was reported that *spaw* expression begins at the posterior end of the left LPM at the 10-somite stage, newly synthesized Spaw in the LPM further stimulates the progressive, posterior-to-anterior expression of *spaw* and its target genes in the left LPM at a rate of 2.3 somite lengths per somite generation time (Long *et al.*, 2003; Wang and Yost, 2008). This suggests that this progression depends on the positive feedback loop of Spaw. So, if this mechanism is deregulated due to lack of flow stimulation on left sided KV cells, it is possible that newly synthesized *spaw* may be compromised, leading to its degradation from posterior to anterior LPM. This would in turn result in absent expression of Spaw target-genes which are important for correct organ positioning.

Our results showed that in *deltaD*^{-/-} heterotaxic embryos displaying central and right liver *situs* there is still some localized flow movement on the left half of the KV (Figure 3.18 H, K). This is particularly visible in the corresponding heat maps (Figure 3.18 I, L) where peaks of relatively fast flow (20 $\mu\text{m s}^{-1}$) are also present on the left side. Therefore we can hypothesize that such flow could originate enough left *spaw* expression to then reach the heart precursor field and generate a normal heart on the left side, but this same flow may be insufficient to trigger a correct response for normal liver positioning. Meaning that to achieve a correct gut looping, a faster fluid flow may be required.

This simple line of thought would predict that in WT zebrafish the percentage of gut asymmetries is higher than the one for heart asymmetries. In fact our results showed us that among the embryos with *situs* defects, the gut position was most often affected rather than the heart which supports our hypothesis.

In order to better understand the impact of localized KV fluid flow on crucial steps for L-R patterning, we think it is worth to characterize the asymmetric information in the LPM by using the left-identity molecular markers *spaw* or *pitx2* in *deltaD*^{-/-} and *dnah7* morphants. Ideally, to be really informative about the cascade of events in L-R patterning we ought to measure KV flow, have a LPM reporter and score organ situs in the same embryo. Such procedure would require either a *spaw*:eGFP or a *pitx2*:eGFP reporter line to score LPM laterality, and later label liver position by *in situ* hybridization using *foxA3*, a transcriptional activator for liver-specific genes. In our lab we aim to achieve this level of evaluation per embryo in the near future.

As we observed WT zebrafish embryos display both heart and liver on the left side of the midline. We propose that there might be a common signal for left, starting at the KV left side by repeated fluid flow stimulation over 3-4 hours (from 12 hpf). Our hypothesis is supported by others' observations (Ober *et al.*, 2003) and by a time course experiment performed recently in our lab that shows both asymmetric heart field position and gut tube looping start on the left side of the body early in development. Markers, such as *lefty2* start to label the heart field on the left side of the embryo at around 18 hpf and *foxA3* labels the first gut looping to the left at 24 hpf. This experiment showed us that heart and gut declare left sidedness between 18 and 23 hpf which means within a five hour time

window. However, the fact that heart and liver position does not always concur in case of *situs* defect, observed in *deltaD*^{-/-} mutants and *dnah7* morphant embryos may indicate that heart and liver patterning may be uncoupled. It is possible that in a situation in which KV fluid flow is impaired, left sided KV cells are not sufficiently stimulated to promote the propagation of the signal responsible for the formation of these two organs. In this case the produced signal would be strong enough for heart formation, but become disrupted during the time window before the formation of the gut. This could explain the origin of liver patterning defects with a correct heart positioning.

We developed a tool to disrupt cilia motility by using novel *dnah7* knockdown experiments, however the mechanism by which the lack of an inner dynein is capable of such severe cilia paralysis defect is yet to be understood. Effective motility of cilia requires precise control of beat frequency and waveform, through regulation of the outer dynein arms and inner dynein arms, respectively. These dynein arms are multisubunit protein complexes with ATPase activity that promote sliding between adjacent microtubules, and their coordinated activation and inactivation generates a ciliary wave.

The regulatory mechanisms are thought to involve structural and chemical signals that begin in the central pair apparatus and are then transmitted to the outer doublet microtubules by the radial spokes (Smith and Yang, 2004). Recently Yamamoto *et al.* (2013) identified the MIA (modifier of inner arms) complex within the *Chlamydomonas reinhardtii* axoneme that physically links to the nexin-dynein regulatory complex (N-DRC) and provides a signaling conduit from the radial spokes to an inner arm dynein (I1 dynein) essential for waveform determination. In axonemes from mutants that lack both the outer dynein arms and the MIA complex, I1 dynein failed to assemble, suggesting physical interactions between these three axonemal complexes. The MIA complex appears to regulate inner arm dyneins and possibly outer arm dyneins, which are both essential for normal motility. Furthermore defective assembly of this inner dynein showed slower ciliary beat frequencies and microtubule sliding velocities, which suggests a possible functional interaction between inner dynein arms and outer dynein arms which control ciliary beat frequency.

Phylogenetic analysis revealed that potential orthologues of *C. reinhardtii* MIA complex components are also present in vertebrates and so it is expected that a similar system may be present zebrafish KV motile cilia. We can speculate that in our *dnah7* morphants the stability of the complex may be compromised when the inner dynein is lacking leading to cilia paralysis. Moreover recent studies in PCD human patients report cases where the isolated absence of inner dynein arms can cause static, immotile respiratory tract cilia (Shoemark *et al.*, 2013), which support the phenotype that we describe in *dnah7* morphants.

Dysfunctional ciliary movement due to inner arms dynein defects can lead to primary ciliary dyskinesia, which may be responsible for recurrent respiratory infections, infertility, and hydrocephalus (Fliegauf *et al.*, 2007; Afzelius, 2004; Ibañez-Tallon *et al.*, 2003). As the expression pattern for *dnah7* showed it is expressed in several ciliated organs (Figures 3.10 - 3.12) we aim to better characterize this gene knockdown to search further cilia dismotility associated organ defects.

One interesting and unexpected result was the expression pattern of *dnah7* seen in the zebrafish embryonic heart (Figure 3.12). Primary 9+0 cilia have been found many years ago in embryonic and adult human heart (Myklebust *et al.*, 1977), mouse and chicken (Slough *et al.*, 2008; Van der Heiden *et al.*, 2006) however motility function has never been associated to cardiac cilia.

Normal cardiac development depends on complex interplay between genetic and epigenetic factors. Signaling pathways such as Wnt/ β -catenin and Hedgehog signaling, and cell behaviors such as epithelial-mesenchymal transformation (EMT) and neural crest cell migration are all essential in specifying heart morphogenesis (Dunwoodie, 2007). A unique feature of heart development is that the heart must function as a pump both to support the remainder of the developing organism, and to drive its own normal morphogenesis. So if flow participates in driving the development of form in the developing heart (and vasculature) there must be a mechanism for the heart to sense and respond to fluid flow. The primary cilia lining cardiac cells assumed the role of sensing this fluid flow and these have been suggested to be required in cardiac development independently from node cilia function in L-R development. A possible function of these cardiac cilia may be therefore a mechanosensory one, integrating flow, cardiac function and morphogenesis.

In search for heart defects in our *dnah7* morphant embryos we found that the cardiac rhythm was slower than WT (30 hpf). So we could hypothesize that initial fluid flow sensed in the heart, at around 18 hpf, could be produced by motile cilia for early heart morphogenesis and that impaired flow at this stage could result in further cardiac defects.

Although we did not yet confirm the presence of motile cilia in the heart a recent work in our lab showed that *Foxj1a*, a transcription factor that regulates motile cilia function, is also present in cardiac cells of the zebrafish. This evidence allied to the *dnah7* expression in this region suggests that motile cilia may effectively be present in the heart. So if cardiac development is dependent of flow in early stages of development, this could indicate the function of motile cilia is needed in addition to cardiac muscle movement. Therefore in the future it would be very interesting to find and film motile cilia in zebrafish embryonic heart and dissect its function.

In collaboration with a group of mathematicians led by Dr. David Smith (University of Birmingham), we have improved the KV fluid-flow model based on their previous version (Smith *et al.* 2012) using experimental data collected for KV volume, CBF, cilia number and cilia length. Our simulations were based purely on observational data and the physics of microscale flow, with no adjustable parameters or fitting employed. The real system is highly complex, and simulation cannot at present capture all of the details of the interior geometry, cilia structure and dynein regulation, however our results show excellent qualitative and good quantitative correspondence between simulated (Figure 3.23) and measured (Figure 3.18) particle velocity distributions, suggesting that the most important features of viscous fluid dynamics, KV geometry and cilia activity have been captured by the model. The formulation of the model can be viewed as a 'blueprint' for the KV architecture.

Dorsal anterior clustering of monociliated KV cells has been described by several authors (Kreiling *et al.*, 2007; Okabe *et al.*, 2008; Supatto *et al.*, 2008) and is also reported here in this work. More recently, Wang *et al.* (2012) showed that this clustering occurs during development due to a KV

cell shape remodeling involving the Rock2b-MyosinII pathway. Here we confirm through flow simulations, that even in WT embryos, when this dorsal anterior cluster of ciliated cells is disturbed (Figure S3 in Annex), the flow forces produced anteriorly become lower and different patterns of 'abnormal' flow may arise (Figure 3.23 F).

In this work we used a combination of diverse imaging, genetic and computational techniques in an arduous mission to understand some of the mechanisms that underlie left-right asymmetry determination. Ultimately, we propose a model that can simply explain the biological significance of KV flow for organ formation and patterning in zebrafish. In a normal *situs solitus* situation, the presence of anterior dorsal KV ciliated cells is crucial to originate a directional strong flow that will stimulate left-sided KV cells. In contrast, when disruption of this cluster of anterior cilia occurs, *situs* abnormalities may arise. Subsequent stronger right flow can stimulate right-sided cells originating *situs inversus*. In turn, heterotaxia may happen in a particular case where impaired fluid flow favors weak cell stimulation in one of KV sides causing gut misplacement alone. Finally, we predict *situs ambiguous* situations may occur when no biased flow signals are present and KV cells are not stimulated, giving rise to a lack of laterality and forming centralized organs. In a near future study we pretend to address these questions by making use of more accurate visualization techniques available to date (Corkidi *et al.*, 2008) for a fast 3D+t reconstruction of the entire functional KV. This would allow not only to fully characterize the complex dynamics of the fluid flow in the KV but also to quantitate the 3D features of the cilia (length, beating frequency, orientation, curvature, torque), which in turn would greatly improve the current algorithms for explaining cilia-mediated hydrodynamics. This setup would improve even more with the usage of zebrafish transgenic lines with genetically encoded calcium indicator (GCaMP) (Muto *et al.*, 2011) under the control of the transcription factor *sox17* that is expressed in KV cells. This would help to understand in 3D and in real-time the real contribution of the fluid flow to KV cell stimulation.

References

- Afzelius, B.A., 1976. A human syndrome caused by immotile cilia. *Science*, 193, 317–319.
- Afzelius, B.A., 2004. Cilia-related diseases. *The Journal of Pathology* 204, 470–477.
- Amack, J.D., Wang, X. and Yost, H.J., 2007. Two T-box genes play independent and cooperative roles to regulate morphogenesis of ciliated Kupffer's vesicle in zebrafish. *Developmental Biology*, 310(2), 196–210.
- Armengot, M., Bonet, M., Carda C., *et al.*, 2012. Development and Validation of a Method of Cilia Motility Analysis for the Early Diagnosis of Primary Ciliary Dyskinesia. *Acta Otorrinolaringologica (English Edition)*, 63(1), 1–8.
- Babu, D. and Roy, S., 2013. Left–right asymmetry: cilia stir up new surprises in the node. *Open Biology*, 3, 130052.
- Badano, J.L., Mitsuma, N., Beales, P.L., and Katsanis, N., 2006. The ciliopathies: an emerging class of human genetic disorders. *Annual review of genomics and human genetics*, 7, 125–48.
- Bellomo, D., Lander, A., Harragan, I. and Brown, N.A., 1996. Cell proliferation in mammalian gastrulation: the ventral node and notochord are relatively quiescent. *Development Dynamics*, 205, 471–485.
- Bill, B.R., Petzold, A.M., Clark, K.J., *et al.*, 2009. A primer for morpholino use in zebrafish. *Zebrafish*, 6(1), 69-77.
- Bisgrove, B.W., Snarr, B.S., Emrazian, A. and Yost, H.J., 2005. Polaris and Polycystin-2 in dorsal forerunner cells and Kupffer's vesicle are required for specification of the zebrafish left-right axis. *Development Biology*, 287, 274-288.
- Borovina, A., Superina, S., Voskas, D. and Ciruna, B., 2010. Vangl2 directs the posterior tilting and asymmetric localization of motile primary cilia. *Nature Publishing Group*, 12(4), 407–412.
- Brennan, J., Norris, D. and Robertson, E., 2002. Nodal activity in the node governs left-right asymmetry. *Genes & development*, 16(18), 2339–2344.
- Brokaw, C.J. and Kamiya, R., 1987. Bending patterns of Chlamydomonas flagella: IV. Mutants with defects in inner and outer dynein arms indicate differences in dynein arm function. *Cell Motility and the Cytoskeleton* 8, 68–75.
- Buceta, J., Ibanes, M., Rasskin-Gutman, D., *et al.*, 2005. Nodal cilia dynamics and the specification of the left/right axis in early vertebrate embryo development. *Biophysical Journal*, 89, 2199–2209.
- Bush, A., Chodhari, R., Collins, N., *et al.*, 2007. Primary ciliary dyskinesia: current state of the art. *Archives of Disease in Childhood*, 92, 1136–1140.

- Carda, C., Armengot, M., Escribano, A. and Peydró, A., 2005. Ultrastructural patterns of primary ciliary dyskinesia syndrome. *Ultrastructural Pathology*, 29: 3-8.
- Cartwright, J.H., Piro, N., Piro, O. and Tuval, I., 2006. Embryonic nodal flow and the dynamics of nodal vesicular parcels. *Journal of The Royal Society Interface*, 4(12), 49–55.
- Cartwright, J.H.E., Piro, O. and Tuval, I., 2009. Fluid dynamics in developmental biology: moving fluids that shape ontogeny. *HFSP Journal*, 1–17.
- Caspary, T., Larkins, C.E. and Anderson, K.V., 2007. The graded response to Sonic Hedgehog depends on cilia architecture. *Developmental Cell*, 12(5), 767–778.
- Castleman, V.H., Romio, L., Chodhari, R., *et al.*, 2009. Mutations in radial spoke head protein genes RSPH9 and RSPH4A cause primary ciliary dyskinesia with central-microtubular-pair abnormalities. *American journal of human genetics*, 84(2), 197–209.
- Chilvers, M.A., Rutman, A. and O'Callaghan, C., 2003. Ciliary beat pattern is associated with specific ultrastructural defects in primary ciliary dyskinesia. *The Journal of Allergy and Clinical Immunology*, 112: 518-524.
- Chung, W.S., and Stainier, D.Y.R., 2008. Intra-endodermal interactions are required for pancreatic beta cell induction. *Developmental Cell*, 14, 582–593.
- Colantonio, J.R., Vermot, J., Wu, D., *et al.*, 2009. The dynein regulatory complex is required for ciliary motility and otolith biogenesis in the inner ear. *Nature*, 457(7226), 205–209.
- Collignon, J., Varlet, I. and Robertson, E.J. 1996. Relationship between asymmetric nodal expression and the direction of embryonic turning. *Nature*, 381, 155–158.
- Cortez, R., 2001. The method of regularized Stokeslets. *SIAM Journal on Scientific Computing*, 23(4), 1204–1225.
- Cortez, R., Fauci, L., and Medovikov, A., 2005. The method of regularized Stokeslets in three dimensions: analysis, validation, and application to helical swimming. *Physics of Fluids*, 17, 1–14.
- Dunwoodie, S.L., 2007. Combinatorial signaling in the heart orchestrates cardiac induction, lineage specification and chamber formation. *Seminars in Cell & Developmental Biology*, 18, 54–66.
- Eisen, J.S. and Smith, J.C., 2008. Controlling morpholino experiments: don't stop making antisense. *Development*, 135(10), 1735-43.
- Essner, J.J., Amack, J.D., Nyholm, M.K., *et al.*, 2005. Kupffer's vesicle is a ciliated organ of asymmetry in the zebrafish embryo that initiates left-right development of the brain, heart and gut. *Development*, 132, 1247–1260.
- Ferrante, M.I., Romio, L., Castro, S., *et al.*, 2009. Convergent extension movements and ciliary function are mediated by *ofd1*, a zebrafish orthologue of the human oral-facial-digital type 1 syndrome gene. *Human Molecular Genetics*, 18(2), 289–303.

- Fliegauf, M., Benzing, T. and Omran, H., 2007. When cilia go bad: cilia defects and ciliopathies. *Nature reviews. Molecular cell biology*, 8(11), pp.880–93.
- Field, S., Riley, K.L., Grimes, D.T., *et al.*, 2011. Pkd111 establishes left–right asymmetry and physically interacts with Pkd2. *Development*, 138, 1131–1142.
- Fowkes, M.E. and Mitchell, D.R., 1998. The role of preassembled cytoplasmic complexes in assembly of flagellar dynein subunits. *Molecular Biology of the Cell*, 9, 2337–2347.
- Francescato, L., Rothschild, S.C., Myers, A.L., and Tombes, R.M., 2010. The activation of membrane targeted CaMK-II in the zebrafish Kupffer's vesicle is required for left-right asymmetry. *Development*, 137, 2753–2762.
- Freund, J.B., Goetz, J.G., Hill, K.L. and Vermot, J., 2012. Fluid flows and forces in development: functions, features and biophysical principles. *Development*, 139(7), 1229–1245.
- Gibbons, I., 1981. Cilia and flagella of eukaryotes. *The Journal of cell biology*, 91, 107–124.
- Goetz, S.C.S. and Anderson, K.V.K., 2010. The primary cilium: a signalling centre during vertebrate development. *Audio, Transactions of the IRE Professional Group on*, 11(5), 331–344.
- Goodenough, U.W. and Heuser, J.E., 1985. Outer and inner dynein arms of cilia and flagella. *Cell* 41, 341–342.
- Hamada, H., 2002. Establishment of vertebrate left-right asymmetry. *Nature Reviews Genetics*, 3, 103–113.
- Hashimoto, H., Rebagliati, M., Ahmad, N., *et al.*, 2004. The Cerberus/Dan-family protein Charon is a negative regulator of Nodal signaling during left-right patterning in zebrafish. *Development*, 131, 1741-1753
- Hayes, J., Kim, S. and Abitua, P., 2007. Identification of novel ciliogenesis factors using a new in vivo model for mucociliary epithelial development. *Developmental Biology*, 312(1), 115–130.
- Heuser, T., Raytchev, M., Krell, J., *et al.*, 2009. The dynein regulatory complex is the nexin link and a major regulatory node in cilia and flagella. *The Journal of Cell Biology* 187, 921–933.
- Heuser, T., Dymek, E.E., Lin, J., *et al.*, 2012. The CSC connects three major axonemal complexes involved in dynein regulation. *Molecular Biology of the Cell*. 23, 3143–3155.
- Hildebrandt, F., Benzing, T. and Katsanis, N., 2011. Ciliopathies. *New England Journal of Medicine*, 364(16), pp.1533–1543.
- Ibañez-Tallon, I., 2003. To beat or not to beat: roles of cilia in development and disease. *Human Molecular Genetics*, 12, 27–35.
- Ishikawa, H. and Marshall, W.F., 2011. Ciliogenesis: building the cell's antenna. *Nature Reviews Molecular Cell Biology*, 12, 222–234.
- Jaffe, K.M., Thiberge, S.Y., Bisher, M.E. and Burdine, R.D., 2010. Imaging Cilia in Zebrafish. *Methods in Cell Biology*, 97, 415-435.

- Kamiya, R., 2002. Functional diversity of axonemal dyneins as studied in *Chlamydomonas* mutants. *International Review of Cytology*, 219, 115–155.
- Kamiya, R., Kurimoto, E. and Muto, E., 1991. Two types of *Chlamydomonas* flagellar mutants missing different components of inner-arm dynein. *The Journal of Cell Biology*, 112, 441–447.
- Kamura, K., Kobayashi, D., Uehara, Y., *et al.*, 2011. Pkd111 complexes with Pkd2 on motile cilia and functions to establish the left-right axis. *Development*, 138(6), 1121–1129.
- Karlsson, J., von Hosten, J. and Olsson, P.E., 2001. Generating transparent zebrafish: a refined method to improve detection of gene expression during embryonic development. *Marine Biotechnology (New York)*, 3(6), 522-7.
- Kimmel, C., Ballard, W., Kimmel, S., *et al.*, 1995. Stages of Embryonic Development of the Zebrafish. *Developmental Dynamics*, 253–310.
- King, S.M., and Kamiya, R., 2009. Axonemal dyneins: assembly, structure, and force generation. In *The Chlamydomonas Sourcebook: Cell Motility and Behavior*. Second Edition. Vol. 3. G.B. Witman, editor. Academic Press, San Diego, CA. pp. 131–208.
- Kobayashi, D. and Takeda, H., 2012. Ciliary motility: the components and cytoplasmic preassembly mechanisms of the axonemal dyneins. *Differentiation; research in biological diversity*, 83(2), 23–9.
- Kramer-Zucker, A., Olale, F., Haycraft, C., *et al.*, 2005. Cilia-driven fluid flow in the zebrafish pronephros, brain and Kupffer's vesicle is required for normal organogenesis. *Development*, 132, 1907–1921.
- Kreiling, J.A., Prabhat, Williams, G. and Creton, R., 2007. Analysis of Kupffer's vesicle in zebrafish embryos using a cave automated virtual environment. *Developmental Dynamics*, 236(7), 1963–1969.
- Lehtreck, K.F., Delmotte, P., Robinson, M.L., *et al.*, 2008. Mutations in *Hydin* impair ciliary motility in mice. *Journal of Cell Biology*, 180, 633–643.
- Levin, M., Johnson, R.L., Stern, C.D., *et al.*, 1995. A molecular pathway determining left-right asymmetry in chick embryogenesis. *Cell*, 82: 803–814.
- Lieschke, G.J. and Currie, P.D., 2007. Animal models of human disease: zebrafish swim into view. *Nature Reviews Genetics*. 8, 353–367.
- Lopes, S.S., Lourenço, R., Pacheco, L., *et al.*, 2010. Notch signalling regulates left-right asymmetry through ciliary length control. *Development*, 137, 3625–3632.
- McGrath, J., Somlo, S., Makova, S., *et al.*, 2003. Two populations of node monocilia initiate left-right asymmetry in the mouse. *Cell*, 114, 61-73.
- Meno, C., Saijoh, Y., Fujii, H., *et al.*, 1996. Left-right asymmetric gene expression of the TGF β -family member *lefty* in mouse embryos. *Nature*, 381: 151–155.

- Mitchell, D., 2007. The evolution of eukaryotic cilia and flagella as motile and sensory organelles. *Eukaryotic Membranes and Cytoskeleton*, 130–140.
- Muto, A., Ohkura, M., Kotonay, T., *et al.*, 2011. Genetic visualization with an improved GCaMP calcium indicator reveals spatiotemporal activation of the spinal motor neurons in zebrafish. *Proceedings of the National Academy of Sciences of the United States of America*, 108(13), 5425–30.
- Myklebust, R., Engedal, H., Saetersdal, T.S. and Ulstein, M., 1977. Primary 9+0 cilia in the embryonic and the adult human heart. *Anatomy and Embryology*. 151, 127–39.
- Nauli, S. M., Alenghat, F. J., Luo, Y., *et al.*, 2003. Polycystins 1 and 2 mediate mechanosensation in the primary cilium of kidney cells. *Nature Genetics*, 33, 129- 137.
- Nonaka, S., Yoshida, S., Watanabe, D., *et al.*, 2005. De novo formation of left-right asymmetry by posterior tilt of nodal cilia. *PLoS Biology*, 3(8), e268–e268.
- Nonaka, S., Shiratori, H., Saijoh, Y. and Hamada, H., 2002. Determination of left-right patterning of the mouse embryo by artificial nodal flow. *Nature*, 418(6893), 96–99.
- Nonaka, S., Tanaka, Y., Okada, Y., *et al.*, 1998. Randomization of left-right asymmetry due to loss of nodal cilia generating leftward flow of extraembryonic fluid in mice lacking KIF3B motor protein. *Cell*, 95(6), 829–837.
- Ober, E.A., Field, H.A., and Stainier, D., 2003. From endoderm formation to liver and pancreas development in zebrafish. *Mechanisms of Development*. 120(1), 5-18.
- Okabe, N., Xu, B. and Burdine, R.D., 2008. Fluid dynamics in zebrafish Kupffer's vesicle. *Developmental Dynamics*, 237(12), 3602–3612.
- Okada, Y., Nonaka, S., Tanaka, Y., *et al.*, 1999. Abnormal nodal flow precedes situs inversus in iv and inv mice. *Molecular Cell*, 4, 459-468.
- Okada, Y., Takeda, S., Tanaka, Y., *et al.*, 2005. Mechanism of nodal flow: a conserved symmetry breaking event in left-right axis determination. *Cell*, 121(4), 633–644.
- Olbrich, H., Schmidts, M., Werner, C., *et al.*, 2012. Recessive HYDIN mutations cause primary ciliary dyskinesia without randomization of left–right body asymmetry. *American Journal of Human Genetics*, 91, 672–684.
- Olm, M.A., Kögler, J.E., Machione, M., *et al.*, 2011. Primary ciliary dyskinesia: evaluation using cilia beat frequency assessment via spectral analysis of digital microscopy images. *Journal of Applied Physiology*, 111(1), 295–302.
- Papon, J.F., Coste, A., Roudot-Thoraval, F., *et al.*, 2010. A 20-year experience of electron microscopy in the diagnosis of primary ciliary dyskinesia. *The European Respiratory Journal*, 35, 1057–1063.

- Parichy, D.M., Elizondo, M.R., Mills, M.G., *et al.*, 2009. Normal table of postembryonic zebrafish development: Staging by externally visible anatomy of the living fish. *Development Dynamics*, 238, 2975-3015.
- Patel, A., and Honoré, E., 2010. Polycystins and renovascular mechanosensory transduction. *Nature Reviews Nephrology*, 6, 530–538.
- Pennarun, G., Escudier, E., Chapelin, C., 1999. Loss-of-function mutations in a human gene related to *Chlamydomonas reinhardtii* dynein IC78 result in primary ciliary dyskinesia. *American Journal of Human Genetics*, 65: 1508–1519.
- Pennekamp P., Karcher, C., Fischer, A., *et al.*, 2002. The ion channel Polycystin-2 is required for left-right axis determination in mice. *Current Biology*, 12, 938–943.
- Piperno, G., Mead, K. and Shestak, W., 1992. The inner dynein arms I2 interact with a “dynein regulatory complex” in *Chlamydomonas flagella*. *The Journal of Cell Biology*, 118, 1455–1463.
- Porter, M.E. and Sale, W.S., 2000. The 9 + 2 axoneme anchors multiple inner arm dyneins and a network of kinases and phosphatases that control motility. *Journal Cell Biology*, 151(5), 37–42.
- Rosen, J.N., Sweeney, M.F. and Mably, J.D., 2009. Microinjection of zebrafish embryos to analyze gene function. *Journal of visualized experiments*, 9(25), pii:1115.
- Sarmah, B., Winfrey, V. P., Olson, G. E., *et al.*, 2007. A role for the inositol kinase Ipk1 in ciliary beating and length maintenance. *Proceedings of the National Academy of Sciences of the United States of America*, 104, 19843–19848.
- Satir, P., Pedersen, L.B. and Christensen, S.T., 2010. The primary cilium at a glance. *Journal of Cell Science*, 123, 499–503.
- Shoemark, A., 2013. Inner Dynein Arm Defects in Primary Ciliary Dyskinesia. *Journal of Genetic Syndromes & Gene Therapy*, 4(7).
- Schottenfeld, J., Sullivan-Brown, J. and Burdine, R.D., 2007. Zebrafish curly up encodes Pkd2 ortholog that restricts left-side-specific expression of southspaw. *Development*, 134(8), 1605-15.
- Schweickert, A., Weber, T., Beyer, T., *et al.*, 2007. Cilia-driven leftward flow determines laterality in *Xenopus*. *Current Biology*, 17(1), 60–66.
- Silflow, C. and Lefebvre, P., 2001. Assembly and motility of eukaryotic cilia and flagella. Lessons from *Chlamydomonas reinhardtii*. *Plant physiology*, 127, 1500–1507.
- Singla, V. and Reiter, J.F., 2006 The primary cilium as the cell's antenna: signaling at a sensory organelle. *Science*, 313, 629–633.
- Slough, J., Cooney, L. and Brueckner, M., 2008. Monocilia in the embryonic mouse heart suggest a direct role for cilia in cardiac morphogenesis. *Development Dynamics*, 237, 2304-2314.
- Smith, A.A., Johnson, T.D, Smith, D.J. and Blake, J.R., 2012. Symmetry breaking cilia-driven flow in the zebrafish embryo. *Journal of Fluid Mechanics*, 705, 26–45.

- Smith, D.J., Blake, J.R. and Gaffney, E.A., 2008. Fluid mechanics of nodal flow due to embryonic primary cilia. *Journal of the Royal Society Interface*, 5(22), 567–573.
- Smith, D.J., Smith, A.A. and Blake, J.R., 2010. Mathematical embryology: the fluid mechanics of nodal cilia. *Journal of Engineering Mathematics*, 70(1-3), 255–279.
- Smith, E.F. and Yang, P., 2004. The radial spokes and central apparatus: mechano-chemical transducers that regulate flagellar motility. *Cell Motility and the Cytoskeleton*.57, 8–17.
- Supatto, W., Fraser, S.E., and Vermot, J., 2008. An all-optical approach for probing microscopic flows in living embryos. *Biophysical Journal*, 95, 29–31.
- Supatto, W. and Vermot, J., 2011. *From cilia hydrodynamics to zebrafish embryonic development*. 1st ed., Elsevier Inc.
- Supp, D., Brueckner, M., Kuehn, M., *et al.*, 1999. Targeted deletion of the ATP binding domain of left-right dynein confirms its role in specifying development of left-right asymmetries. *Development*, 126, 5495–5504.
- Supp, D., Witte, D., Potter, S., and Brueckner, M., 1997. Mutation of an axonemal dynein affects left-right asymmetry in *inversus viscerum* mice. *Nature* 389, 963–966.
- Takeda, S., Yonekawa, Y., Tanaka, Y., *et al.*, 1999. Left-right asymmetry and kinesin superfamily protein KIF3A: new insights in determination of laterality and mesoderm induction by *kif3A*^{-/-} mice analysis. *Journal Cell Biology*. 145, 825-836.
- Tanaka, Y., Okada, Y., and Hirokawa, N., 2005. FGF-induced vesicular release of Sonic hedgehog and retinoic acid in leftward nodal flow is critical for left-right determination. *Nature*, 435, 172–177.
- Thisse, C. and Thisse, B., 2008. High-resolution in situ hybridization to whole-mount zebrafish embryos. *Nature Protocols*, 3(1), 59–69.
- Van der Heiden, K., Groenendijk, B.C., Hierck, B.P., *et al.*, 2006. Monocilia on chicken embryonic endocardium in low shear stress areas. *Developmental Dynamics*, 235, 19-28.
- Vermot, J., Llamas, J.G., Fraulob, V., *et al.*, 2005. Retinoic acid controls the bilateral symmetry of somite formation in the mouse embryo. *Science*, 308, 563–566.
- Vilfan, M., Kokot, G., Vilfan, A., *et al.*, 2012. Analysis of fluid flow around a beating artificial cilium. *Beilstein Journal of Nanotechnology*, 3, 163–171.
- Vincensini, L., Blisnick, T. and Bastin, P., 2011. 1001 Model Organisms To Study Cilia and Flagella. *Biology of the cell / under the auspices of the European Cell Biology Organization*, 103(3), 109–30.
- Vogan, K., and Tabin, C., 1999. A new spin on handed asymmetry. *Nature*, 397, 295–298.
- Wang, G., Manning, M.L. and Amack, J.D., 2012. Regional cell shape changes control form and function of Kupffer's vesicle in the zebrafish embryo. *Developmental biology*, 370(1), 52–62.

- Wang, X. and Yost, H.J., 2008. Initiation and propagation of posterior to anterior (PA) waves in zebrafish left-right development. *Development Dynamics*, 237, 3640–3647
- Westerfield, M., 1995. *The Zebrafish Book*. Eugene: University of Oregon Press.
- Yamamoto, R., Song, K., Yanagisawa, H.A., *et al.*, 2013. The MIA complex is a conserved and novel dynein regulator essential for normal ciliary motility. *Journal of Cell Biology*, 201, 263–278.
- Zhang, X.M., Ramalho-Santos, M. and McMahon, A.P., 2001. Smoothed mutants reveal redundant roles for Shh and Ihh signaling including regulation of L/R symmetry by the mouse node. *Cell*, 106, 781–792.
- Zhang, Y.J., O’Neal, W.K., Randell, S.H., *et al.*, 2002. Identification of dynein heavy chain 7 as an inner arm component of human cilia that is synthesized but not assembled in a case of primary ciliary dyskinesia. *Journal of Biological Chemistry*, 277(20), 17906–17915.

Annex I

Scripts to R program

Fast Fourier Transform (FFT) function

```
PEAKS_LIM <- 13

peaks <- function(series, span=PEAKS_LIM - 2)
{
  z <- embed(series, span)
  s <- span%%2
  v <- max.col(z, "first") == 1 + s # take first if a tie
  result <- c(rep(FALSE, s), v)
  result <- result[1:(length(result)-s)]
  result
}

filterTimeSeries <- function(timeSeries, LowFreqRange, HighFreqRange, end, timeScale)
{
  limit = 4
  layout(matrix(c(1,2,3,4), 2, 2, byrow = TRUE))
  data.freqDomain <- fft(timeSeries)

  frequency <- c( 1:length(Mod(data.freqDomain)) )
  frequency <- frequency/length(data.freqDomain)
  frequency <- frequency/timeScale
  plot(frequency, Mod(data.freqDomain), type = "l", main = "Re Frequency domain", xlab = "Beat
frequency (Hz)", ylab = "Power", xlim = c(0, frequency[length(frequency)/2]))

  data.freqDomain[HighFreqRange] <- 0 + 0i
  HighFreqRange2 <- rev(HighFreqRange)
  HighFreqRange2 <- length(timeSeries) - HighFreqRange2[1:length(HighFreqRange2)] + 1
  data.freqDomain[HighFreqRange2] <- 0 + 0i

  data.freqDomain[LowFreqRange] <- 0 + 0i
  LowFreqRange2 <- rev(LowFreqRange)
  LowFreqRange2 <- length(timeSeries) - LowFreqRange2[1:length(LowFreqRange2)] + 1
  data.freqDomain[LowFreqRange2] <- 0 + 0i

  ts.f <- Mod(data.freqDomain[1:(length(frequency)/2)])
  pks <- peaks( ts.f, span=PEAKS_LIM)
  fq.max <- frequency[1:(length(frequency)/2)]
  fq.max <- fq.max[pks]; fq.max
  fq.max <- round(fq.max, 1)
}
```

```

y.peaks<-ts.f[pks]
y.max<-y.peaks[which(y.peaks>PEAKS_LIM-1)]
x.max<-fq.max[which(y.peaks>PEAKS_LIM-1)]
vals<-data.frame(Max.Freq = x.max, Power = round(y.max, 1))
vals<- vals[order(-vals[,2]),]
plot(frequency[1:length(frequency)/2], Mod(data.freqDomain[1:length(frequency)/2]), type = "b",
     main = "Re Frequency domain filtered", xlab = "Beat frequency (Hz)", ylab ="Power", xlim = c(1 +
limit,frequency[length(frequency)/2] - limit), ylim = c(0,50), pch = 1)
abline(v=x.max, col = "red")
if(length(x.max>0)) text(x.max+ 5, y.max +4, paste (x.max, "Hz"), col = "red")

data.timeDomain <- fft(data.freqDomain, inverse = TRUE)
data.timeDomain <- data.timeDomain/length(data.freqDomain)
data.timeDomain <- Mod(data.timeDomain)

time <- c(1:length(data.timeDomain))*timeScale
plot(time,timeSeries, type = "l",
     main = "Time domain", xlab = "time (s)", ylab ="intensity")
plot(time,data.timeDomain, type = "l",
     main = "Time domain filtered", xlab = "time (s)", ylab ="intensity")
beatFreq <- cbind(frequency ,Mod(data.freqDomain))
return (beatFreq)
}
plotSelectedFreqDomain<- function(timeSeries, XLIM)
{
layout(1)
data.freqDomain<-fft(timeSeries)
plot(Mod(data.freqDomain[XLIM]), type = "l",
     main = "Frequency domain filtered", xlab = "Frequency", ylab ="Power")
}
readData<-function(filename,timeScale, range)
{
data <- read.table(filename, skip =1)
colnames(data)<- c("t","f")
colnames(data)
data.selected <-data$f[range]
data.selected<-normalise(data.selected)
end<-round(length(data.selected)/2)
LowFreqRange<-1:3

```

```

HighFreqRange<-(end-4):end
ReFreqDomainFiltered<- filterTimeSeries(data.selected, LowFreqRange, HighFreqRange, end,
timeScale)
ReFreqDomainFiltered<-ReFreqDomainFiltered[range,]
return(ReFreqDomainFiltered)
}
normalise<-function(d)
{
  d<as.vector(d)
  d<-(d- min(d))/(max(d) - min(d) )
  return(d)
}
##### Read data #####
setwd("E:/Desktop") #Kymograph directory
filename <- "Plot_Values.xls" #Name of kymograph file
timescale <- 1/500 #Time in seconds / Number of frames
Range <- 1:1000 # This is the range that you used to create the kymograph
Wt1C1 <- readData (filename, timescale, Range)

```

Rayleigh test and flow maps functions

```

setOrigin <- function(xy, x0, y0, R, velFactor){
  x<- -(xy[,4] - x0) / R
  y<- (xy[,5] - y0) / R
  id<-xy[,2]
  omega <- atan2(x, y)
  r<- sqrt(x^2 + y^2)
  n<-length(x)
  a<-xy[,4][2:n] - xy[,4][1:(n-1)]
  b<-xy[,5][2:n] - xy[,5][1:(n-1)]
  alpha <-atan2(a, b)
  alpha.id <- which(alpha < 0)
  alpha[alpha.id] <- 2*pi + alpha[alpha.id]
  speed <- xy[,11]
  speed[is.na(speed)] <- 0
  p<- data.frame(x = x[1:(n-1)], y = y[1:(n-1)], id = id[1:(n-1)],
  omega = omega[1:(n-1)], r = r[1:(n-1)],
  alpha, speed = speed[2:(n)] * velFactor)

```

```

return(p)
}
KVvectorField<-function(Data, Name, Scale){
  drawKV(Name)
  mag<-Data$speed
  direction<-Data$alpha + pi/2
  xpos<-Data$x
  ypos<-Data$y
  vectorcol<-Data$id
  vectorField(direction,mag,xpos,ypos,scale=Scale,vecspec="rad",col="blue",headspan=0.03)
}
KVnormalizedVectorField <- function(Data, Name, Scale1, Scale2) {
  r.step = 0.15
  o.step = pi/36
  r.id = seq(0, 1.4 - r.step, r.step)
  o.id = seq(-pi, pi - o.step, o.step)
  data.av<-NULL
  for (i in 1:length(r.id)){
    for(j in 1:length(o.id)){
      data.sub<-subset(Data, r > r.id[i] & r < r.id[i] + r.step & omega > o.id[j] & omega < o.id[j] + o.step)
      speed.x<-(data.sub$speed)*cos(data.sub$alpha)
      speed.y<-(data.sub$speed)*sin(data.sub$alpha)
      vals<-data.frame(speed.x, speed.y, speed= data.sub$speed)
      if (length(data.sub[,1])>0){
        data.sub.m <- apply(data.sub,2, mean)
        vals.m <-apply(vals, 2, mean)
        speed.m<-sqrt(vals.m[1]^2 + vals.m[2]^2)
        data.sub.m[["speed"]] <- speed.m
        alpha <-atan2(vals.m[2], vals.m[1])
        if(alpha < 0) alpha <- 2*pi + alpha
        data.sub.m[["alpha"]] = alpha
        data.av<- rbind(data.av, as.vector(data.sub.m))
      }
    }
  }
  colnames(data.av)<-colnames(Data)
  data.av<-data.frame(data.av)
  par(mfrow = c(1,2))
  KVvectorField(Data, paste(Name, "(raw)"), Scale1)
  KVvectorField(data.av, paste(Name, "(smoothed)"), Scale2)
}

```

```

pdf(paste(Name, "_Flow.pdf", sep=""))
par(mfrow = c(1,2))
KVvectorField(Data, paste(Name, "(raw)"), Scale1)
KVvectorField(data.avs, paste(Name, "(smoothed)"), Scale2)
dev.off()
}
calcFlowHeatMaps<-function(data, Name){
  lim =2
  n<- 200
  L<- interp(data$x,data$y, data$speed,duplicate = "mean",
            xo=seq(-lim, lim, length=n), yo=seq(-lim, lim, length=n))
  L.smooth<- image.smooth( na.exclude(L), theta = 0.2)
  for (i in 1:length(L$z[,1]))
    for (j in 1:length(L$z[1,])){
      if(is.na(L$z[i,j])) L.smooth$z[i,j] =NA
    }
} par(mfrow = c(1,2))
drawKV(paste(Name, "Raw"))
image.plot(L, main = "S", xlim = c(-1,1), ylim = c(-1,1), zlim=c(0,30),add = T, horizontal =T, legend.lab
= expression (Flow~Velocity~(mu~m / s)))
redrawKV()
drawKV(paste(Name, "Smoothed"))
image.plot(L.smooth, "S blurred", xlim = c(-1,1), ylim = c(-1,1),zlim=c(0,30), add = T, horizontal =T,
legend.lab = expression (Flow~Velocity~(mu~m / s)))
redrawKV()
pdf(paste(Name, "_FlowHeatMaps.pdf", sep=""))
par(mfrow = c(1,2))
drawKV(paste(Name, "Raw"))
image.plot(L, main = "S", xlim = c(-1,1), ylim = c(-1,1),zlim=c(0,30), add = T, horizontal =T, legend.lab
= expression (Flow~Velocity~(mu~m / s)))
redrawKV()
drawKV(paste(Name, "Smoothed"))
image.plot(L.smooth, "S blurred", xlim = c(-1,1), ylim = c(-1,1), zlim=c(0,30),add = T, horizontal =T,
legend.lab = expression (Flow~Velocity~(mu~m / s)))
redrawKV()
dev.off()
}
drawKV <- function(nm){
  plot(c(-1.3, 1.3), c(-1.3,1.3), type = "n", asp=1,
      yaxt = 'n', xaxt='n', xlab = "", ylab = "",

```



```

    frame.plot = F, main = nm )
text(-1.3, 0, "L")
text(1.3, 0, "R")
text(0, 1.3, "A")
text(0, -1.3, "P")
}
redrawKV<- function(){
  text(-1.3, 0, "L")
  text(1.3, 0, "R")
  text(0, 1.3, "A")
  text(0, -1.3, "P")
  points(0,0, lwd =1)
}
circularAnalysis1<-function(Coords, minR){
  idx<-which(Coords$r > minR)
  print(length(idx))
  H <-circular(Coords$omega,type="angle",units="radians", rotation = "counter")
  plot(H[idx], rotation = "clock", zero =c(rad(90)), cex=1.03,
    stack=TRUE, add = T, axes = T, asp = 1, col = "darkgreen" )
  points(Coords$x[idx],Coords$y[idx], pch = 4,
    col = "darkgrey", cex = 0.5, symbol = "cross")
  draw.circle(0,0, minR, lty = 2, lwd =2)
  #Uniformity test
  rt<-rayleigh.test(H[idx], mu= NULL)
  p<-round(rt$p.value, digits = 3)
  for (i in seq(0, (3*pi)/2, by = pi/2)){
    rt<-rayleigh.test(H[idx], mu= circular(i))
    p<-c(p,round(rt$p.value, digits = 3))
  }
  l<-seq(0, (3*pi)/2, , by = pi/2)
  print(c(NA, l))
  print(p)
  text(0, 1.2, "A", cex = 1.2)
  text(0, 1.4, p[2], col = "darkgreen")
  mtext("R", 4, line = 0, las = 1)
  mtext(p[3], 4, line = 1, las = 1, col = "darkgreen", cex = 0.7)
  text(0, -1.2, "P", cex = 1.2)
  text(0, -1.4, p[4], col = "darkgreen")
  mtext("L", 2, line = 0, las = 1)
  mtext(p[5], 2, line = 1, las = 1, col = "darkgreen", cex = 0.7)

```

```

}
circularAnalysis2<-function(Coords, minR){
  idx<-which(Coords$r > minR)
  H <-circular(Coords$omega,type="angle",units="radians", rotation = "counter")
  rose.diag(-H[idx] + pi/2, bins=24,shrink=0.5,xlim=c(-2,2),ylim=c(-2,2),
    axes=FALSE,prop=2)
  p<-NULL
  for (i in seq(0, (3*pi)/2, by = pi/2)){
    rt<-rayleigh.test(H[idx], mu= circular(i))
    p<-c(p,round(rt$p.value, digits = 3))
  }
  text(0, 1.2, "A", cex = 1.2)
  mtext("R", 4, line = 0, las = 1)
  text(0, -1.2, "P", cex = 1.2)
  mtext("L", 2, line = 0, las = 1)
}
analyzeAndPlot<-function(dat, Name){
  pdf(paste(Name, ".pdf", sep=""))
  par(mfrow = c(1,3))
  drawKV(Name)
  points(dat$x,dat$y, pch = 19, col = dat$id, cex = 0.5)
  circularAnalysis1(dat, 0.5)
  circularAnalysis2(dat, 0.5)
  dev.off()
}
##### Read and analyze data #####
dir<-"G:/Desktop "
setwd(dir)
xy <- read.csv("Points1.txt", header = T, sep = "\t")
x0 <- 224
y0 <- 216
r <- 150
Name <- "Time course 1"
fps<- 1/0.2
pixelsToMicrons<-0.11825
velFactor = pixelsToMicrons * fps
WTcourse1.dat<-setOrigin(xy, x0, y0, r, velFactor)
analyzeAndPlot(WTcourse1.dat, Name)
KVnormalizedVectorField(WTcourse1.dat, Name, 1, 0.2)
calcFlowHeatMaps(WTcourse1.dat, Name)

```

Annex II

Supplemental data

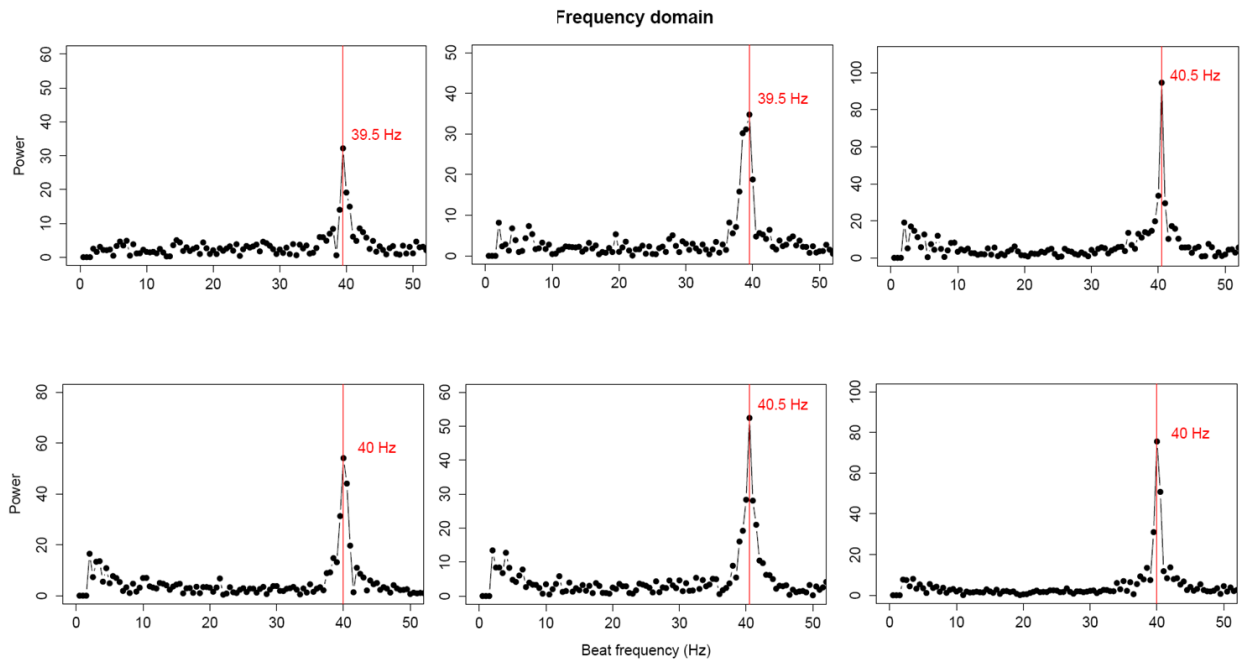


Figure S1 - CBF measurements of a cilium in a WT embryo revealed similar FFT spectra. Results from one cilium with single CBF after FFT spectral analyses, measured during one hour (10 minutes interval each) along 1000 frames. Measured frequencies are depicted as vertical red lines. CBF (cilia beat frequency); FFT (fast fourier transform).

16 hpf embryo

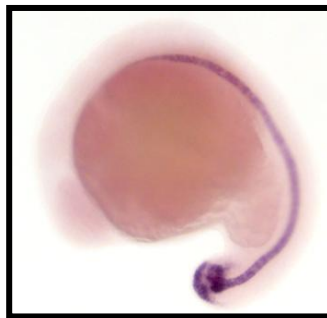


Figure S2 – WISH experiment for *ntl* gene in WT 16 hpf embryos, related with Figures 3.9 – 3.12 - Lateral view of WT embryo showing *ntl* expression at tail bud and along the notochord. *ntl* gene expression was used as an experimental positive control for WISH staining.

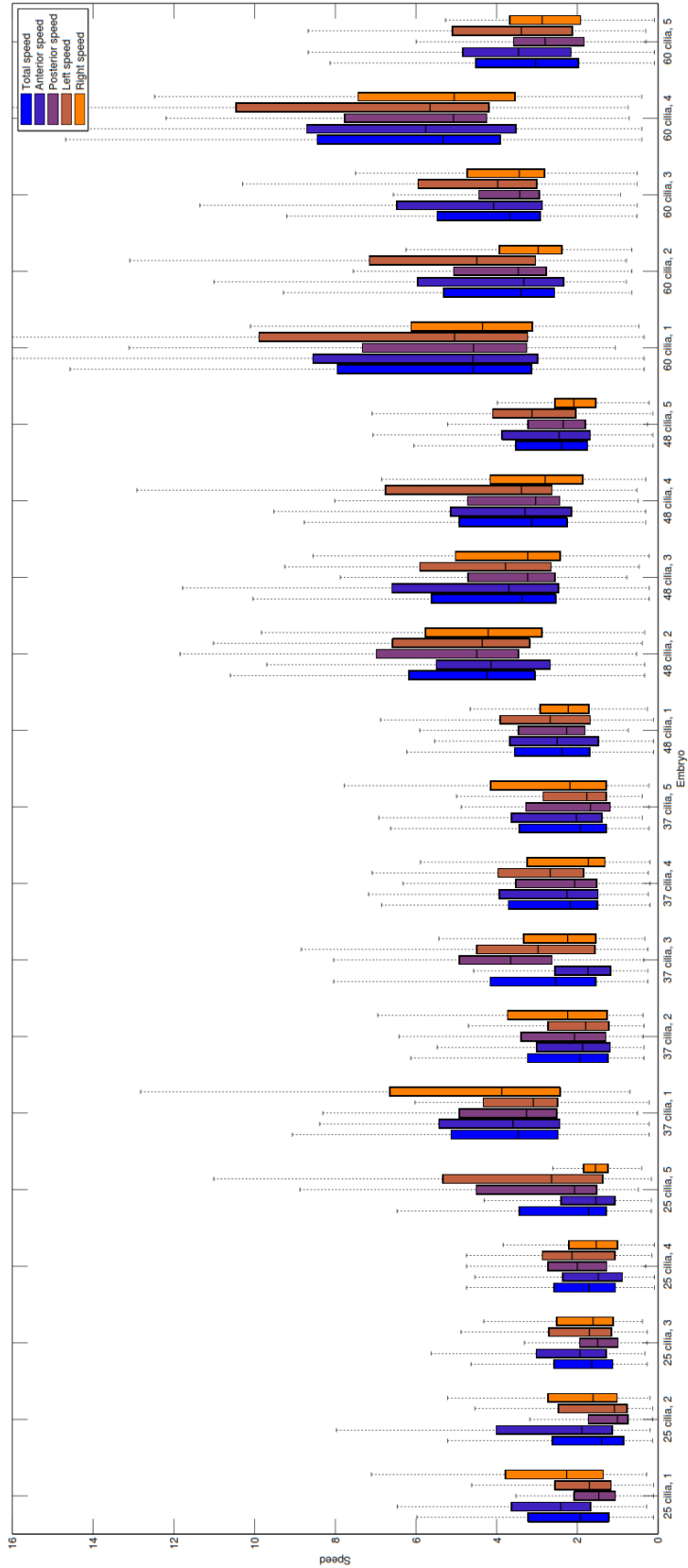


Figure S3. Simulation results for WT embryos, Related to Figure 3.23. For WT embryos, 5 simulations were performed for embryos with 25, 37, 45 and 60 cilia. These values were chosen to span the range of cilia numbers found in experimental data (Figures 3.1, 3.2, 3.3, 3.19, 3.20 and 3.21). Analysis of simulations focused on the Coronal plane time-averaged velocity field.

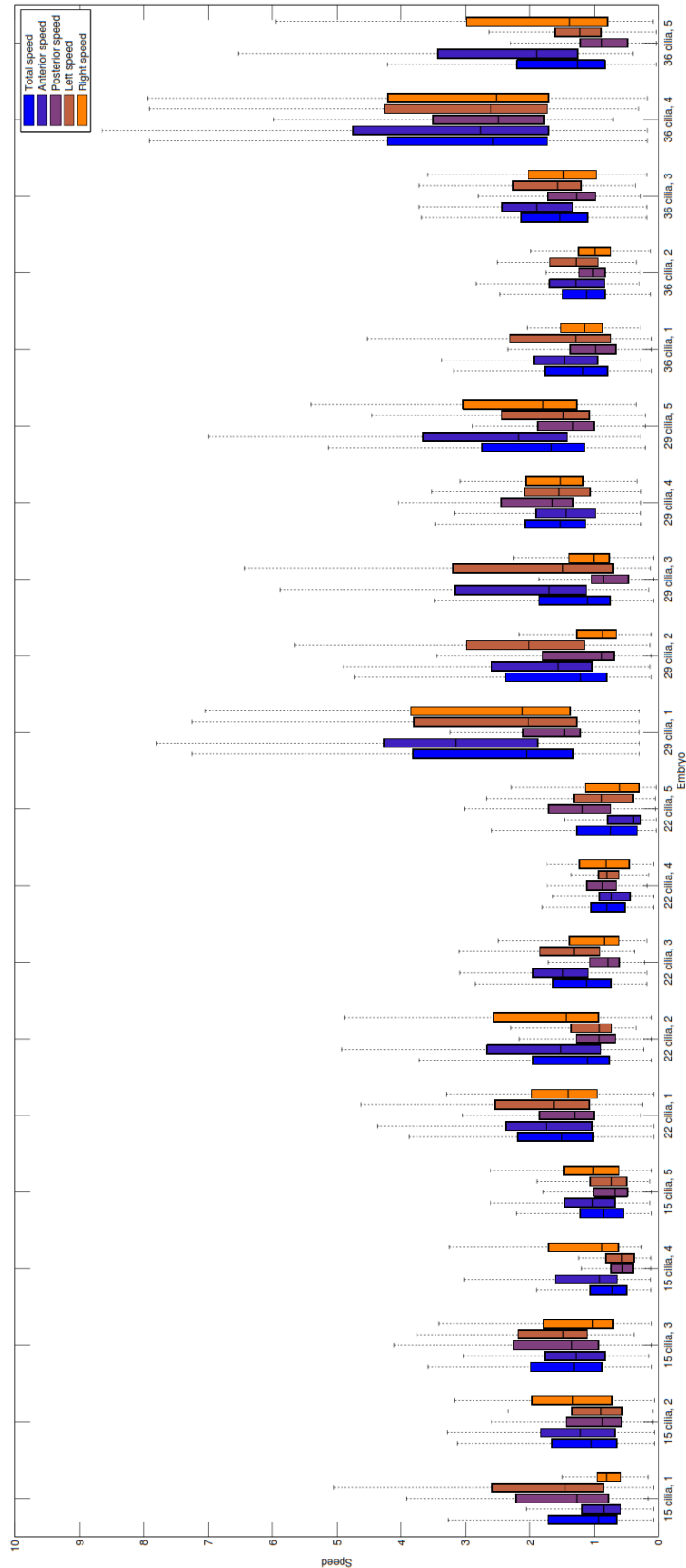


Figure S4. Simulation results for $\delta\text{tad}^{\Delta}$ mutant embryos, Related to Figure 3.23. For $\delta\text{tad}^{\Delta}$ mutant embryos, 5 independent simulations with different random parameters were performed for embryos with 15, 22, 29 and 36 cilia, according to experimental data (Figures 3.1, 3.2, 3.3, 3.19, 3.20 and 3.21). Analysis of simulations focused on the Coronal plane time-averaged velocity field.

Supplemental movies (available on CD)

Movie S1 – Motile cilium in wild-type Kupffer’s vesicle. Lateral view of a normal motile cilium inside the Kupffer’s vesicle from uninjected wild-type embryo at 8 somites stage. High speed videomicroscopy recorded at 500 fps and played at 30 fps.

Movie S2 – Immotile cilium in wild-type Kupffer’s vesicle. Lateral view of an uninjected wild-type embryo at 8 somites stage. High speed videomicroscopy recorded at 500 fps and played at 30 fps.

Movie S3 – Kupffer’s vesicle as both immotile and motile cilia, related to Figure 3.4. Dorsal to ventral view of *sox17:GFP* transgenic embryo injected with *ar13b-GFP* to label the cilia in the Kupffer’s vesicle. Both motile and immotile cilia are present inside the KV. Anterior to the top.

Movie S4 - *dnah7* morpholino renders immotile cilia and compromises fluid flow inside the Kupffer’s vesicle, related to Figure 3.15. Injected embryo showing several immotile cilia while some native particles exhibit Brownian motion. Sequence of bright field images of a KV oriented with anterior axis to the top and left axis to the left of the page. Recorded at 60 fps and played at 30 fps.

Movie S5 - *dnah7* mismatch control-morpholino does not influence cilia motility or fluid flow inside the Kupffer’s vesicle, related with Figure 3.17. Injected embryo showing several motile cilia while a native particle moves in the presence of counterclockwise fluid flow. Sequence of bright field images of a KV oriented with anterior axis to the top and left axis to the left of the page. Recorded at 60 fps and played at 30 fps.

Movie S6 – Cilia motility and fluid flow inside the Kupffer’s vesicle in a WT embryo, related with Figure 3.15. Embryo showing several motile cilia while a native particle moves in the presence of counterclockwise fluid flow. High speed videomicroscopy recorded at 60 fps and played at 30 fps. Anterior to the top.

***In silico* experimentation via mathematical modeling**

The methodology used to generate geometrically and temporally detailed models of KV, resolved at the level of individual cilia, are extended from an earlier study (Smith *et al.*, 2012), and are described in detail below. KV is characterized by very small length and velocity scales; the Reynolds number, the ratio of viscous to inertial forces is $\mathcal{O}(10^{-3})$, so that the Stokes flow equations provide an accurate description of the fluid dynamics. These equations are linear, meaning that solutions to complicated problems may be calculated by superposing the simple solutions of flow generated by force singularities. Considering the Stokes flow equations driven by a smoothed point force,

$$\nabla p = \mu \nabla^2 \mathbf{u} + F \psi_\epsilon(\mathbf{x} - \mathbf{y}), \nabla \cdot \mathbf{u} = 0, \quad (\text{S1})$$

where p is pressure, \mathbf{u} is velocity, and μ is the fluid dynamic viscosity, Cortez (2001) introduced the ‘regularized stokeslet’. The symbol $\psi_\epsilon(\mathbf{x} - \mathbf{y})$ denotes a cut-off function or ‘blob’ with regularization parameter $\epsilon > 0$.

By placing distributions of regularized stokeslets over the surface of our computational mesh of KV, weighted by the hydrodynamic force per unit area (stress), the flow can therefore be calculated. Simulating the flow in KV comprises three steps,

- Geometry: specify KV dimensions, cilia beat pattern, frequency and location and generate timelapse surface mesh.
- Stress calculation: calculate the viscous force per unit area on the surface mesh.
- Velocity calculation: using the viscous force, calculate the time-averaged flow in the vesicle midplane.

Step (1) calculates the surface location and velocities, step (2) formulates a set of linear algebraic equations which relate the unknown stress to the known surface velocities and solves them to determine the stress, step (3) then involves calculating velocity in the interior of the fluid from integrals of the fundamental solutions weighted by the stresses. The uncoupling of the stress calculation and calculation of velocity in the interior of the fluid is a consequence of the linearity of Stokes flow and associated boundary element representation of the flow. This uncoupling is computationally very convenient in that it greatly reduces the number of unknowns and also removes the need for meshing of the interior of KV. It also means that regions of KV in which velocity calculations are not required (for example when running particle tracking simulations or when calculating 2D slices) can be omitted completely from the simulation.

Encoding experimental observations into a computational mesh

We use a modification of the meshing method developed previously (Smith *et al.*, 2012). Beginning with a scalene ellipsoidal model of KV, cilia are given random placements in the dorsal-

anterior, dorsal-central, dorsal-posterior and ventral quadrants with density distribution given by 38%, 25%, 17% and 20% of cilia in the D-A, D-C, D-P, and V quadrants respectively (Kreiling *et al.*, 2007). The ellipsoidal surface is then triangulated with DistMesh, using these cilium locations as fixed vertices. From this triangulation, Voronoi cells are constructed, which form a model of the ciliated cell structure. Cilia are then smoothly inserted on each cell containing the assigned cilium vertices, and the mesh is calculated over a time-lapse describing the beating of each cilium. This model now allows for arbitrary cilium placement, length, frequency and motility, in contrast to earlier work (Smith *et al.*, 2012). These parameters are randomly assigned to each cilium from fitted distributions of experimental data (Figures 3.1, 3.2, 3.3, 3.19, 3.20). This statistical sampling approach is motivated by fact that the flow produced by an individual cilium scales with the cube of cilia length (Smith *et al.*, 2008). This nonlinear dependence shows that long cilia have a disproportionate influence, and hence a 'mean length' model is not justified.

The code produces a time-lapse of quadratically (Q9-T6) smooth surface meshes, which can be used for visualization purposes, and as input to the regularized stokeslet boundary element method for fluid dynamics calculations.

Cilium beat patterns and wobbling

Cilia were modelled as whirling rods, performing a conical rotational motion. This was achieved by specifying a cilium centerline of the form $\xi = b \tanh(as)$ for semi-cone angle $b = 35^\circ$, bend-curvature $a = 5 \mu\text{m}^{-1}$, and arclength s , then rotating this centerline about the tilted axis with the primary frequency f_1 . The secondary frequency f_2 of wobbling cilia was incorporated through oscillations in the cilium semicone angle,

$$\xi = (b + \beta \sin(2\pi(f_1 - f_2) t)) \tanh(as); \quad (\text{S2})$$

resulting in the beat kinematics shown in Figures 3.1, 3.2, 3.3. The amplitude of wobbling β was specified to replicate the power and frequency of the Fourier peaks observed experimentally.

Statistics of KV morphology

The numbers of immotile, wobbling and single beat frequency cilia in each simulation were taken as the rounded whole number closest to the experimentally observed averages of 22% immotile, 14.4% wobbling for WT and 15% immotile, 11.3% wobbling for deltaD^-

Cilia beat frequencies were randomly sampled from a normal distribution, truncated at 0, fitted to the experimental data. For deltaD^- , single beat frequency cilia were sampled from a distribution with mean $\mu = 33.9$ Hz and standard deviation $\sigma = 4.3$ Hz. The primary frequency of wobbling cilia were sampled with mean $\mu = 31.1$ Hz and standard deviation $\sigma = 6.3$ Hz, whereas the secondary

frequencies were sampled with mean $\mu = 10.8$ Hz and standard deviation $\sigma = 9.4$ Hz, truncated at $f_2 = 0$. For WT, single beat frequency cilia were sampled from a distribution with mean $\mu = 33.9$ Hz and standard deviation $\sigma = 4.1$ Hz. The primary frequency of wobbling cilia were sampled with mean $\mu = 28.7$ Hz and standard deviation $\sigma = 7.3$ Hz, whereas the secondary frequencies were sampled with mean $\mu = 9.0$ Hz and standard deviation $\sigma = 6.5$ Hz, truncated at $f_2 = 0$.

Cilia lengths were randomly sampled from a generalized distribution, which has probability density function

$$\gamma_{\text{pdf}}(y) = \left(\frac{y-m}{b}\right)^{a-1} \frac{\exp(-\frac{y-m}{b})}{b\Gamma(a)}, \quad y \geq m, \quad a > 0, \quad b > 0. \quad (\text{S3})$$

that provided the best fit for the experimental data. For $\text{delta}D^{\prime}$, $m = -0.55$, $a = 8.6$ and $b = 0.47$, while for WT $m = -18.3$, $a = 203.1$, $b = 0.11$. The disparity in parameters arises from the small value of b for WT, which indicates that the mean and modal lengths are approximately $0.11 \mu\text{m}$ apart for WT. These data were inputted to the meshing code to create the computational model.

Calculating stresses on KV

For the cut-off function $\psi_{\epsilon}(x - y) := 15\epsilon^4 = (8\pi\mu r_{\epsilon}^7)$, Cortez *et al.* (2005) showed that the regularized stokeslet is given by

$$S_{ij}^{\epsilon}(\mathbf{x}, \mathbf{y}) = \frac{\delta_{ij}(r^2 + 2\epsilon^2) + r_i r_j}{r_{\epsilon}^3} \quad \text{where} \quad r_{\epsilon}^2 = r^2 + \epsilon^2. \quad (\text{S4})$$

The resultant regularized stokeslet boundary integral equation is then,

$$u_j(\mathbf{y}) = \int_D [S_{ij}^{\epsilon}(\mathbf{x}, \mathbf{y}) f_i(\mathbf{x}) - u_i(\mathbf{x}) T_{ijk}^{\epsilon}(\mathbf{x}, \mathbf{y}) n_k(\mathbf{x})] dS_x + \mathcal{O}(\epsilon^2), \quad (\text{S5})$$

for flow bounded by a surface D . The symbol $u_j(\mathbf{y})$ denotes the fluid velocity at a general point \mathbf{y} and $n_k(\mathbf{x})$ is a unit surface normal pointing into the fluid. The density $f_i(\mathbf{x})$ has dimensions of stress, and therefore $f_i(\mathbf{x})dS_x$ has dimensions of force. The tensor $T_{ijk}^{\epsilon}(\mathbf{x}, \mathbf{y})$ is the stress field corresponding to the regularized stokeslet. The ‘double-layer potential’ associated with $T_{ijk}^{\epsilon}(\mathbf{x}, \mathbf{y})$ is neglected, since the motion of cilia is treated as rigid. Since the single-layer potential associated with $S_{ij}^{\epsilon}(\mathbf{x}, \mathbf{y})$ is continuous as \mathbf{y} approaches D ,

$$u_j(\mathbf{y}) = \int_D S_{ij}^{\epsilon}(\mathbf{x}, \mathbf{y}) f_i(\mathbf{x}) dS_x + \mathcal{O}(\epsilon^2), \quad \text{for} \quad \mathbf{y} \in D. \quad (\text{S6})$$

Since the velocity on the surface is prescribed, this information is used to calculate the unknown stress $f_i(\mathbf{y})$ for $\mathbf{y} \in D$. These stresses may then be used to calculate the flow velocity at any point within the fluid. The stress is discretized as piecewise constant $f_i[1], \dots, f_i[N]$ on surface elements $D[1], \dots, D[N]$, where $D = D[1] \cup \dots \cup D[N]$ is the surface mesh and N is the number of mesh elements. The equation may then be written,

$$u_j(\mathbf{y}) = \sum_{n=1}^N f_i[n] \int_{D[n]} S_{ij}^e(\mathbf{x}, \mathbf{y}) dS_x \quad \text{where } \mathbf{y} \in D[m]. \quad (\text{S7})$$

Setting \mathbf{y} to be the centroid of each element $D[m]$, with $m = 1, \dots, N$ and $j = 1, 2, 3$, yields $3N$ equations for $3N$ unknown scalar stresses. For the present study, we solved systems with up to 8,344 surface elements, corresponding to 25,032 degrees of freedom with the NAG Fortran library Restarted GMRES algorithm (Numerical Algorithms Group, Oxford, UK).

Extracting and analyzing the fluid flow

Given the known stresses on each element, the flow velocity at any point in the domain is calculated from equation (S7). To calculate the time-averaged velocity over the Coronal midplane, the average beat frequency was subdivided into three intervals, and the velocity calculated at twelve steps corresponding to nodes of Gauss-Legendre quadrature. This was done for five complete cycles of the average beat frequency, resulting in a total of 180 time-steps over which the velocity was integrated, and then divided to produce the time-averaged flow. The resultant flow for the second δD^2 simulation with 36 cilia for the sample is shown within the mesh in figure 3.22.

Supplemental references

- Cortez, R., Fauci, L., and Medovikov, A., 2005. The method of regularized Stokeslets in three dimensions: analysis, validation, and application to helical swimming. *Physics of Fluids*, 17, 1–14.
- Cortez, R., 2001. The method of regularized Stokeslets. *SIAM Journal on Scientific Computing*, 23(4), 1204–1225.
- Kreiling, J.A., Prabhat, Williams, G., and Creton, R., 2007. Analysis of Kupffer’s vesicle in zebrafish embryos using a cave automated virtual environment. *Developmental Dynamics*, 236(7), 1963–1969.
- Smith, D.J., Blake, J.R. and Gaffney, E.A., 2008. Fluid mechanics of nodal flow due to embryonic primary cilia. *Journal of the Royal Society Interface*, 5(22), 567–573.
- Smith, A.A., Johnson, T.D., Smith, D.J., and Blake, J.R., 2012. Symmetry breaking cilia-driven flow in the zebrafish embryo. *Journal of Fluid Mechanics*, 705, pp.26–45.